

27721



National Library of Canada

Bibliothèque nationale du Canada

CANADIAN THESES ON MICROFICHE

THÈSES CANADIENNES SUR MICROFICHE

NAME OF AUTHOR/NOM DE L'AUTEUR ANTHONY WILLIAM PASTERNAK

TITLE OF THESIS/TITRE DE LA THÈSE COOPERATIVE THOMSON SCATTERING FROM AN ARGON ARC PLASMA USING A PULSED CO₂ LASER

UNIVERSITY/UNIVERSITÉ ALBERTA

DEGREE FOR WHICH THESIS WAS PRESENTED/ GRADE POUR LEQUEL CETTE THÈSE FUT PRÉSENTÉE PH.D.

YEAR THIS DEGREE CONFERRED/ANNÉE D'OBTENTION DE CE GRADE 1976 SPRING CONV.

NAME OF SUPERVISOR/NOM DU DIRECTEUR DE THÈSE DR. A.A. OFFENBERGER
+ DR. P.R. SMY

Permission is hereby granted to the NATIONAL LIBRARY OF CANADA to microfilm this thesis and to lend or sell copies of the film.

L'autorisation est, par la présente, accordée à la BIBLIOTHÈQUE NATIONALE DU CANADA de microfilmer cette thèse et de prêter ou de vendre des exemplaires du film.

The author reserves other publication rights, and neither the thesis nor extensive extracts from it may be printed or otherwise reproduced without the author's written permission.

L'auteur se réserve les autres droits de publication; ni la thèse ni de longs extraits de celle-ci ne doivent être imprimés ou autrement reproduits sans l'autorisation écrite de l'auteur.

DATED/DATE Jan 23/76 SIGNED/SIGNÉ Anthony Pasternak

PERMANENT ADDRESS/RÉSIDENCE FIXE 11435-79th Avenue
EDMONTON, ALBERTA
T6G 0P8

INFORMATION TO USERS

THIS DISSERTATION HAS BEEN
MICROFILMED EXACTLY AS RECEIVED

This copy was produced from a microfiche copy of the original document. The quality of the copy is heavily dependent upon the quality of the original thesis submitted for microfilming. Every effort has been made to ensure the highest quality of reproduction possible.

PLEASE NOTE: Some pages may have indistinct print. Filmed as received.

Canadian Theses Division
Cataloguing Branch
National Library of Canada
Ottawa, Canada K1A 0N4

AVIS AUX USAGERS

LA THESE A ETE MICROFILMEE
TELLE QUE NOUS L'AVONS RECUE

Cette copie a été faite à partir d'une microfiche du document original. La qualité de la copie dépend grandement de la qualité de la thèse soumise pour le microfilmage. Nous avons tout fait pour assurer une qualité supérieure de reproduction.

NOTA BENE: La qualité d'impression de certaines pages peut laisser à désirer. Microfilmée telle que nous l'avons reçue.

Division des thèses canadiennes
Direction du catalogage
Bibliothèque nationale du Canada
Ottawa, Canada K1A 0N4

THE UNIVERSITY OF ALBERTA

COOPERATIVE THOMSON SCATTERING FROM AN ARGON
ARC PLASMA USING A PULSED CO₂ LASER

by



ANTHONY WILLIAM PASTERNAK

A THESIS

SUBMITTED TO THE FACULTY OF GRADUATE STUDIES AND RESEARCH
IN PARTIAL FULFILLMENT OF THE REQUIREMENTS FOR THE DEGREE
OF DOCTOR OF PHILOSOPHY

DEPARTMENT OF ELECTRICAL ENGINEERING

EDMONTON, ALBERTA

SPRING, 1976

THE UNIVERSITY OF ALBERTA
FACULTY OF GRADUATE STUDIES AND RESEARCH

The undersigned certify that they have read, and recommend to the Faculty of Graduate Studies and Research, for acceptance, a thesis entitled COOPERATIVE THOMSON SCATTERING FROM AN ARGON ARC PLASMA USING A PULSED CO₂ LASER, submitted by ANTHONY WILLIAM PASTERNAK in partial fulfilment of the requirements for the degree of Doctor of Philosophy.

A. Offenberg

.....
Supervisor

Peter R. Jones

.....
Supervisor

C. P. Cuyack

.....
A. M. Labussein

.....
John Keys

.....
External Examiner

Douglas M. Sheppard

Date *Nov 18, 1975*

ABSTRACT

Experiments involving cooperative Thomson scattering from a magnetized argon arc plasma are reported. For the first time, thermal ion fluctuations have been observed using a pulsed CO₂ laser as incident source. Resolution of scattered ion spectra was achieved with an infrared Fabry-Perot interferometer.

Design features are described and operational parameters given for the arc plasma facility and a high power CO₂ pulsed laser system. Electrostatic probe diagnostics are discussed as applied to the argon arc and subsequent electron temperature and density information is presented. Line broadening measurements are described along with an investigation of the Zeeman splitting of spectral lines. Ion temperature and magnetic field data are respectively derived from these spectroscopic methods.

A theoretical evaluation of the extent of arc plasma perturbations due to interactions with high power CO₂ laser radiation is reported along with associated experimental observations.

Finally, aspects of the Thomson scattering experimental design are detailed and experimental results compared with the theory. Application of this technique to low density, high temperature plasmas such as present toroidal devices is discussed.

ACKNOWLEDGMENTS

Special thanks are due to Dr. A.A. Offenberger who, as supervisor of this work, has given generously of his time and energy in providing a very stimulating atmosphere for experimental research. His enthusiasm for science has been a continually uplifting influence. I am grateful as well for his prompt reading and returning of drafts of this thesis while on sabbatical leave.

I wish also to express my thanks to Dr. P.R. Smy for helpful discussions concerning plasma probes, his reading of the thesis draft on that subject, and for kindly serving as advisor during Dr. Offenberger's absence.

In appreciation of excellent technical support which has been received, I would like to thank the following people: Doug Way-Nee and Brian Hadley for their skilled assistance with laboratory equipment and for their cheerful forbearance; EE machine shop personnel, especially Konrad Doerrbäcker, Herb Gans and Steve Gomez, for fine machining work and helpful cooperation in construction of experimental apparatus; and Barry Arnold for providing high quality optical components.

I am indebted to Margaret Hinchliffe for her effort and patience in quickly preparing this manuscript and to Mrs. R. Robinson for typing of rough drafts.

Financial assistance from the National Research Council and from Dr. Offenberger is gratefully acknowledged.

TABLE OF CONTENTS

| | | Page |
|-------------|---|------|
| CHAPTER I | INTRODUCTION | 1 |
| CHAPTER II | SCATTERING THEORY; MOTIVATIONS FOR CO ₂ LASER SCATTERING DEVELOPMENT | 3 |
| | 2.1 Outline | 3 |
| | 2.2 Diagnostic Overview of Scattering | 3 |
| | 2.3 Thomson Scattering Theory | 4 |
| | 2.3.1 Scattering by a Single Electron | 4 |
| | 2.3.2 Scattering from Plasma Electrons | 7 |
| | 2.3.3 Magnetic Field Effects on Scattered Spectra | 11 |
| | 2.3.4 Collisional Effects on Scattered Spectra | 13 |
| | 2.4 Scattering with CO ₂ Lasers | 13 |
| | 2.5 CO ₂ Scattering from a Hollow Cathode Arc Plasma | 16 |
| CHAPTER III | PLASMA FACILITY AND CO ₂ LASER SYSTEMS | 17 |
| | 3.1 Outline | 17 |
| | 3.2 Argon Arc Plasma Facility | 17 |
| | 3.2.1 General Requirements | 17 |
| | 3.2.2 Initial Development | 18 |
| | 3.2.3 Arc Chamber and Electrode Design | 19 |
| | 3.2.4 Electrical Characteristics | 22 |
| | 3.2.5 Arc Striking | 25 |
| | 3.3 CO ₂ Pulsed Lasers for Scattering | 26 |
| | 3.3.1 Oscillator-Amplifier System | 26 |

| | Page |
|---|------|
| 3.3.2 Two Discharge 6.7 Meter Oscillator | 30 |
| 3.3.3 Laser Line Spectra | 31 |
| 3.4 Conclusions | 33 |
| CHAPTER IV : PROBE AND SPECTROSCOPIC DIAGNOSTICS | 34 |
| 4.1 Outline | 34 |
| 4.2 Probe Measurements | 35 |
| 4.2.1 Introduction | 35 |
| 4.2.2 Probe Theory | 35 |
| 4.2.3 Experimental Method | 38 |
| 4.2.4 Experimental Results | 39 |
| 4.2.5 Discussion | 45 |
| 4.3 Optics for Spectroscopic Measurements | 50 |
| 4.4 Line Broadening and Splitting | 52 |
| 4.4.1 Fabry-Perot Resolution | 54 |
| 4.4.2 Experimental Results | 56 |
| 4.4.3 Discussion | 60 |
| 4.5 Hydrogen Impurity in the Arc | 61 |
| 4.6 Conclusions | 63 |
| CHAPTER V : ARC PLASMA PERTURBATION BY A HIGH POWER CO ₂ LASER | 65 |
| 5.1 Outline | 65 |
| 5.2 Thermal Conduction Limited Electron Heating | 65 |
| 5.3 Experimental Observations and Discussion | 72 |
| CHAPTER VI : COOPERATIVE THOMSON SCATTERING EXPERIMENTS | 75 |

| | Page |
|--|------|
| 6.1 Outline | 75 |
| 6.2 Scattered Spectral Shapes | 76 |
| 6.3 Experimental Design | 80 |
| 6.3.1 Input Optics | 80 |
| 6.3.2 Collection Optics | 81 |
| 6.3.3 Stray Laser Light | 84 |
| 6.3.4 Fabry-Perot Interferometer Resolution | 84 |
| 6.3.5 Fabry-Perot Thermal Stabilization | 87 |
| 6.3.6 Infrared Detector | 88 |
| 6.4 Signal/Noise Calculations | 89 |
| 6.5 Experimental Noise Levels | 91 |
| 6.6 Experimental Signal Levels | 92 |
| 6.7 Experimental Fabry-Perot Instrument Functions | 96 |
| 6.8 Enhancement of Signal/Noise | 98 |
| 6.9 CO ₂ Laser Scattering Results and Discussion | 102 |
| 6.10 Cooperative CO ₂ Scattering from a Tokamak Plasma | 108 |
| CHAPTER VII : SUMMARY AND CONCLUSIONS | 114 |
| REFERENCES | 117 |

LIST OF FIGURES

| | | |
|------------|--|----|
| FIGURE 2.1 | Scattering of an electromagnetic wave by an electron. | 5 |
| FIGURE 3.1 | Magnetic field profiles for the argon arc. | 20 |
| 3.2 | Arc chamber assembly and striking circuitry. | 21 |
| 3.3 | Photograph of the argon arc. | 23 |
| 3.4 | Arc volt-amp characteristics. | 24 |
| 3.5 | CO ₂ laser pulse shapes. | 28 |
| 3.6 | CO ₂ laser multi-shot wavelength spectra. | 32 |
| FIGURE 4.1 | Probe setup inside the arc chamber. | 36 |
| 4.2 | Design of plane probes. | 37 |
| 4.3 | Spatial current profiles for double-ended plane probes. | 40 |
| 4.4 | Volt-amp characteristics for swinging probes. | 41 |
| 4.5 | Profiles of electron temperature and density across the arc. | 42 |
| 4.6 | Voltage-swept probe curves. | 43 |
| 4.7 | Logarithmic plot of probe current versus voltage. | 47 |
| 4.8 | Optical systems for transverse and axial spectroscopic measurements. | 51 |
| 4.9 | Fabry-Perot instrument profiles for HeNe and HeCd laser lines. | 55 |
| 4.10 | π components of Doppler-broadened Ar II spectral lines. | 57 |
| 4.11 | σ components of Doppler-broadened Ar II spectral lines. | 58 |

| | | Page |
|--------|------|--|
| | 4.12 | Zeeman splitting of Ar I and Ar II transitions. 59 |
| | 4.13 | Broadening of the H α line. 62 |
| FIGURE | 5.1 | Model for plasma electron heating in the CO $_2$ laser focus. 69 |
| | 5.2 | Electron temperature perturbations as a function of laser intensity. 71 |
| FIGURE | 6.1 | Theoretical ion spectra for $\theta = 150^\circ$ backscatter. 78 |
| | 6.2 | Theoretical ion spectra for $\theta = 30^\circ$ forward scatter. 79 |
| | 6.3 | Input and detection optics for Thomson scattering. 82 |
| | 6.4 | Point source Fabry-Perot instrument profile. 86 |
| | 6.5 | Equivalent lens system for the detection optics. 93 |
| | 6.6 | Fabry-Perot instrument profiles for the scattering volume. 97 |
| | 6.7 | Detection and synchronization electronics for scattering. 100 |
| | 6.8 | Synchronization of boxcar integrator gate to resolved scattered signal. 101 |
| | 6.9 | Experimental data for $\theta = 150^\circ$ backscatter. 103 |
| | 6.10 | Experimental data for $\theta = 30^\circ$ forward scatter. 104 |
| | 6.11 | Comparison of experimental data to calculated spectrum for $\theta = 150^\circ$ backscattering. 105 |
| | 6.12 | Comparison of experimental data to calculated spectrum for $\theta = 30^\circ$ forward scattering. 106 |
| | 6.13 | Optics for small angle CO $_2$ laser scattering from a Tokamak plasma. 110 |

LIST OF TABLES

| | Page |
|---|------|
| TABLE 3.1 | |
| PARAMETERS OF CO ₂ PULSED LASERS USED FOR SCATTERING STUDIES. | 27 |
| TABLE 4.1 | |
| ION SATURATION CURRENTS. | 44 |

CHAPTER I

INTRODUCTION

Thomson scattering of electromagnetic radiation is an elegant plasma diagnostic, one which can provide comprehensive information from a minimum number of measurements. Scattering with ruby lasers has been well established as an on-line measurement technique for a number of years. However, for many plasma applications including important fusion research projects (toroidal devices), the full potential of the scattering diagnostic has not yet been realized. With the availability of high power CO₂ lasers, there is a reasonable possibility that this circumstance can eventually be altered.

These gas lasers have wavelengths in the neighborhood of 10 μm , and as scattering sources are thus suitable for observation of interesting and informative cooperative phenomena in plasmas from which only incoherent scattering results with a ruby probe. Although difficult technical problems exist with regard to experimental design and detection in the infrared, the CO₂ scattering technique is worthy of developmental effort because of the diagnostic benefits to be gained. A more complete outline of the factors motivating efforts towards CO₂ pulsed laser scattering is included in Chapter II, following a review of relevant scattering theory.

It was originally intended to study Thomson scattering from a hollow cathode arc discharge using a 1 MW CO₂ pulsed laser as incident source. However, investigations with this setup were hindered by very poor signal to noise in detection of spectrally integrated scattering.

This provided impetus for development of a higher density plasma and a more powerful pulsed laser. Construction of a 10-20 MW laser oscillator-amplifier system followed along with installation of a new plasma facility in the form of a magnetized d.c. argon arc operating in the multi-Torr pressure region. Chapter III contains descriptions of the plasma device and lasers.

As the plasma parameters of the arc were not well known, a series of probe and spectroscopic diagnostics were undertaken to determine densities, temperatures and magnetic fields. This experimental study is the subject of Chapter IV.

In Chapter V, the question of plasma disturbance by CO_2 pulsed lasers is discussed and Chapter VI contains the details of our cooperative scattering scheme and important results therefrom.

CHAPTER II

SCATTERING THEORY; MOTIVATIONS FOR CO₂ LASER SCATTERING DEVELOPMENT

2.1 Outline

A summary of some important results of Thomson scattering theory is given. Emphasis is placed on features of cooperative scattering which results when the incident wavelength is sufficiently long to probe plasma particle correlations. Possible magnetic field and particle collision effects on this scattered spectrum are summarized.

Advantages of the carbon dioxide laser as a source for cooperative scattering are discussed from the point of view of plasma information obtainable and potential applications, as well as some factors involved in detection and resolution of spectra.

The overall potential of such a diagnostic provides motivation for the development of a cooperative scattering technique employing a high power pulsed CO₂ laser and a plasma with electron density in the 10¹⁴-10¹⁵ cm⁻³ range. An initial attempt to carry out such a scattering experiment is briefly described.

2.2 Diagnostic Overview of Scattering

For several years, Thomson scattering has been established as a useful plasma diagnostic. Potentially, the technique is very powerful as, under suitable experimental conditions, information relating to electron and ion temperatures, electron density, ion charge

and density, magnetic fields and particle collisions may be obtained. In addition, the nature of plasma wave modes, wave damping and plasma turbulence effects may be studied.

Employment of lasers as radiation sources for scattering results in excellent spatial and temporal resolution - nominally given by the laser focal spot size and the laser ON time. Additionally, there is the important advantage of negligible disturbance of the plasma.

Drawbacks associated with scattering basically stem from the extremely small cross-section for the scattering process. Sophisticated, sensitive detection schemes are usually necessary to provide discrimination against competing plasma radiation and stray laser light along with various troublesome noise sources.

2.3 Thomson Scattering Theory

2.3.1 Scattering by a Single Electron

Thomson scattering involves the interaction of charged particles with electromagnetic waves. Charged particles are accelerated by incident electric fields and radiate as a result. The spectrum of radiation from an ensemble of scatterers reflects the average motion of the group.

In Fig. 2.1, the geometry for scattering by a single electron moving with velocity v is shown. The scattered E field amplitude is proportional to the acceleration caused by the incident field. In a plasma of ions and electrons, the lighter electrons are responsible

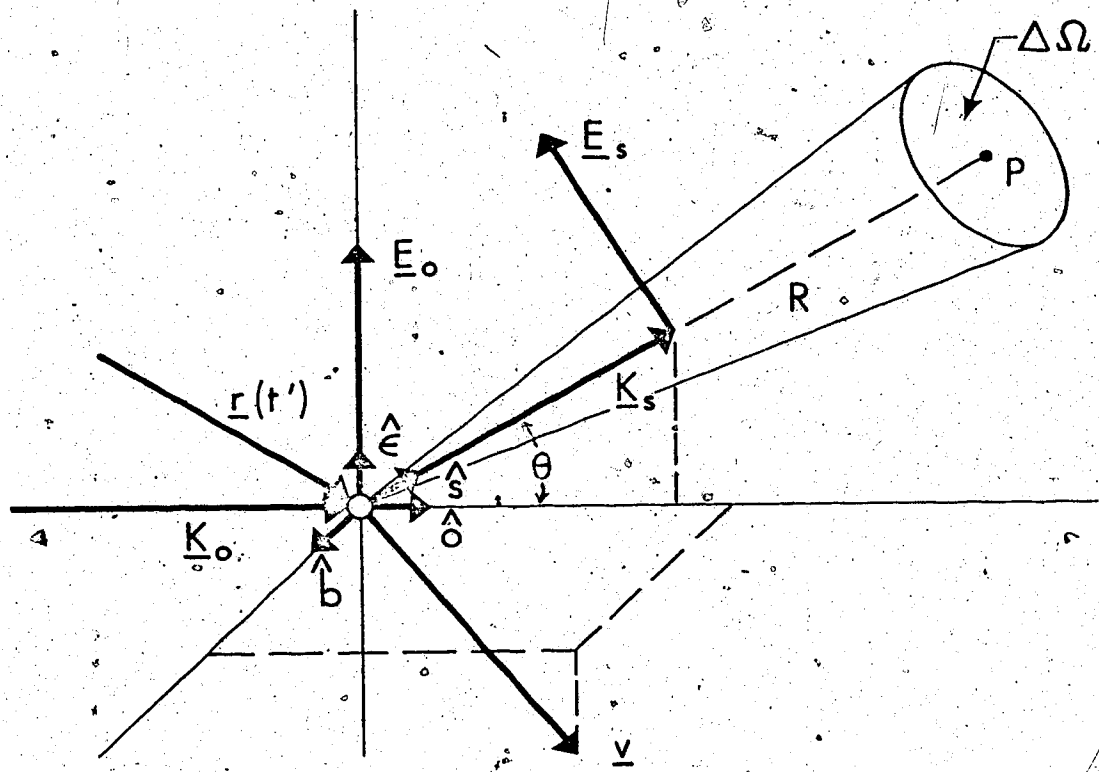


Fig. 2.1 Scattering of an electromagnetic wave by a single electron.

for essentially all the scattering. Information concerning ion motion is included by virtue of Coulomb interactions which influence the electrons.

Referring to Fig. 2.1, the incident \underline{E} field is denoted by

$$\underline{E}_0 = \hat{\epsilon} E_0 \cos (\underline{K}_0 \cdot \underline{r} - \omega_0 t') \tag{2.1}$$

An observer at position P, a distance R from the electron (in the far field) will, at time t, see a scattered \underline{E} field given by

$$\underline{E}_s = \frac{e^2 E_0}{m_e c^2 R} [\hat{s} \times (\hat{s} \times \hat{\epsilon})] \cos [K_s R - \omega_s t - \underline{K} \cdot \underline{r}(0)] \tag{2.2}$$

due to the acceleration of the charge at time

$$t' = \frac{t - R/c - \hat{s} \cdot \underline{r}(0)/c}{1 - \hat{s} \cdot \underline{v}/c} \tag{2.3}$$

In eqn. 2.2,

$$\underline{K}_s = \frac{\hat{s} K_0 (1 - \hat{o} \cdot \underline{v}/c)}{1 - \hat{s} \cdot \underline{v}/c} \tag{2.4}$$

$$\omega_s = c K_s \tag{2.5}$$

$$\underline{K} = \underline{K}_s - \underline{K}_0 \tag{2.6}$$

and

$$\omega = \omega_s - \omega_0 \tag{2.7}$$

The scattered frequency is seen to depend on the velocity of the scatterer in the form of two Doppler shifts, one between the frame of the incident field and that of the charge, the other between the frame of the charge and that of the observer.

Field 2.2 is calculated assuming $|\bar{v}/c| \ll 1$, which is satisfied in the low temperature plasmas used in these investigations. The amplitude of \underline{K} is then approximately

$$K = 2 K_0 \sin \theta/2 \quad (2.8)$$

In a solid angle $\Delta \Omega$, the observer will detect a time averaged scattered power, for unpolarized incident radiation, of

$$P_s = c r_e^2 E_0^2 \overline{\sin^2 \delta} \frac{\Delta \Omega}{4 \pi} \text{ watts} \quad (2.9)$$

where $r_e = e^2/m_e c^2 = 2.8 \times 10^{-13}$ cm is the classical electron radius and δ is the angle between $\hat{\epsilon}$ and \hat{s} . It is evident that the scattered power is an extremely small fraction of the incident power.

2.3.2 Scattering from Plasma Electrons

For an ensemble of N electrons in a plasma volume V , the total scattered \underline{E} field is a vector sum of the individual scattered fields. The scattered power is proportional to

$$\sum_{\ell=1}^N \sum_{j=1}^N \underline{E}_{sj} \cdot \underline{E}_{s\ell} = \sum_{j=1}^N E_{sj}^2 + \sum_{j \neq \ell} \underline{E}_{sj} \cdot \underline{E}_{s\ell} \quad (2.10)$$

The cross terms in eqn. 2.10 would sum to zero if the motions of electrons in the ensemble were completely uncorrelated with respect to the incident e.m. wave probe. When the source wavelength λ_0 is $\ll \lambda_D$, the electron Debye length, this is indeed the case, and the distribution of scattered frequencies is equivalent to the electron velocity distribution. The Debye length is given by

$$\lambda_D = \left(\frac{k T_e}{4\pi n_e e^2} \right)^{1/2} \text{ cm} \quad (2.11)$$

where k is Boltzmann's constant, T_e the electron temperature and n_e the electron density.

On the other hand, when $\lambda_0 \gg \lambda_D$, the incident wave sees the correlated motions of electrons, which exist due to Coulomb interactions with ions and other electrons and occur over a scale length of λ_D . The second sum on the right hand side of eqn. 2.10 now provides a considerable contribution to P_s . A scattered spectrum under these circumstances contains frequencies representative of ion thermal motion or ion acoustic waves and electron plasma waves.

A parameter

$$\alpha = \frac{1}{k\lambda_D} = \frac{\lambda_0}{4\pi \lambda_D \sin \theta/2} \quad (2.12)$$

is used to determine which type of spectrum will be observed. When $\alpha < 1$, the incoherent electron spectrum results. Coherent effects make an appearance as α approaches unity and become dominant for $\alpha \gg 1$.

The focus of investigations described herein has been on such cooperative scattering effects; to design an $\alpha > 1$ scattering experiment for a relatively low density plasma by utilizing a sufficiently long wavelength source. Specific details of this experiment will be described later; for now, a brief outline of the features of cooperative spectra is given.

In general, scattering of an incident e.m. wave can be considered to originate from microscopic fluctuations in electron density. At a given observation angle θ , the scattering is due to the particular component of density fluctuations $n_e(\underline{K}, \omega)$ for which \underline{K} and ω satisfy eqns. 2.6 and 2.7. Scattered power is related to an ensemble average of $n_e(\underline{K}, \omega)$ and this in turn to the two particle correlation

function^{2,3,4}. For a plasma of electrons and ions of charge Ze , this is given by

$$\langle |Q(\underline{K}, \omega)|^2 \rangle = \frac{|1-G_i|^2 f_e(-\frac{\omega}{K}) + Z |G_e|^2 f_i(-\frac{\omega}{K})}{K |1-G_e-G_i|^2} \quad (2.13)$$

In thermal equilibrium, $f_{e,i}$ are the Maxwellian velocity distributions of electrons and ions at T_e and T_i . G_e and G_i are functions of ω , K , T_e , T_i and α .

Salpeter² has evaluated eqn. 2.13 as a function of the scattering parameter α , and has provided normalized plots of scattered power versus frequency. In a functional form, the normalized spectra can be expressed as

$$P_N(\omega) = \bar{Q} \langle |Q(\omega)|^2 \rangle = \frac{\Gamma_\alpha \left(\frac{\omega}{\omega_e}\right)}{\omega_e} + \left(\frac{\alpha^2}{1 + \alpha^2}\right)^2 Z \Gamma_\beta \left(\frac{\omega}{\omega_i}\right) \quad (2.14)$$

where $\omega_{e,i} = k \bar{v}_{e,i}$. \bar{Q} is a normalization constant. The Γ functions give the basic shape of scattered spectra for varying α and β parameters, where

$$\beta = \left(\frac{Z \cdot T_e \alpha^2}{T_i (1 + \alpha^2)}\right)^{1/2} \quad (2.15)$$

Eqn. 2.14 provides an accurate description of incoherent spectra, while for cooperative spectra it is good for $\beta \lesssim \sqrt{3}$. For the scattering experiment eventually carried out, β was ≈ 1.2 , sufficiently low to allow use of the Salpeter approximation.

Integration of eqn. 2.14 over all frequencies shows that total scattered power is proportional to $N (1 + Z \alpha^2)/(1 + (Z + 1) \alpha^2)$; consequently, the effective scattering cross-section is a factor of two lower for the cooperative case than for $\alpha \ll 1$ scattering (when $Z = 1$). Combining eqn. 2.9 with this dependence, the integrated scattered power becomes, for the $\alpha \gg 1, Z = 1$ case of interest

$$P_s = \frac{r_e^2}{2} P_0 n_e \lambda \sin^2 \delta \Delta \Omega \text{ watts} \quad (2.16)$$

where $P_0 = cE_0^2 A/8\pi$ is the incident power in a beam of area A , $n_e = N/V$ and $V = A \lambda$.

For the cooperative case, $\alpha \gg 1$, the second term on the right hand side of eqn. 2.14 represents the ion feature of the scattered spectrum. Scattering originates from the correlated motions of electrons which shield the ions. The first term represents scattering from elec-

tron plasma waves which have frequencies in the range of $\omega_{pe} = (4\pi n_e e^2/m_e)^{1/2} \text{ sec}^{-1}$.

The value of β indicates the spectral shape of the ion feature, which depends upon the magnitude and damping of ion acoustic waves in the plasma. When $T_e = T_i$ ($\beta = 1$) acoustic waves have low amplitude because of strong ion Landau damping. The spectrum is flat-topped with a frequency spread corresponding to ion thermal velocities. As T_e becomes $\gg T_i$, the resonance increases because ion damping decreases so that a more pronounced spike appears in the spectrum at

$$\omega = K \left(\frac{k T_e + 3k T_i}{m_i} \right)^{1/2} \quad (2.17)$$

In this regime, $\Gamma_\beta(\omega/\omega_i)$ gives a qualitative picture of the spectrum, in that it predicts the position of the resonance but not the correct amplitude. In addition, electron Landau damping becomes the dominant damping mechanism for $T_e \gg T_i$.

Most of the scattered power in a cooperative spectrum is contained in the ion feature. Integration of the first term in eqn. 2.14 shows that the power in the ω_{pe} satellites is $\sim 1/\alpha^2$ of the total scattered power.

2.3.3 Magnetic Field Effects on Scattered Spectra

In a magnetized plasma, electrons and ions execute circular motions about B field lines at the respective cyclotron frequencies

$$\Omega_{e,i} = \frac{q_{e,i} B}{m_{e,i} c} \quad (2.18)$$

The spectrum of electron density fluctuations will contain Fourier components corresponding to these frequencies. Consequently, features of the scattered spectra from magnetized plasmas^{5,6} may differ from the $B = 0$ case.

In order to observe these magnetic effects in scattering, the incident wavelength should be long enough so that

$$\alpha_{Be,i} = (\underline{K} \cdot \underline{r}_{Be,i})^{-1} \geq 1 \quad (2.19)$$

where $\underline{r}_{Be,i} = \underline{v}_{e,i} / \Omega_{e,i}$ and may be considered as an appropriate component of \underline{r} in Fig. 2.1 when there is a magnetic field \underline{B} in the \hat{b} direction. This condition means that incident radiation is able to probe the plasma on a scale length \geq the scale of the organized component of n_e fluctuations due to magnetic field gyration effects. Narrowing of scattered spectra by a factor $\cos \phi$ is the general result in this case, ϕ being the angle between \underline{B} and \underline{K} .

Since, for normal values of λ_0 employed in scattering experiments, extremely large \underline{B} fields are required to obtain the foregoing situation, (eqn. 2.19 is equivalent to $\Omega_{e,i} / \omega_{e,i} \geq 1$) the more physically realizable situation is $\alpha_{Be,i} \ll 1$. In this case, \underline{K} must be within an angle $\sin^{-1} \alpha_{Be,i}$ of the perpendicular to \underline{B} to observe magnetic effects in the spectra. If this condition is met, the portion of the scattered spectrum carried by ions will be modulated at multiples of Ω_i and that carried by electrons modulated at multiples of Ω_e , the degree of modulation depending on the perpendicularity of \underline{K} and \underline{B} .

Experimental observation of these effects depends upon scattering detection system design. In all cases, integrated scattered power is not changed from the $B = 0$ case.

2.3.4 Collisional Effects on Ion Spectra

It has been predicted^{3,7} that appreciable narrowing of the ion feature of cooperative spectra will occur for

$$\alpha_{ci} = \frac{\nu_{i-i}}{K \bar{v}_i} > 1 \quad (2.20)$$

where ν_{i-i} is the ion-ion collision frequency. This is equivalent to $\lambda_0 / (4\pi \lambda_{i-i} \sin \theta/2) > 1$, where λ_{i-i} is the ion-ion collision mean free path, so that experimental observation of the effect is restricted to high density low temperature plasmas, and relatively long probe wavelengths.⁸ For example, $n_i \gtrsim 5 \times 10^{16} \text{ cm}^{-3}$ and $T_i \lesssim 1 \text{ eV}$ would be required to obtain $\alpha_{ci} > 1$ for $\lambda_0 = \lambda_{\text{CO}_2} = 10.6 \text{ } \mu\text{m}$, and $n_e \gtrsim 1 \times 10^{13} \text{ cm}^{-3}$ for $\lambda_0 = 6943 \text{ } \text{\AA}$.

2.4 Scattering with CO₂ Lasers

The great majority of laboratory scattering experiments have been carried out with the giant pulse ruby laser, ($\lambda_0 = 6943 \text{ } \text{\AA}$) which can provide several hundred megawatts of power in a 10-20 nsec burst. The pulsed CO₂ laser ($\lambda_0 = 10.6 \text{ } \mu\text{m}$) as a scattering source has some diagnostic advantages over the visible laser, especially with regard to observation of cooperative phenomena in lower density, high temperature

plasmas where only scattering from random electron fluctuations occurs when a ruby probe is used. Considerably more information becomes available if an effective CO₂ scattering system is employed in situations where the ruby could only be used to determine T_e.

To present an important example, recent research into the heating of 10¹⁴ cm⁻³ density plasmas to thermonuclear temperatures (Tokamak machines) has produced a need for additional diagnostics in order to gain an understanding of heating processes. Present methods include $\alpha \ll 1$ ruby scattering⁹ to measure T_e, but density measurements are possible only with an absolute intensity - calibrated detection system. With a 10.6 μ m laser and T_e = 1 keV, $\alpha > 1$ scattering is possible for $\theta < 4^\circ$ and could yield T_i as well as T_e and n_e with no absolute calibration required. In addition, coherent scattering from enhanced electron and ion waves could be used to study turbulent heating in toroidal plasmas. Finally, the longer wavelength would permit magnetic modulation scattering experiments providing a means of determining B fields in Tokamaks.

The CO₂ infrared laser was adopted for the scattering experiments described in this work, in hopes of developing a suitable technique for cooperative scattering from 10¹⁴ - 10¹⁵ cm⁻³ plasmas.

Besides the potential information recovery, further factors tend to make cooperative scattering at 10.6 μ m an attractive proposition. As the most powerful coherent source in the intermediate and far infrared, the CO₂ pulsed laser can provide power levels of > 10⁹ watts, comparable to available ruby powers. In obtaining a cooperative scattered spectrum, use of the 10.6 μ m source permits viewing at a much larger angle θ than would be possible with a visible laser. An important

consequence is greatly reduced stray light problems in detection, which, for small angle scattering, could be a deciding factor as regards experimental feasibility. Other advantages result due to larger θ for longer λ_0 . Collection solid angle $\Delta \Omega$ increases at least as θ does and as θ^2 for small θ . For a given cooperative α , spectral widths $\Delta \lambda$ increase \sim as $\lambda_0 \theta$, whereby required resolution $\Delta \lambda / \lambda_0$ is proportional to θ , and is thus a less demanding requirement at longer wavelengths. IR monochromators and Fabry-Perot interferometers of quality and efficiency equal to that of visible instruments may be used to provide the necessary resolution of scattered spectra.

These benefits help to balance lower detector responsivity and greater photon noise for $10 \mu\text{m}$ detection than for the visible. Photoconductive IR detectors are capable of a few amps/watt responsivity as compared to a few $\times 10^4$ amps/watt from photomultipliers. This difference is slightly offset by higher detector quantum efficiency at $10 \mu\text{m}$ ($\sim 40\%$ versus $\sim 75\%$ at 6943 \AA). Plasma emission, while often the limiting noise source for ruby laser scattering detection, is not a problem at $10 \mu\text{m}$ because of the λ^{-2} dependence in bremsstrahlung intensity. A more serious noise problem exists in the $10 \mu\text{m}$ region with regard to blackbody room temperature (300°K) radiation pickup by detectors which are commonly cooled to liquid N_2 temperatures (77°K) or lower. Such noise can be reduced, however, by placing a similarly cooled optical bandpass filter immediately before the detector chip, keeping in mind the requirements for transmission of scattered photons.

Another factor worthy of mention is increased absorption of longer wavelength radiation, which may lead to unwanted disturbance of the plasma. This subject is discussed in detail in Chapter V, wherein

it is shown that 10.6 μm absorption presents no problems in this regard for $n_e \sim \text{few} \times 10^{15} \text{ cm}^{-3}$, $T_e > \text{a few eV}$, and focussed CO_2 laser intensities of up to $10^{10} \text{ watts/cm}^2$.

2.5 CO_2 Scattering from a Hollow Cathode Arc Plasma

Originally it was proposed to observe Thomson scattering from a hollow cathode argon arc plasma¹⁰ having $T_e = 5 \text{ eV}$, $T_i = 0.5 \text{ eV}$ and a maximum electron density of $5 \times 10^{13} \text{ cm}^{-3}$. A 1 MW, 200 nsec pulsed CO_2 laser served as radiation source (see Chapter III). The plasma chamber was designed such that either $\alpha = 0.3$ or $\alpha = 2$ scattering could be observed from an interaction length of 1 cm over a solid angle of 3×10^{-2} sterr. From eqn. 2.16, the integrated scattered power expected in the cooperative case was 5×10^{-8} watts. Unfortunately, efficient collection of this radiation by the detection optics was not possible and photons reaching the detector did not produce an observable signal above the existing background noise and stray laser light.

In order to provide sufficient scattered power for resolution of spectra, it was decided to increase both laser power and plasma density. Development of a new plasma facility and laser system followed, and these are described in the next Chapter.

CHAPTER III

PLASMA FACILITY AND CO₂ LASER SYSTEMS3.1 Outline

The development of a 10 kW magnetized d.c. argon arc plasma is described. Design of the arc chamber and electrodes was such that long term stable operation was possible. Probable plasma density was a few $\times 10^{15}$ cm⁻³, perhaps two orders of magnitude greater than the hollow cathode arc density. Magnetic field profiles and pressure-volt-ampere characteristics for the arc are given. A reliable method of arc striking is also described.

Parameters of CO₂ TEA lasers intended for use in scattering experiments are summarized. In particular, two schemes for increasing the original 1 MW laser power are described. Resulting temporal pulse shape and wavelength spectral information is presented.

3.2 Argon Arc Plasma Facility3.2.1 General Requirements

The development of a plasma device suitable for a CO₂ Thomson scattering experiment followed, to some extent, the design of Jassby¹ for a magnetized d.c. arc in argon gas. A steady state plasma was more desirable than a pulsed discharge as spatial and temporal re-

producibility problems were eliminated. Also, the existence of the hollow cathode arc chamber and electromagnets facilitated the experimental steps leading to conversion to a higher current, higher density arc.

A plasma density 1 - 2 orders of magnitude greater than that in the hollow cathode discharge was desired. Thus operation in a few Torr of gas was necessary and at d.c. currents of several hundred amperes. Argon was chosen as the working gas for two reasons. First, the relatively low ionization potential (15.7 eV) resulted in minimum electrical dissipation for a given plasma density. Second, its chemical inactivity made for maximum electrode lifetime, a factor which mitigated against hydrogen.

The available power supply was a welder unit which could drive over 300 A at 40 V with a 100% duty factor. A 1 cm diameter tungsten-tipped electrode similar to those used in laboratory plasma jets² initially served as a cathode and a flat 2.5 cm diameter copper plate was used for the anode.

3.2.2 Initial Development

First attempts to strike an arc using a 2 kV radio frequency (RF) field to preionize an electrode gap of 10 - 15 cm were unsuccessful. It became evident that the 0.5 kG axial magnetic field of the hollow cathode arc was inadequate for confinement of a discharge in this higher pressure range. The electromagnets were powered by a 120 V d.c. generator and dissipated 4.5 kW. As a larger supply was not available to drive greater magnetizing currents, a stronger B

field was produced by inserting mild steel pole pieces into the bore of each magnet. These steel cores were tapered such that the field was focussed in the electrode gap, which was decreased to 6 cm. Hall probe measurements showed $B = 2.5$ kG at the minimum field point, an increase of a factor of 5. The field profile is plotted in Fig. 3.1.

With the stronger confining field, it proved possible to strike a stable arc, initial success occurring for $P = 1$ Torr, $I = 250$ A and $V = 40$ V. With this established, the next step was achievement of long term operation of such a discharge.

3.2.3 Arc Chamber and Electrode Design

An aluminum vacuum chamber was constructed (see Fig. 3.2) with sufficient water cooling to maintain wall temperatures below 35°C . Further chamber design features for accommodation of scattering measurements on the arc are discussed in detail in Chapter VI. Also, see Fig. 6.3. Exposed faces of the pole pieces were cooled to avoid possible deterioration of magnetic properties through excessive heating. A port was provided for connection to a 500 μ /min mechanical pump capable of evacuating the chamber to < 0.1 Torr. To afford a view of the discharge as well as enable general access to the chamber interior, a 12 cm diameter port was included and sealed with a thick Pyrex window.

Electrode design was of prime importance. The 2% thoriaated tungsten cathode eventually adopted was 1 cm in diameter, silver

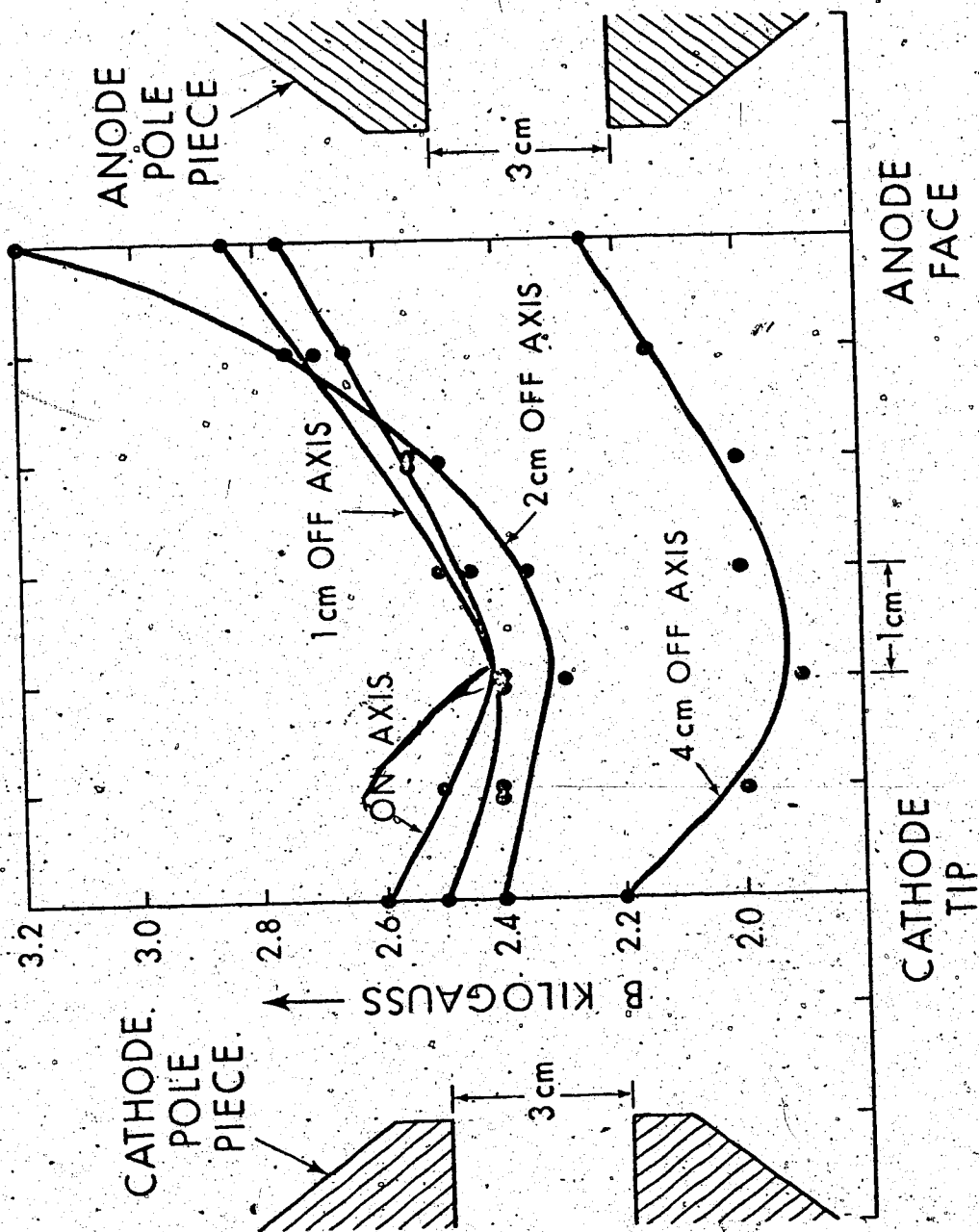


Fig. 3.1 Magnetic field strength in the arc region as measured with a Hall probe.

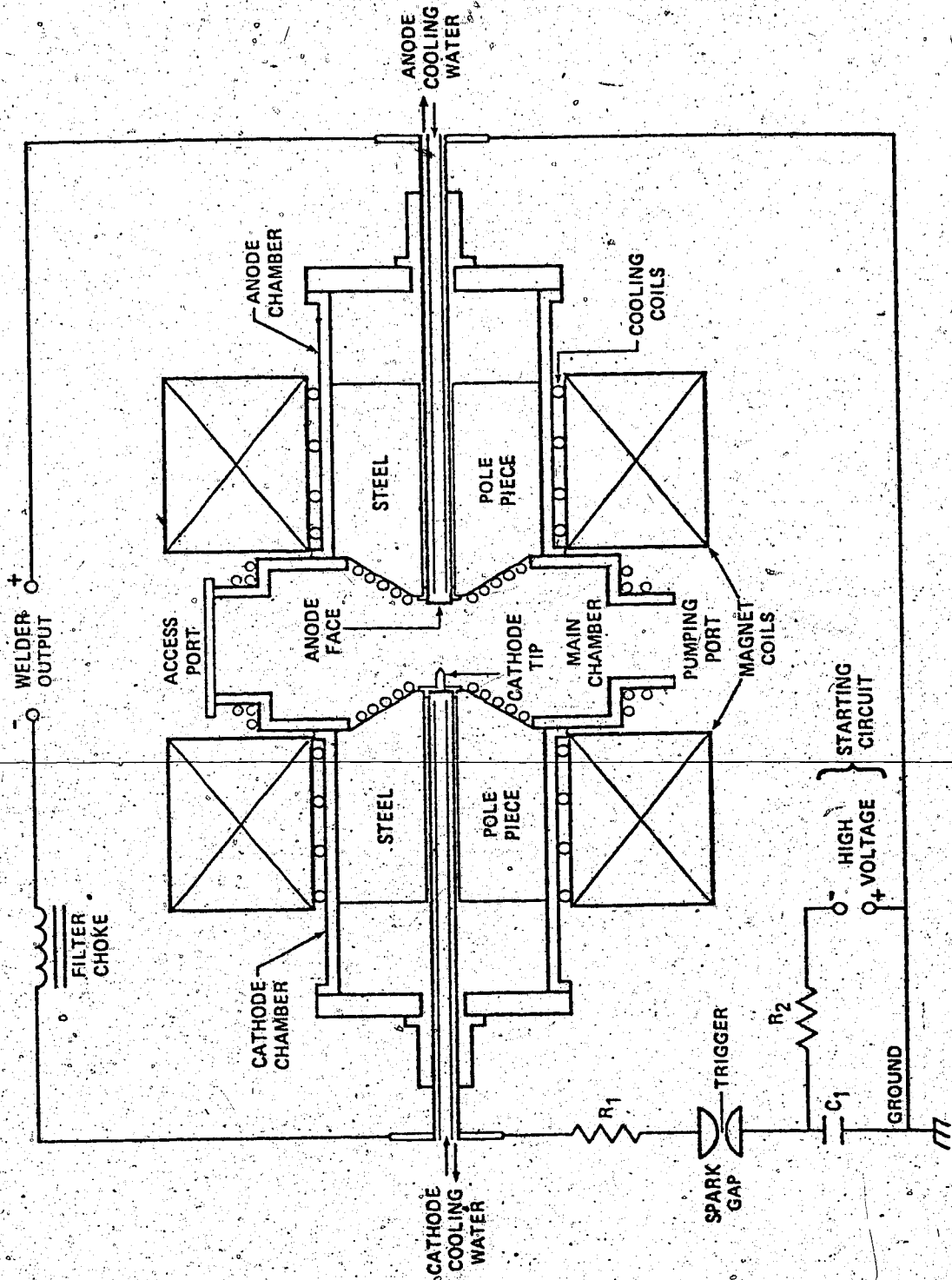


Fig. 3.2 Arc chamber assembly and striking circuitry.

soldered to a 2.5 cm diameter copper tube and water cooled at 15 l/min to ensure no boiling occurred at the hot end. Similar water flow was supplied to the copper anode. Both electrodes were electrically isolated from the pole pieces.

3.2.4 Electrical Characteristics

Operation of this plasma facility for periods of several hours was possible, arc current and voltage holding constant within 5%. In order to avoid buildup of contaminants, gas was pumped continuously through the chamber, although shorter term operation with a static backfill was also possible. Lifetime of the tungsten cathodes ranged from 50 to 100 hours depending on the arc current.

A stable arc could be established in pressures ranging from 0.5 Torr to 10 Torr. For lower pressures, the welder voltage was insufficient to sustain the arc, while above 10 Torr, the magnetic field was apparently too weak to maintain an ionized column. In fact, for $I > 250$ A, the current channel began to bulge midway between the electrodes when the pressure rose above 4 Torr. In addition, it was observed that operation at any pressure was impossible if the field dropped below 2 kG, further indication that the maximum field strength was just adequate for confinement. A photograph of the arc is shown in Fig. 3.3.

Arc volt-amp characteristics are displayed in Fig. 3.4 for various background pressures. In contrast to Jassby's arc, it was found that two stable modes of operation existed for a given pressure. The current channel was more constricted in the higher voltage mode and



Fig. 3.3 Photograph of argon arc. $P = 3$ Torr, $I = 265$ A, $V = 30$ V.

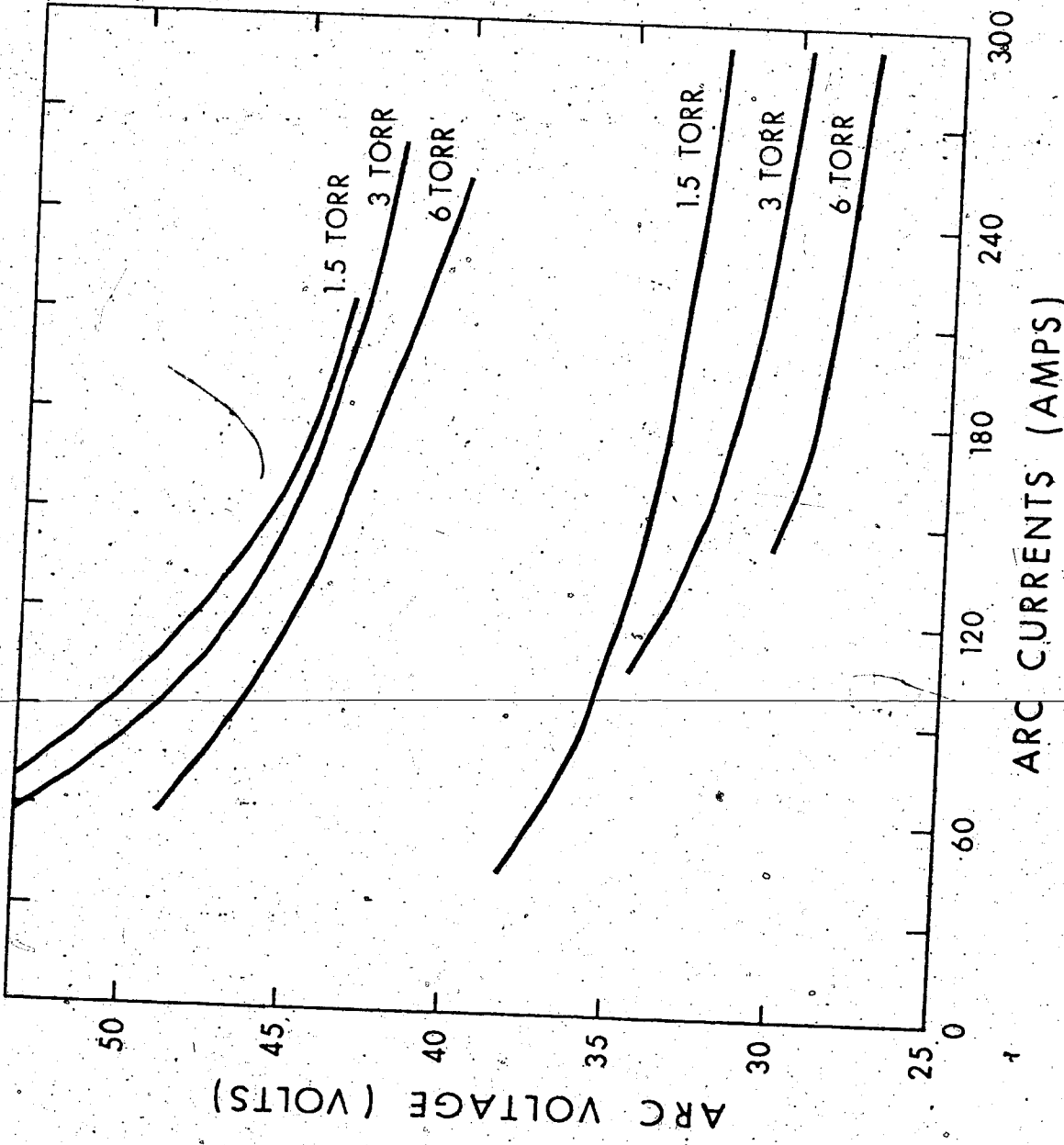


Fig. 3.4 Arc volt-amp characteristics.

thermal emission appeared to be confined to the tip of the tungsten cathode. In the more common low voltage mode, thermionic emission from the entire cathode surface was observed.

Very low frequency ($0.5 \text{ Hz} < f < 5 \text{ Hz}$) rotations of the current channel about the anode-cathode axis have been occasionally observed. This instability has occurred only in the low voltage mode for $P > 4 \text{ Torr}$ and $I > 150 \text{ A}$. A detailed study of these rotations has not been done. There may be some dependence upon the exact arc length or the shape of the cathode tip because the instability was usually not present under the P-I-V conditions mentioned above.

3.2.5 Arc Striking

A capacitive discharge circuit for starting the arc is included in Fig. 3.2. It was adopted due to the unreliability of the RF voltage for this purpose. RF striking was difficult at the lower background pressures and generally became less successful as cathode wear increased.

Two basic factors are involved in striking such a high current arc. Ionization must occur in the electrode gap to provide a current path for the low voltage main supply and must be maintained long enough to initiate thermionic emission through cathode bombardment. The overall process is aided by the magnetic field which tends to prevent diffusion of ions from the electrode gap.

Essentially 100% reliability in starting was achieved by discharging the $250 \mu\text{F}$ capacitor C_1 across the electrode gap. A cur-

rent limiting series resistor $R_1 = 7 \Omega$ stretched the discharge time to several milliseconds. A 500 V charge was normally sufficient to strike the arc.

Stabilization of arc electrical parameters typically occurred within a few seconds after starting, with volt-amp values being reproduced on each start for a given argon pressure.

3.3 CO₂ Pulsed Lasers for Scattering

3.3.1 Oscillator- Amplifier System

The original laser oscillator constructed for use as a Thomson scattering source was of the helical TEA discharge type³. This provided a peak laser power of 1 MW or an intensity of 5×10^7 watts/cm² when focussed through the plasma axis by a 50 cm focal length mirror. Parameters for this laser are included in Table 3.1.

A Rogowski profile, UV preionized TEA discharge unit⁴ was constructed for amplification of the oscillator output. This type of discharge has a peak small signal gain of $> 0.04 \text{ cm}^{-1}$, but the high input power density from the oscillator gave rise to saturation effects. Over a path length of 160 cm (triple pass through the amplifying medium) an energy gain of ~ 7 and a peak power gain of ~ 10 were obtained for the TEA oscillator input. Thus, some temporal sharpening of the oscillator pulse occurred. Oscillograms of a typical oscillator pulse shape and that of the amplified beam are shown in Fig. 3.5 (a) and (b) respectively. A gold-doped germanium IR detector with a risetime of $< 2 \text{ nsec}$ was used to

| | | HELICAL TEA LASER | ROGOWSKI AMPLIFIER | OSCILLATOR AMPLIFIER TANDEM | TWO DISCHARGE OSCILLATOR |
|------------------------------|---|-------------------------|---|-----------------------------------|--------------------------------|
| DISCHARGE PARA- METERS | ELECTRICAL ENERGY INPUT (J/g) | 25 | 250 | 25/250 | 25/250 |
| | E/P (volts/cmTorr) | 16 | 36 | 16/36 | 16/36 |
| | He:CO ₂ :N ₂ (% by volume) | 85:10:5 | 72:21:7 | 85:10:5 72:21:7 | 72:21:7 |
| CAVITY PARA- METERS | LENGTH (m) | 3.3 | 50x5x3.7cm ³ ACTIVE VOLUME | 3.3 | 6.7 |
| | AXIAL MODE SPACING (MHz) | 45 | | 45 | 22 |
| | BACK MIRROR REFLECTIVITY (%) | ALUMINUM ~ 100 | | ALUMINUM ~ 100 | ALUMINUM ~ 100 |
| | BACK MIRROR FOCAL LENGTH (m) | 10 | | 10 | 10 |
| | FRONT MIRROR REFLECTIVITY (%) | GERMANIUM 70 | | GERMANIUM 70 | SODIUM CHLORIDE 8 |
| | FRONT MIRROR FOCAL LENGTH (m) | ∞ | | ∞ | ∞ |
| OUTPUT PARA- METERS | ENERGY (J) | 0.45 | | 3.0 | 2.3 |
| | PEAK POWER (MW) | 1 | | 10 | 20 |
| | 10.6 μm TRANSITION | P(14)-P(22) | | P(14)-P(22) | P(20) |
| | BEAM DIAMETER (cm) | 0.7 | | 1.2 | 0.8 |
| | MULTI-SHOT LINewidth (Å) | 0.9 | | 1.2 | 1.2 |

TABLE 3.1 PARAMETERS OF CO₂ PULSED LASERS USED FOR SCATTERING STUDIES.

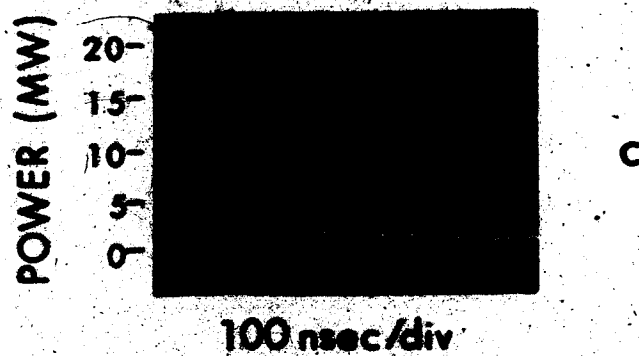
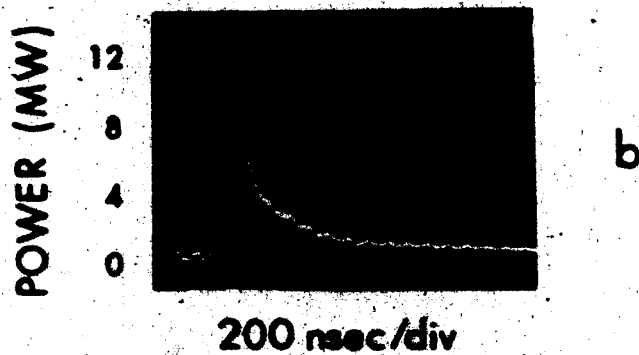
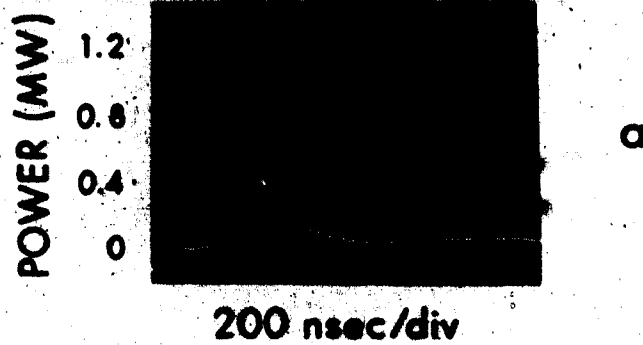


Fig. 3.5 CO_2 laser pulse shapes for; (a) helical TEA laser; (b) oscillator-amplifier configuration; (c) 6.7 meter two discharge laser oscillator

obtain these temporal profiles. Oscilloscope bandwidth was 20 MHz (17 nsec risetime) so that oscillator self mode-locking, which was present in varying degree from shot to shot, was electronically integrated out. For the 3.3 m cavity length, the longitudinal mode spacing was 45 MHz. Amplification removed a considerable portion of the mode-locked pulse structure.

Reliable synchronization of oscillator and amplifier discharges was required, both to place the oscillator pulse near the peak of the amplifier gain profile and to prevent arcing in the Rogowski section. A graphite anode was employed in this unit and tiny carbon particles in the active volume provided sites for ionization via absorption of oscillator photons. If sufficient oscillator power was generated prior to initiation of the amplifier discharge, the result was localized preionization and subsequent arcing.

Low jitter (< 50 nsec) variable delay electronic trigger circuits were used to set the optimum synchronization of discharges. This was also dependent on long term regulation of spark gap pressures in the discharge circuitry.

The helical TEA laser could oscillate on one of several 10 μm P branch CO_2 transitions, but P(20) was selected by cavity mirror adjustment, since the narrowband filter used in conjunction with the detector for scattering measurements had maximum transmission at this wavelength ($\sim 10.59 \mu\text{m}$). In amplification, both the oscillator transition and transverse mode pattern were preserved. With the TEA amplifier, lasing was observed to occur 100 - 200 nsec sooner than for the oscillator alone. This was attributed to a photon injection effect⁵, whereby random photons generated in the amplifier active volume entered the oscillator cavity, inducing an earlier gain buildup.

The amplified beam was somewhat larger in cross-section than the oscillator output (see Table 3.1). Stronger amplification of the lower power edges of the input beam was the probable cause. With an $f = 50$ cm mirror, the beam could be focussed to a 2 mm diameter spot in the plasma chamber, for a resulting peak intensity of 3×10^8 watts/cm². Further amplifier parameters are included in Table 3.1.

3.3.2 Two Discharge 6.7 Meter Oscillator

Combination of the two discharges into a 6.7 m oscillator cavity with a NaCl etalon for output coupling yielded typically 2.3 joules in a pulse of 20 MW peak power. About half the energy was in the initial gain-switched spike. A typical pulse shape is shown in Fig. 3.5 (c).

Lasing was observed only on the P(20) transition. Because the same 10 m focal length back mirror was used in this longer cavity, the output beam diameter was smaller than that of the oscillator - amplifier configuration. It could be focussed to approximately a 1.7 mm spot in the plasma arc, for a peak intensity of 7×10^8 watts/cm².

Discharge synchronization was again important for the reasons stated previously. The 8% feedback was sufficient to generate oscillation with the pin discharge operating alone. (~ 0.09 joules output and peak power of a few hundred kW).

Both oscillator - amplifier and 6.7 m oscillator were used in Thomson scattering measurements.

3.3.3 Laser Line Spectra

Monochromaticity of the laser output is important for use in Thomson scattering experiments since the laser linewidth must necessarily be less than scattered spectral widths. Assuming ~ 1 eV ion temperatures in an argon plasma, the ion feature of a cooperative scattered spectrum is of the order of a few \AA in width for a $10.6 \mu\text{m}$ incident source. Multi-shot scans of laser wavelength spectra for the (20) transition are shown in Fig. 3.6, and spectral widths (FWHM) listed in Table 3.1. Apparently, the TEA laser longitudinal modes would vary from shot to shot, so that averaged over many shots, the spectrum is considerably wider than that of a single pulse^{6,7}. Since in obtaining scattered spectra, averaging over many shots was necessary for signal to noise improvement (see Chapter VI), the characteristic linewidth to be contended with was that of the multi-shot spectrum. As measured laser linewidths were only somewhat less than probable scattered widths, convolution of profiles was eventually necessary for accurate reduction of experimental Thomson scattering data.

The spectra in Fig. 3.6 were obtained by slow scanning of an infrared Fabry-Perot interferometer. Details of this instrument's operation are given in Chapters IV and VI. It was not possible to scan quickly enough to observe single shot spectra. Linewidths quoted in Table 3.1 were calculated by subtraction of the Fabry-Perot instrumental width (0.3\AA FWHM) from the widths of depicted experimental profiles, assuming Lorentzian shapes in all cases. Linewidth of the 6.7 m oscillator was \sim equal to that of the oscillator - amplifier configuration.

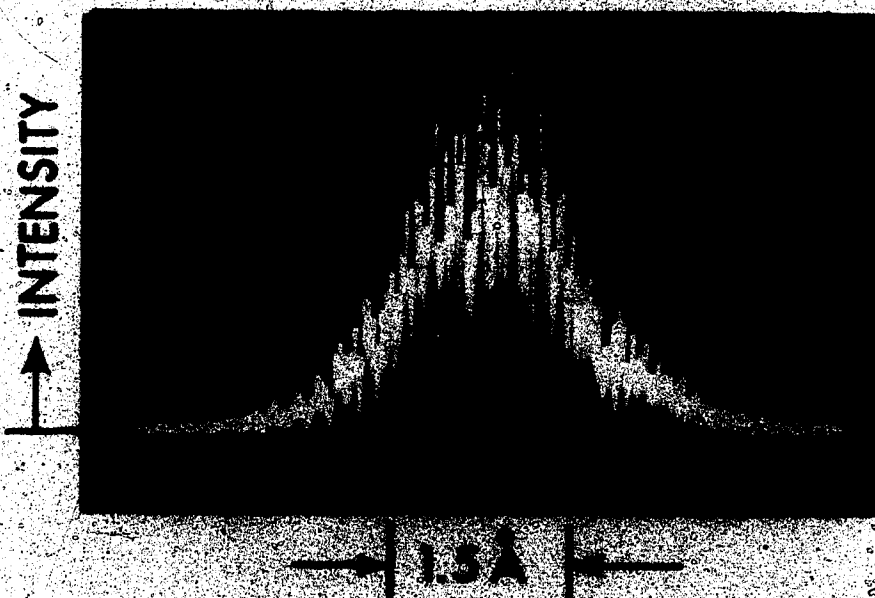
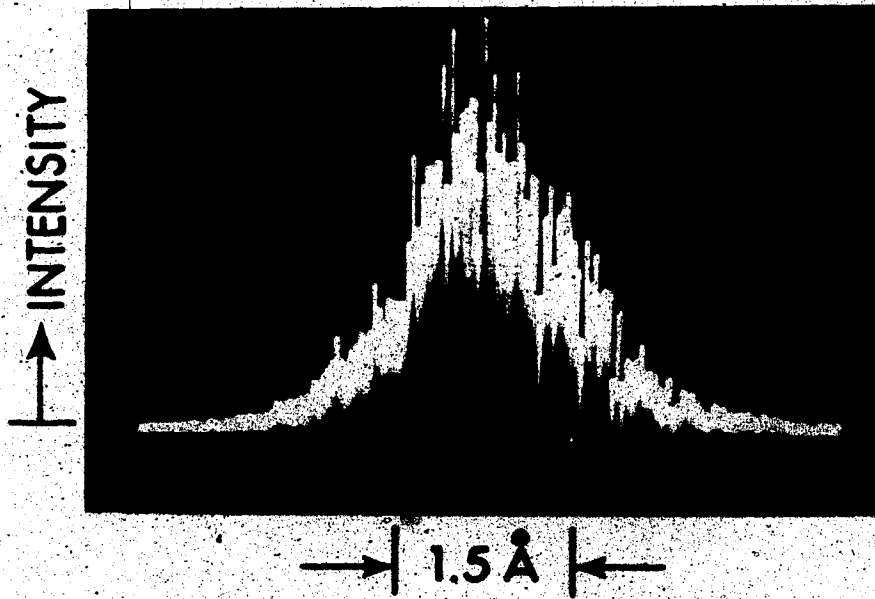


Fig. 3.6 CO₂ laser multi-shot wavelength spectra for: (a) helical TEA laser; (b) amplified helical TEA laser (similar to 6.7 m laser oscillator). Instrument width was 0.3 Å.

3.4 Conclusions

With increases in laser power and energy, and in plasma density, the outlook for Thomson scattering was considerably brighter. In the following Chapter, detailed measurements of arc plasma parameters are documented, providing the necessary information for design of the scattering experiment.

CHAPTER IV

PROBE AND SPECTROSCOPIC DIAGNOSTICS

4.1 Outline

Measurements of the plasma parameters of the argon arc were carried out using electrostatic probe and spectroscopic methods. Besides providing some useful knowledge which would facilitate the design of Thomson scattering experiments, use of these diagnostic techniques served to increase the body of data for this type of plasma arc.

Plane wire probes were designed for application to extreme heat flux conditions and in addition were swept through the plasma to prevent probe damage. Electron density and temperature profiles of the arc cross-section resulted from reduction of probe data. Effects of electron-ion collisions and the magnetic field on the probe I-V curves have been considered.

Spectroscopic measurements were made in both axial and transverse directions. Broadening of singly ionized argon spectral lines was recorded by scanning with a visible Fabry-Perot interferometer and ion temperature was inferred from the thermal broadening contribution. The degree of Zeeman splitting of these transitions as well as some argon neutral lines yielded magnetic field strength in the arc.

Radiation from impurity hydrogen in the arc chamber was detected and broadening of the H_{α} line in particular was measured. Some changes in arc characteristics due to addition of traces of hydrogen were observed.

4.2 Probe Measurements

4.2.1 Introduction

Double-ended tungsten wire probes were constructed and mounted on the shaft of a small d.c. motor. The assembly was placed inside the arc chamber by attachment to an access port cover plate (see Fig. 4.1). These probes were insulated everywhere by alumina and boron nitride with only their flat tips exposed (see Fig. 4.2). Spatially resolved measurements of swept probe currents have enabled determination of n_e and T_e profiles of the arc cross-section approximately midway between anode and cathode.

4.2.2 Probe Theory

With an assumed Maxwellian distribution of electron velocities, collection of electrons by the probe should vary according to

$$I_e \propto n_e e^{eV_p/kT_e} \quad (4.1)$$

where V_p is the probe potential. The plasma density is certainly high

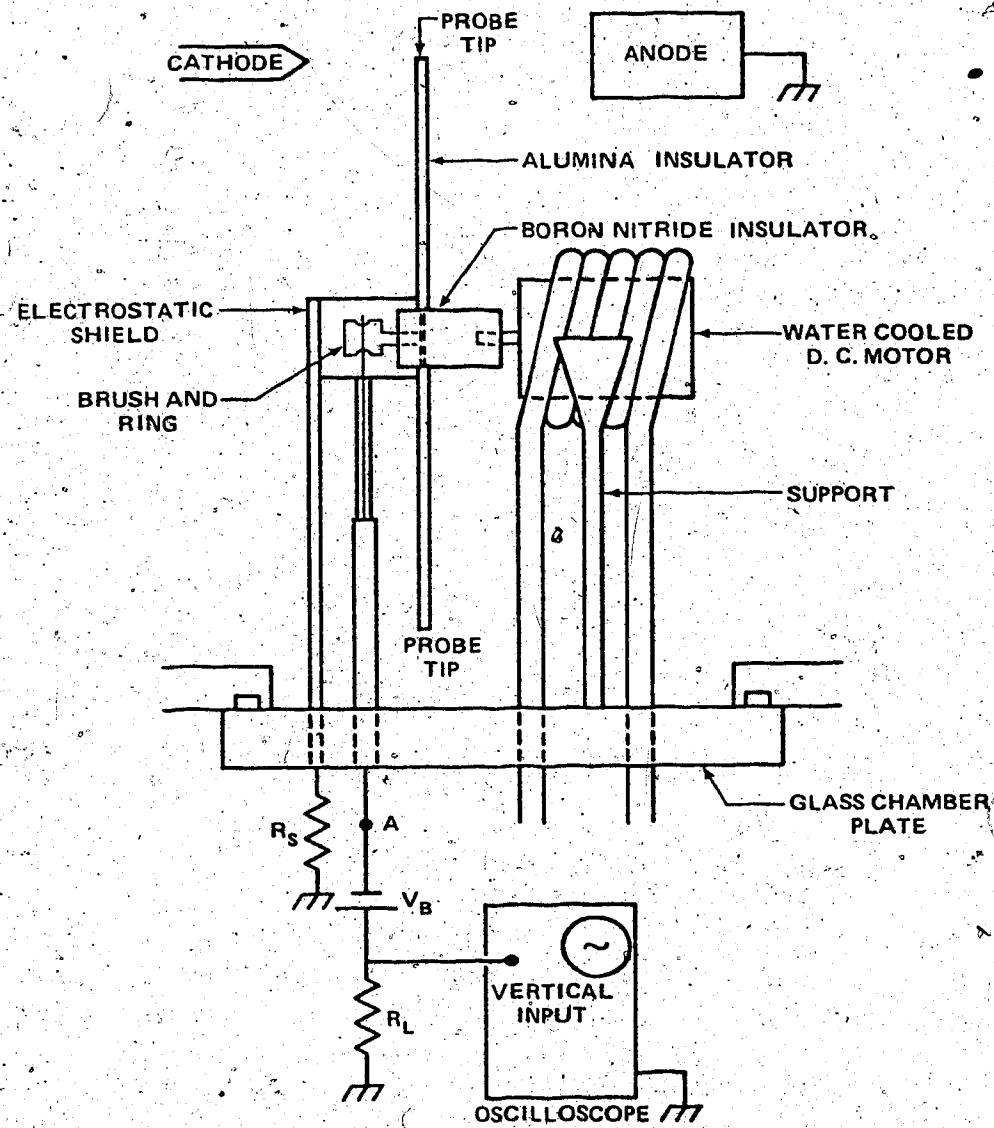


Fig. 4.1 Probe set-up inside the arc chamber.

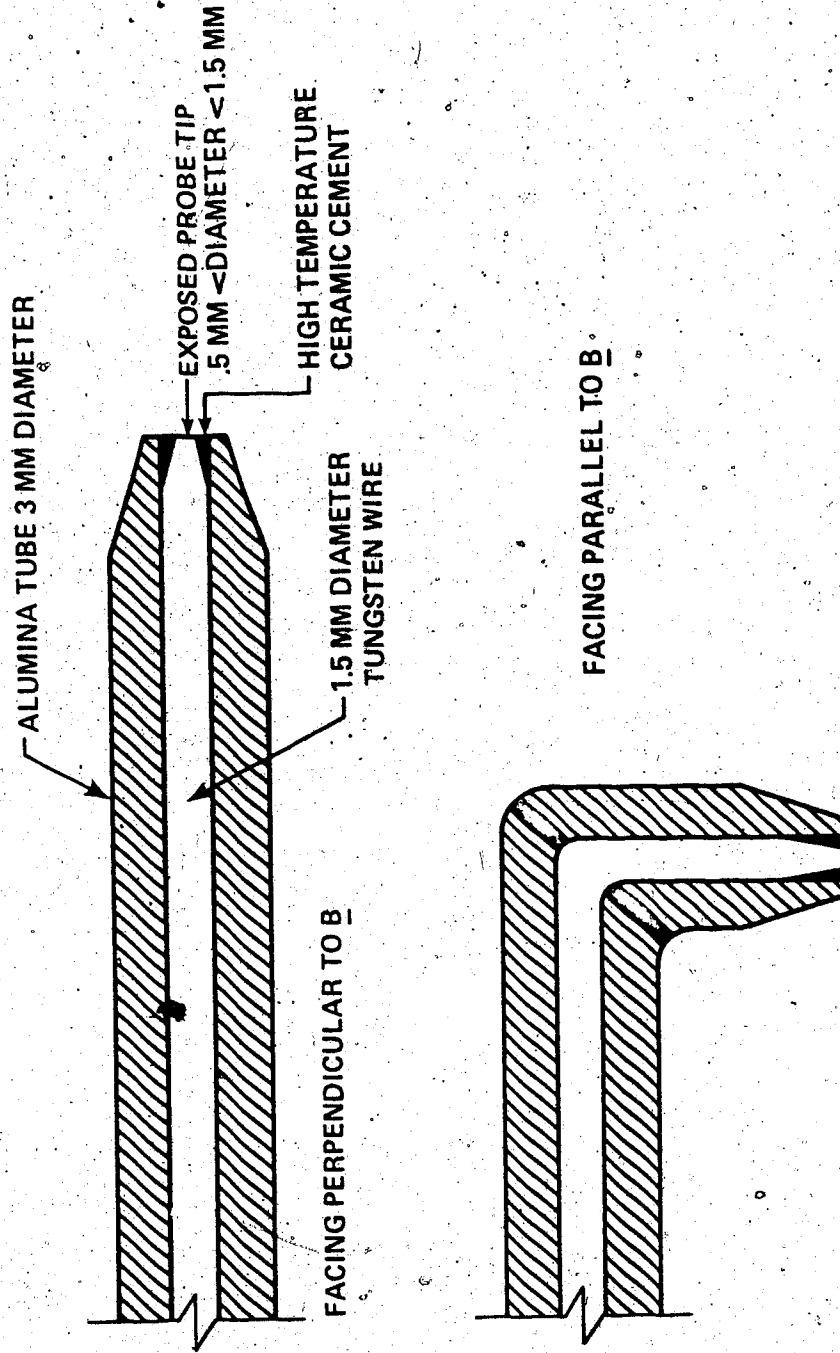


Fig. 4.2 Design of plane probes.

enough that the Debye length is negligible compared to millimeter dimension probes. Current collection under these conditions should be dependent on the product of density and particle velocity; thus the saturation ion current to a strongly negative probe is estimated by¹

$$I_{is} = \frac{0.4 n_e e}{3 \times 10^9} \left(\frac{2k T_e}{m_e} \right)^{1/2} \left(\frac{m_e}{m_i} \right)^{1/2} A_p \text{ ampères} \quad (4.2)$$

where A_p is the probe area in cm^2 . The electron temperature can be found from the slope of a logarithmic plot of relation 4.1, that is, $\ln(I_e - I_{is})$ versus V_p has a slope proportional to T_e^{-1} .

4.2.3 Experimental Method

Probes were positioned to swing through the arc approximately 2.5 cm from the cathode tip at speeds in the vicinity of 10^3 cm/sec, decreasing the probe duty factor to $\sim 10\%$. A slower moving probe was likely to melt or break apart due to the extremely high heat flux from the arc. In fact, the relatively high speed probes occasionally incurred damage in the form of cracking of the alumina insulating tube. Because the probe apparatus was in such close proximity to the arc (< 10 cm from the axis) it was necessary to electrostatically shield the ring and brush (Fig. 4.1) from pickup of large electron currents when the probe was biased strongly positive. With the shield grounded through a high resistance, tests with a dummy probe (no exposed surface) demonstrated the effectiveness of the electrostatic shield, as essentially no pickup current was detected for any positive bias voltage.

Despite water cooling, it was not possible to operate the motor for more than 10 sec in the presence of a discharge. Consequently, the method of operation was to set the bias voltage, strike the arc, then swing the probe through the stabilized plasma column, recording the repetitive current waveform. Later in this investigation, a slow voltage ramp was utilized for the probe bias and it was possible to obtain the entire probe characteristic curve in 1.5 sec. At the same time, an additional feature was incorporated into the probe design. One end was hooked to face parallel to \underline{B} field lines, the other end faced perpendicular to \underline{B} as previously. If some anisotropy in charged particle fluxes existed, it could be expected to be evident in the current collection of such a probe.

4.2.4 Experimental Results

Oscillograms displaying various spatial profiles of probe current corresponding to different probe bias voltages are included in Fig. 4.3. These show the arc to be cylindrically symmetric with respect to properties which may be inferred from the probe current. Typical probe curves showing ion saturation, electron saturation and transition regions are plotted in Fig. 4.4. Carrying out the electron temperature and density calculations according to eqns. 4.1 and 4.2 led to the $n_e - T_e$ profiles of the arc cross-section shown in Fig. 4.5.

The voltage-swept double-ended probe was tested at pressures of 1.3, 3 and 7 Torr and Fig. 4.6 contains oscillograms of probe current versus bias voltage. Actual probe voltage is determined by subtracting the voltage drop across R_L (2.0Ω). Resulting electron temperatures

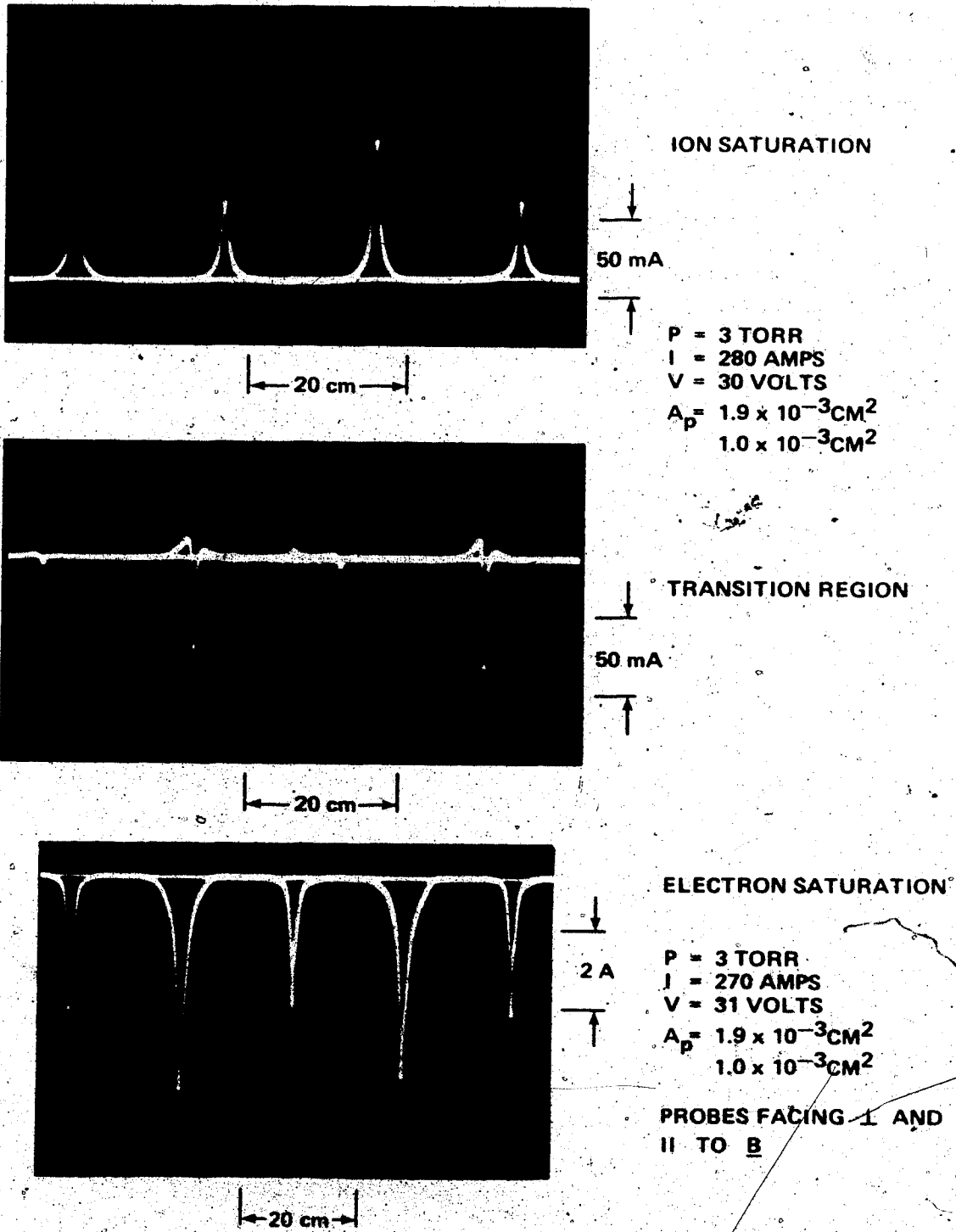


Fig. 4.3 Spatial current profiles for double-ended plane probes.

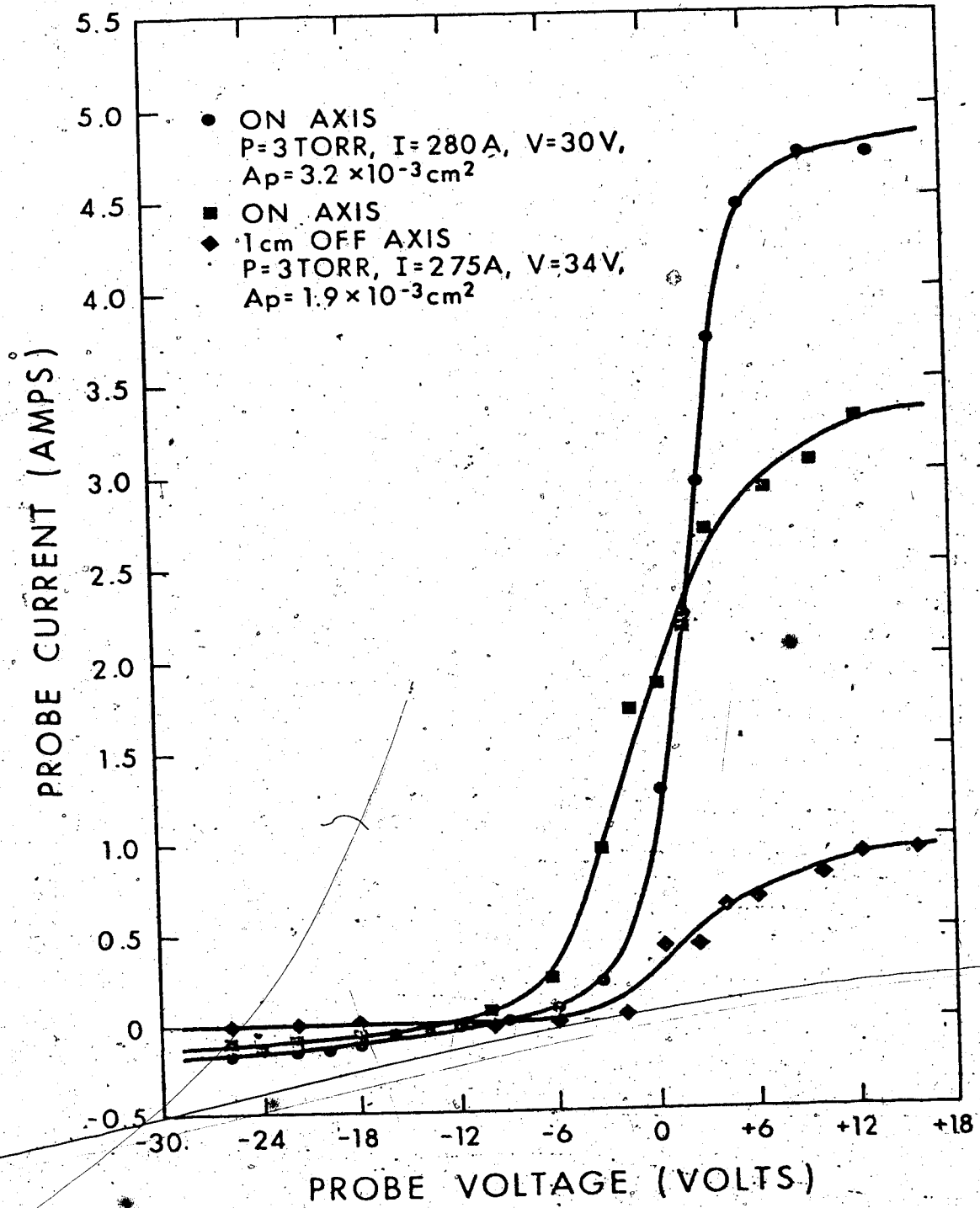


Fig. 4.4 Volt-amp characteristics of swinging probes.

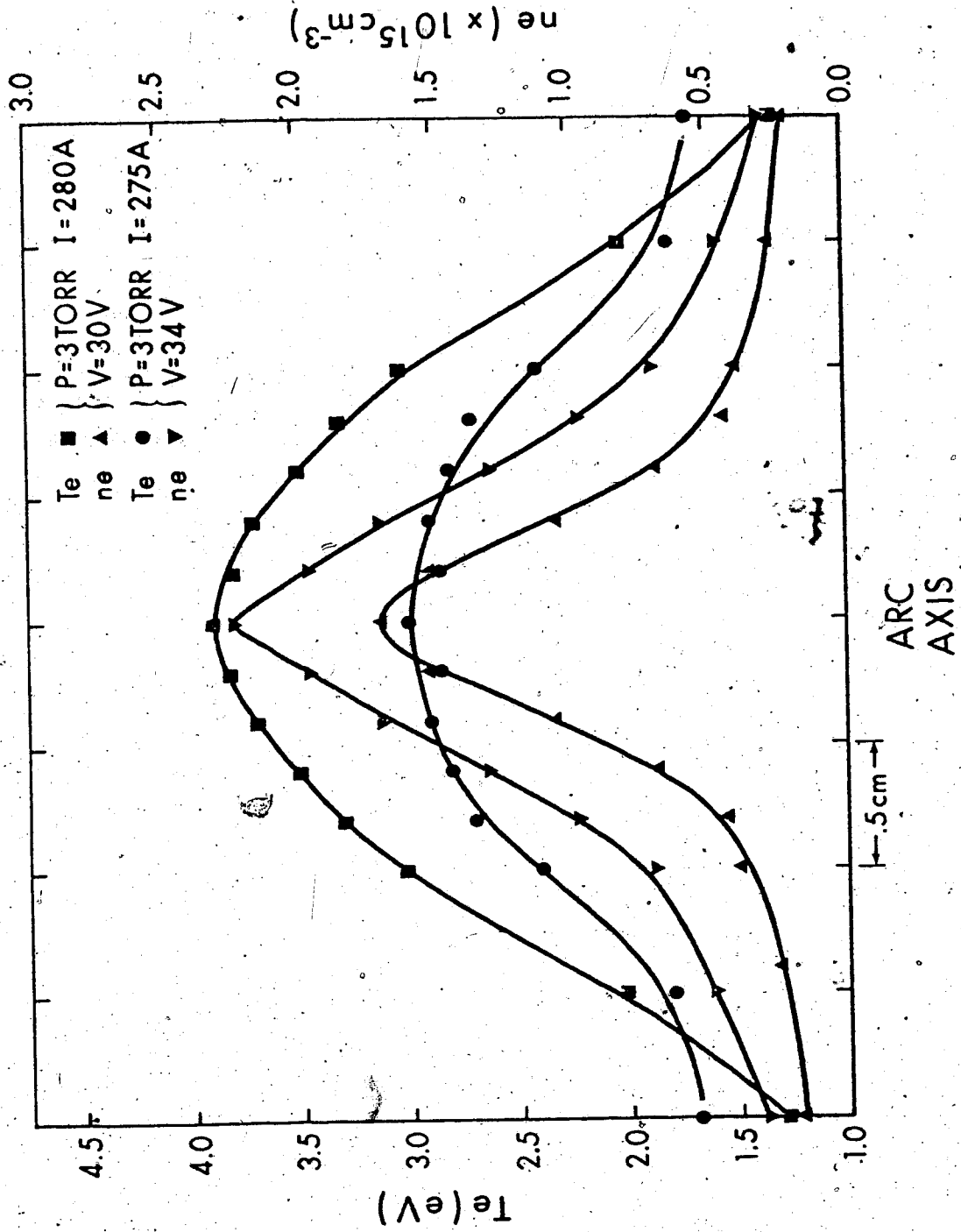
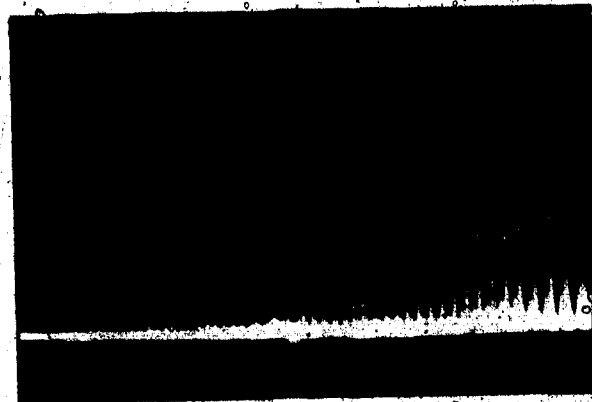


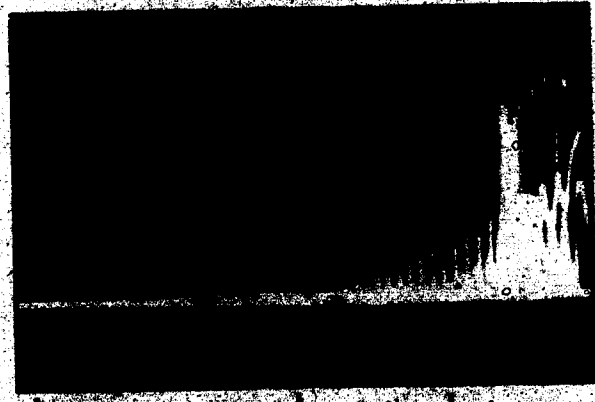
Fig. 4.5 Profiles of electron temperature and electron density across the arc.



P = 1.3 TORR
 I = 250 AMPS
 V = 36 VOLTS
 $T_I = T_{II} = 4.5 \text{ eV}$



P = 3 TORR
 I = 270 AMPS
 V = 31 VOLTS
 $T_I = 4.5 \text{ eV}$
 $T_{II} = 4 \text{ eV}$



P = 7 TORR
 I = 260 AMPS
 V = 28 VOLTS
 $T_I = T_{II} = 4 \text{ eV}$

Fig. 4.6 Voltage-swept probe characteristics. $A_p = 1.9 \times 10^{-3} \text{ cm}^2$ facing I to B, $1.0 \times 10^{-3} \text{ cm}^2$ facing I to B. The larger electron current was collected by the probe facing I to B.

| PRESSURE (torr) | ARC VOLTAGE (volts) | ARC CURRENT (amps) | ION SATURATION CURRENT (amps) | PLASMA CURRENT CHANNEL HALFWIDTH (cm) | PROBE AREA (cm ²) |
|--------------------|------------------------|-----------------------|-------------------------------------|---|----------------------------------|
| 1.5 | 34 | 260 | 1.10 | 1.0 | 1.8x10 ⁻² |
| | 33 | 270 | 0.050 | 1.2 | 7x10 ⁻⁴ |
| 3.0 | 35 | 275 | 1.35 | 1.2 | 1.8x10 ⁻² |
| | 30 | 290 | 0.060 | | 7x10 ⁻⁴ |
| 4.5 | 31 | 270 | 0.90 | 1.3 | 1.8x10 ⁻² |
| | 30 | 275 | 0.050 | | 7x10 ⁻⁴ |
| 6.0 | 28 | 265 | 0.62 | 1.5 | 1.8x10 ⁻² |
| | 28 | 275 | 0.035 | | 7x10 ⁻⁴ |

TABLE 4.1 ION SATURATION CURRENTS

are indicated. In these cases, the parallel end of the probe faced the cathode, however, there was no appreciable difference in the characteristic when this probe faced the anode. This technique has the disadvantage that spatial resolution is lost and only axial information is obtainable.

Ion saturation currents were measured for a range of background pressures using probes facing perpendicular to the magnetic field and the results are recorded in Table 4.1. The half widths of these saturation current profiles are also tabulated and give an indication of the increase in the arc current channel diameter with increasing pressure.

At one point, an attempt was made to use a cylindrical probe of length 1.1 mm and diameter 100 μm . Ion saturation currents of 250 mA collected by this probe corresponded to a density of $2.8 \times 10^{15} \text{ cm}^{-3}$ assuming $T_e = 3.5 \text{ eV}$. Unfortunately, this probe and others similar to it melted immediately when biased to collect electron currents and therefore could not be used to measure T_e directly.

4.2.5 Discussion

For operation at 3 Torr and with arc currents in the range of 260 A - 280 A, peak electron temperatures of between 3 and 4 eV (on axis) have been measured with the plane probes facing perpendicular to B , the temperature falling to 75% of the peak value 1 cm off axis. Peak electron densities were $(2-2.5) \times 10^{15} \text{ cm}^{-3}$ falling to 30% of this 1 cm off axis. For $I > 250 \text{ A}$, peak T_e was $\sim 20\%$ lower at 7 Torr than

at 1.5 Torr, while maximum density was greatest at $P \approx 3$ Torr, falling by $\sim 50\%$ at 7 Torr.

As well as showing comparable peak electron temperatures, the double-ended probe collected approximately equal electron saturation currents, taking into account the different areas of the two probe tips. (see Figs. 4.3 and 4.6). Thus there appeared to be no directional features associated with current collection by the plane probes.

Electron temperatures were taken from the straight line portion of the $\ln(I_e - I_{is})$ versus V_p curves in the electron current region. This would appear to yield the best estimate of T_e since this region of the probe curve encompasses collection of the majority of the current carriers; therefore the bulk of the electron distribution should be characterized by such a temperature. Many of the probe curves appeared to exhibit a "temperature" feature, two straight-line segments on the logarithmic plot. Such a situation is illustrated in Fig. 4.7. A higher temperature was indicated from the probe curve in the region where V_p was close to the plasma floating potential than from the region where electron current dominated. It is likely, however, that the higher temperature is not representative of the bulk of the electron distribution since it is derived from collection of a comparatively small fraction of the electrons, namely those in the high energy tail of the distribution function which may not be Maxwellian.

Interpretation of swinging probe data should be possible in terms of conventional probe theory, but some modification to include the effects of charged particle collisions and magnetic fields may also be necessary, especially with regard to the magnitude of electron

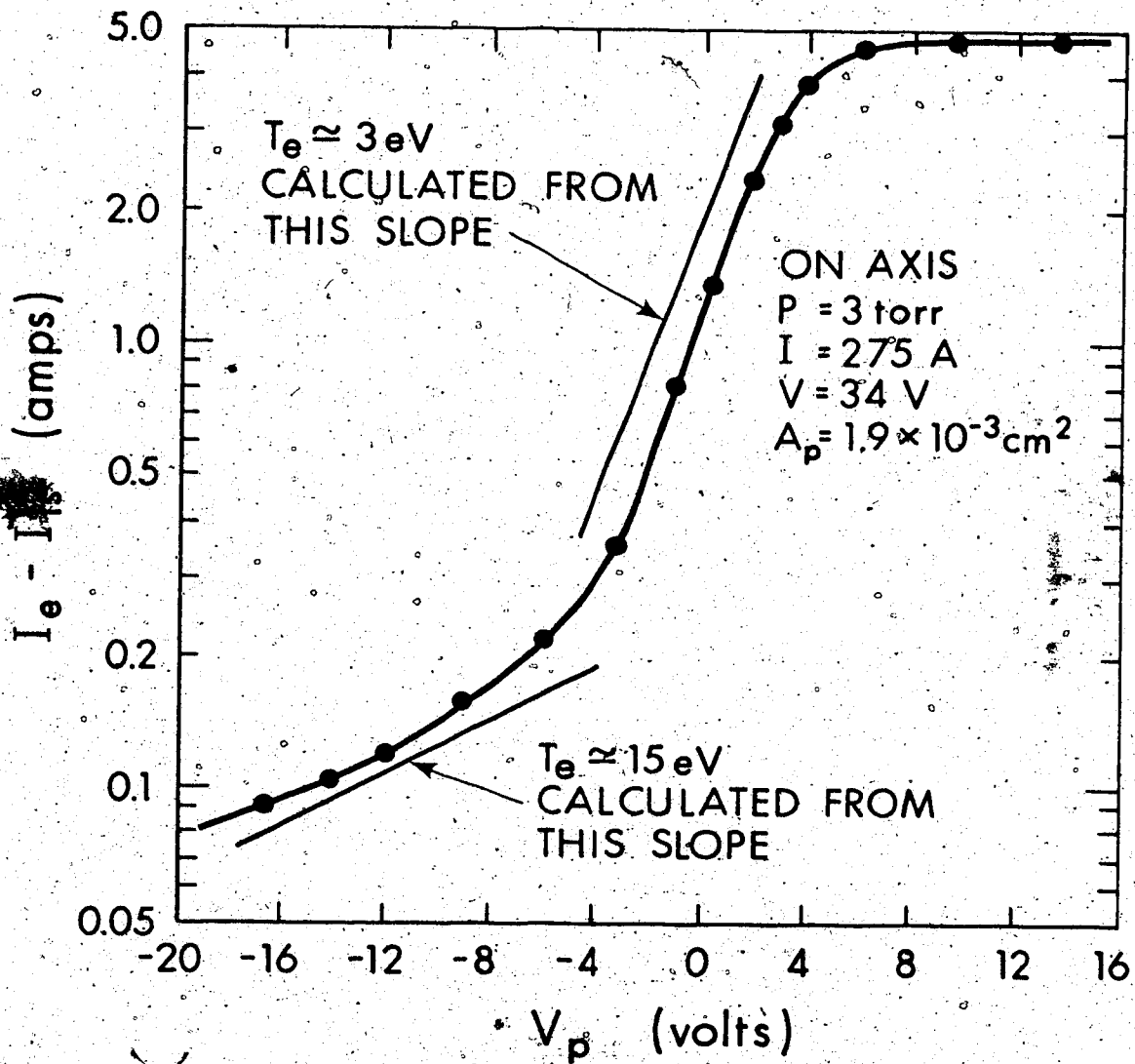


Fig. 4.7 Logarithmic probe current versus probe voltage curve showing "two-temperature" feature.

saturation current. Probe velocities of ~ 1000 cm/sec were insignificant compared with electron thermal velocities

$$\bar{v}_e = \left(\frac{8k T_e}{\pi m_e} \right)^{1/2} \approx 1.3 \times 10^8 \frac{\text{cm}}{\text{sec}} \quad (4.3)$$

for $T_e = 3.5$ eV, and electron drift velocities

$$v_{eD} = \frac{3 \times 10^9 \text{ J}}{n_e e} \approx 3.1 \times 10^5 \frac{\text{cm}}{\text{sec}} \quad (4.4)$$

for $n_e = 2 \times 10^{15} \text{ cm}^{-3}$ and $J = 100 \text{ A/cm}^2$, and so should have had negligible effect on current collection.

Ratios of electron to ion saturation current of 30 - 40 on axis and 50 - 60 1 cm off axis have been observed (see Fig. 4.4), while a collisionless, field-free theory would predict

$$\frac{I_{es}}{I_{is}} = \left(\frac{m_i}{m_e} \right)^{1/2} \approx 270 \text{ for argon} \quad (4.5)$$

Apart from magnetic field effects, when Coulomb encounters between electrons and ions become numerous to the point where mean free paths are of the order of or smaller than probe dimensions, collection of electron currents should be inhibited, with an estimate of the reduction factor given by²

$$\frac{I_{es}}{I_{eso}} = \frac{3}{4} \frac{\lambda}{d} \quad (4.6)$$

where λ is the electron-ion collision mean free path and d is the probe dimension. I_{eso} is the saturation current in the collisionless case.

Ion saturation currents should not be affected by ions colliding with electrons. For $n_e = 2 \times 10^{15} \text{ cm}^{-3}$ and $T_e = 3.5 \text{ eV}$, the m.f.p. is

$$\lambda_{e-i} = (n_e \sigma_{e-i})^{-1} = \frac{15(k T_e)^2}{4\pi n_e e^4 \ln \Lambda} \approx 0.45 \text{ mm} \quad (4.7)$$

where $\ln \Lambda$ is the Coulomb logarithm and $\Lambda = 12\pi n_e \lambda_D^3$. Note that $\lambda_D = 3.1 \times 10^{-5} \text{ cm}$ (eqn. 2.11) for $T_e = 3.5 \text{ eV}$ and $n_e = 2 \times 10^{15} \text{ cm}^{-3}$, which is very small compared to probe dimensions, as mentioned in the discussion on probe theory. In calculating λ_{e-i} it is assumed that the plasma column is essentially fully ionized on axis and that electron collisions with singly charged ions dominate. This approximate value of λ is comparable to the diameters of plane probes which have been used. Therefore collisions alone could possibly reduce I_{es} although it is difficult to calculate the extent of the effect. To first order, the entire electron distribution should be affected by collisions in a similar manner, consequently, the probe curve may still yield the approximate electron temperature.

In a sufficiently large magnetic field, the effective mean free path of charged particles is given by their Larmor radii and saturation currents may be reduced if probe dimensions are appreciably greater. For Ar II ions in a 2.5 kG field, the gyroradius is $\sim 0.5 \text{ cm}$, therefore the field should have no influence upon I_{is} . However, the electron gyroradius r_{Be} is $\sim 3 \times 10^{-3} \text{ cm} \ll d$ and I_{es} may consequently be reduced. An order of magnitude estimate of this decrease, from consideration of classical particle diffusion rates, is given by²

$$\frac{I_{es}}{I_{eso}} \sim \frac{1}{\Omega_e \tau_{e-i}} \approx \left(\frac{\pi}{2}\right)^{3/2} \left(\frac{n_e m_e^{1/2} c e^3 \lambda n \Lambda}{B (k T_e)^{3/2}} \right) \quad (4.8)$$

where $\Omega_e = eB/m_e c$ is the cyclotron angular frequency and τ_{e-i} is the electron-ion collision time. For the present conditions, $\Omega_e \tau_{e-i} \approx 9$, which implies a considerable decrease in I_{es} .

The observed drop in I_{es} from the collisionless field-free case is perhaps explicable in terms of a combined influence of collisions and magnetic fields which both serve to retard the progress of electrons towards a biased probe. Again it is likely that the approximate electron temperature is obtainable from the straight-line portion of $\ln(I_e - I_{is})$ versus V_p curves. It was possible to process current and voltage raw data such that resulting errors in the plots of Figs. 4.4, 4.5 and 4.7 were less than 10%. However, it is very difficult to apply an overall limit of accuracy to the probe technique because of unknown plasma-probe conditions. To our knowledge, biased probes have up to now not been employed in such an arc plasma, and further corroboration of the probe results would therefore be desirable. Spectroscopic measurements of ion temperature discussed later in this Chapter lend credence to a picture of a plasma with $T_e > T_i$, and support the values of T_e obtained from probes.

4.3 Optics for Spectroscopic Measurements

Optical systems were set up for observation both across and along the axis of the arc. In both cases the optical train included a 1/4 m Jarrell-Ash monochromator, a piezoelectrically scanned Fabry-Perot interferometer and an RCA 8645 photomultiplier with an S-20

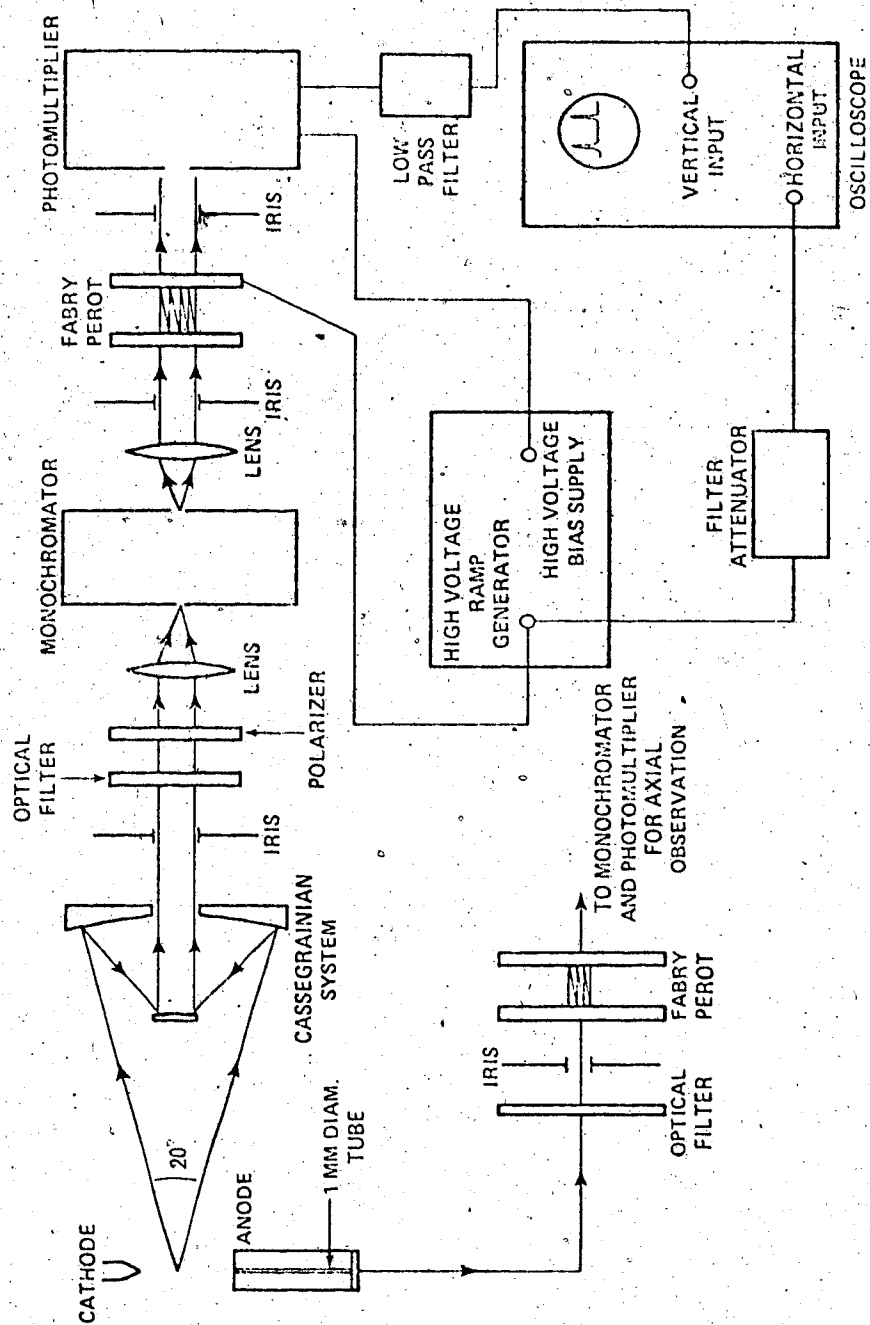


Fig. 4.8 Optical systems for transverse and axial spectroscopic measurements.

photocathode. Details of the optical setup are shown in Fig. 4.8.

For transverse observation, light was collected and collimated by a modified Cassegrainian system. With an $f = 8.2$ cm lens prior to a $150 \mu\text{m} \times 150 \mu\text{m}$ monochromator entrance aperture, it was possible to view a 0.25 mm square plasma cross-section extending through the current channel. Results are therefore averages of properties over this sight line. To facilitate axial observation, an anode was constructed containing a central 1 mm diameter aperture sealed by a small viewing window. In all other respects, this anode was identical to that described in Chapter III. The optics could then view a cylinder of plasma extending from anode to cathode and results are again averages over this line of sight.

Monochromator resolution was $\sim 10 \text{ \AA}$ at 5000 \AA , sufficient for isolation of most argon spectral lines. The Fabry-Perot interferometer was scanned by application of a high voltage ramp to a piezoelectric drive upon which one of the mirrors was mounted. Two sets of mirrors were used; one pair having 90% reflectivity at 6900 \AA and the other with 99% reflectivity at 4800 \AA , enabling resolution of spectral lines from 4200 \AA to 7500 \AA .

4.4 Line Broadening and Splitting

Measurements of the broadening of Ar II spectral lines³ were carried out in order to determine ion temperatures in the arc. Neutral argon lines³ have also been observed in the anode and cathode regions as well as the area peripheral to the current channel, and Zeeman splitting⁴ of both neutral and ion transitions has been used to determine magnetic field values.

The Doppler width of a spectral line of wavelength λ emitted by particles having a Maxwellian velocity distribution is

$$\Delta \lambda_D = 7.68 \times 10^{-5} \lambda (T/M)^{1/2} \text{ \AA FWHM} \quad (4.9)$$

for λ in \AA , T in eV and M in a.m.u. Gaussian line profiles result when this is the dominant broadening mechanism. For Ar II, $M \approx 40$ and broadening of visible lines for \sim eV ion temperatures is $< 0.1 \text{ \AA}$.

When a magnetic field is present, each spectral line is split into several components, the exact number depending upon the quantum numbers of the upper and lower energy levels of the particular transition. These components may be divided into 2 groups, usually denoted by π and σ , according to their polarization. When viewing perpendicular to \underline{B} , the π components, polarized with \underline{E}_π parallel to \underline{B} , are flanked on each side by a group of σ components which have \underline{E}_σ perpendicular to \underline{B} . Each σ group is shifted from line centre by approximately

$$\Delta \lambda_Z = \frac{\Omega_e}{4\pi c} \lambda^2 \approx 4.66 \times 10^{-10} \lambda^2 B \text{ \AA} \quad (4.10)$$

for λ in \AA and B in kG. When viewing parallel to \underline{B} , only the σ components appear, both groups circularly polarized and separated by approximately $2 \Delta \lambda_Z$. Exact separations of line components may be calculated from quantum mechanical considerations. For $B = 2.5$ kG and λ in the visible, Zeeman splitting of argon transitions was comparable to their Doppler widths, and was therefore considered in the unfolding of experimental profiles.

4.4.1 Fabry-Perot Resolution

With widths and shifts of $\sim 0.1 \text{ \AA}$ to contend with, Fabry-Perot resolving powers $> 5 \times 10^4$ were required. Such resolution was easily obtained as high reflectivity mirrors were employed in the instrument.

The free spectral range of a Fabry-Perot is given by

$$\text{FSR} = \lambda^2 / 2d \quad (4.11)$$

where d is the mirror separation. To prevent overlapping of orders, typical FSR of $\sim 0.5 \text{ \AA}$ was used, corresponding to $d \sim 0.3 \text{ cm}$. For experimental runs, exact mirror spacing was determined by comparison of measured wavelength separations of closely spaced Ar II lines with data from accurate wavelength tables³.

Optimum finesse for mirrors of reflectivity R is

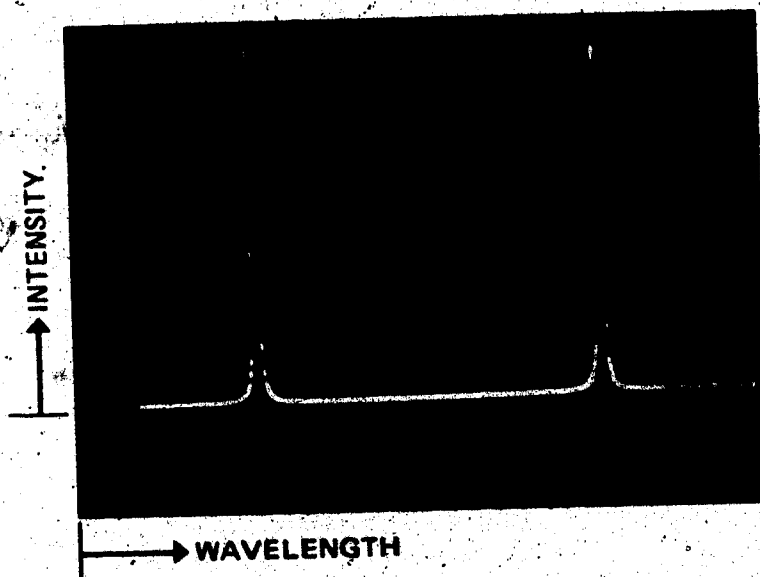
$$F = \pi \sqrt{R} / (1-R) \quad (4.12)$$

and the upper limit of resolving power is then

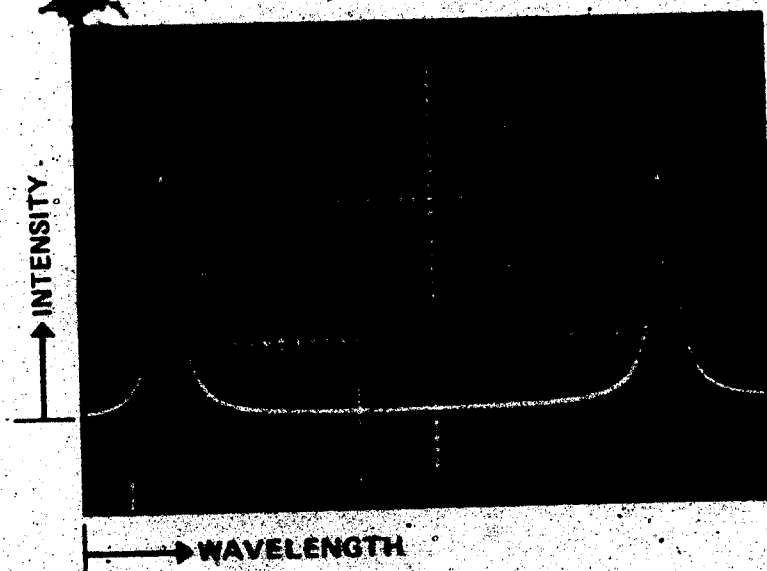
$$\text{RP} = \frac{\lambda F}{\text{FSR}} = \frac{2\pi d \sqrt{R}}{\lambda (1-R)} \quad (4.13)$$

For $d = 0.3 \text{ cm}$, $\text{RP} \approx 3.9 \times 10^6$ for $R = 0.99$ at 4800 \AA and 2.6×10^5 for $R = 0.90$ at 6900 \AA . Both figures are then much higher than required resolving power.

In actual practice however, RP may be limited by the quality



HELIUM - CADMIUM
LASER $\lambda = 4416 \text{ \AA}$
FREE SPECTRAL
RANGE = $.417 \text{ \AA}$



HELIUM - NEON
LASER $\lambda = 6328 \text{ \AA}$
FREE SPECTRAL
RANGE = $.480 \text{ \AA}$

Fig. 4.9 Typical Fabry-Perot instrument profiles for HeCd and HeNe alignment lasers.

of light incident upon the mirrors. This is expressed as

$$RP = (2/\theta_{div})^2 \quad (4.14)$$

where θ_{div} is the full angle divergence of incident light. For transverse observations, 2 mm irises before and after the Fabry-Perot cavity and separated by ~ 75 cm limited θ_{div} to < 2.7 mrad. Thus, RP for blue spectrum lines was divergence - limited to $\sim 5.6 \times 10^5$ while RP for red lines was reflectivity - limited. For axial observation, light divergence was limited to ~ 1 mrad by the anode tube and a 1 mm iris prior to the Fabry-Perot.

Interferograms of both HeCd and HeNe laser alignment sources are shown in Fig. 4.9. In most cases, instrument broadening had negligible influence on observed spectral linewidths.

4.4.2 Experimental Results

Interferograms of some Ar II lines observed transverse to the arc axis are contained in Fig. 4.10. A polaroid plate was included in the optical path to block the Zeeman σ components. Some Ar II lines viewed along the arc axis showing the σ components are included in Fig. 4.11. Fabry-Perot scan time was ~ 30 sec/FSR. A 10 Hz low pass filter was used to integrate photon noise.

The contribution of thermal Doppler broadening to Ar II linewidths measured in both transverse and axial directions corresponds to an ion temperature of 2 eV ($\pm 10\%$). From the splitting of lines it was found that $B = 2.5$ kG along the arc axis, which compares favorably

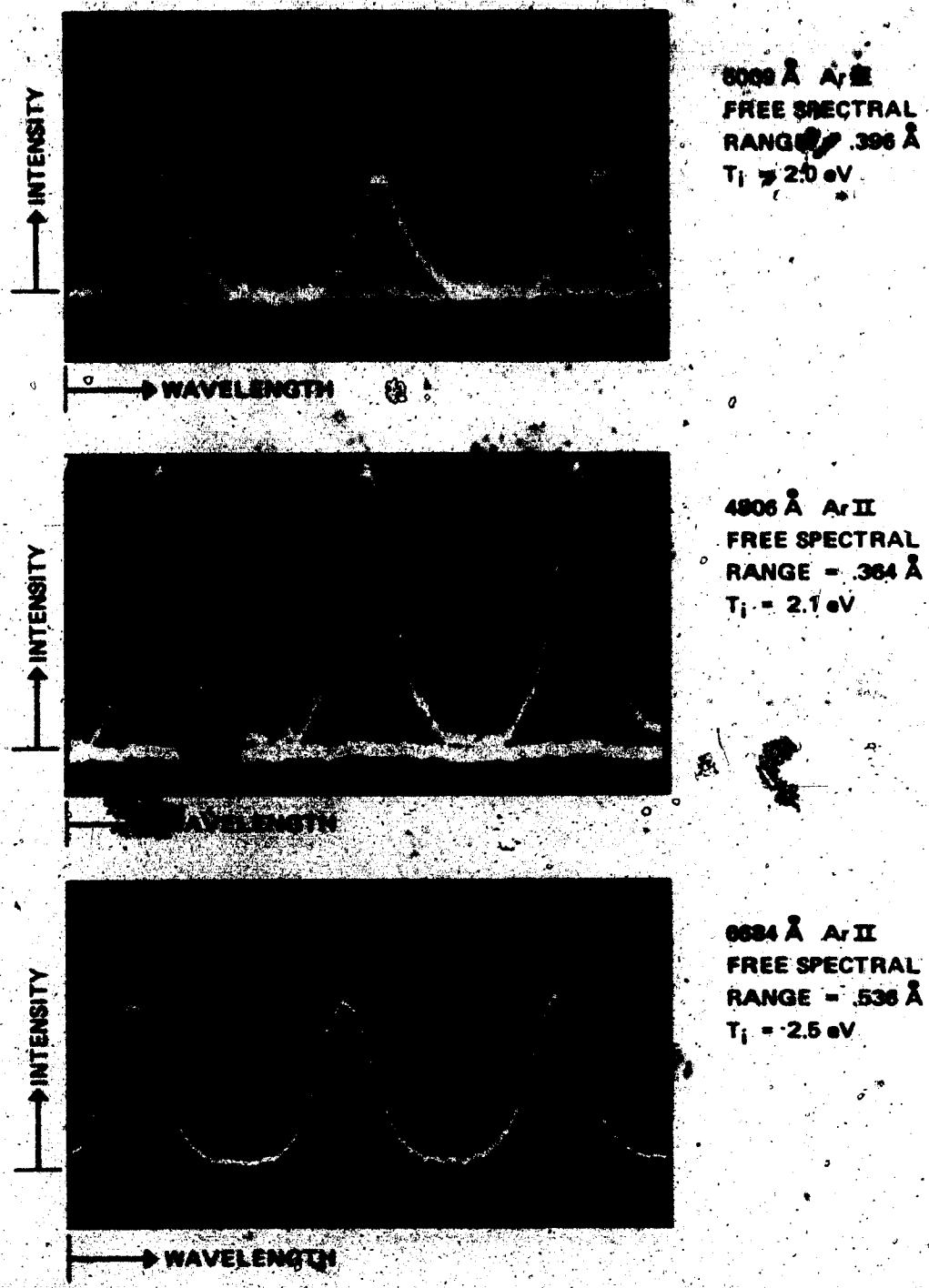
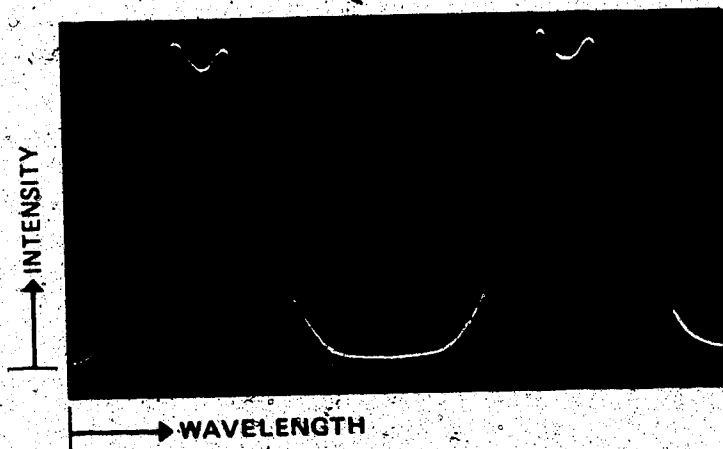
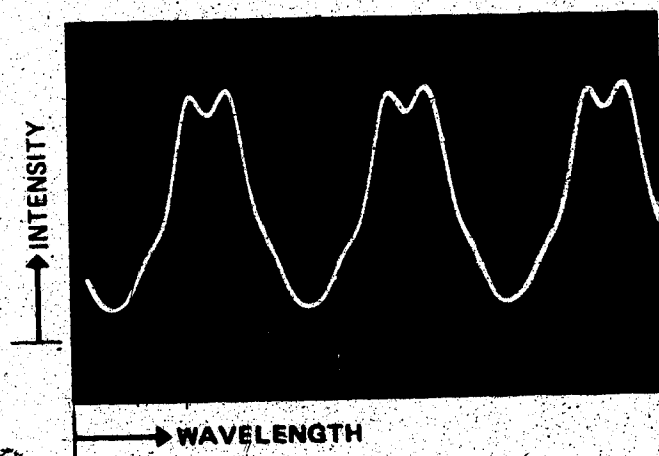


Fig. 4.10 π components of Doppler-broadened Ar II spectral lines viewed transverse to the arc axis. $P = 3$ Torr, $I = 270$ A, $V = 31$ V.



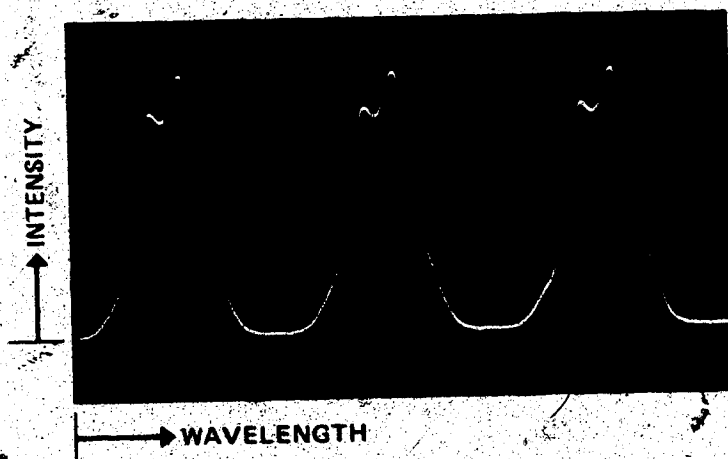
5062 Å Ar II
 FREE SPECTRAL
 RANGE = .554 Å

$T_i = 2.0 \text{ eV}$
 $B = 2.5 \text{ KGAUSS}$



4806 Å Ar II
 FREE SPECTRAL
 RANGE = .410 Å

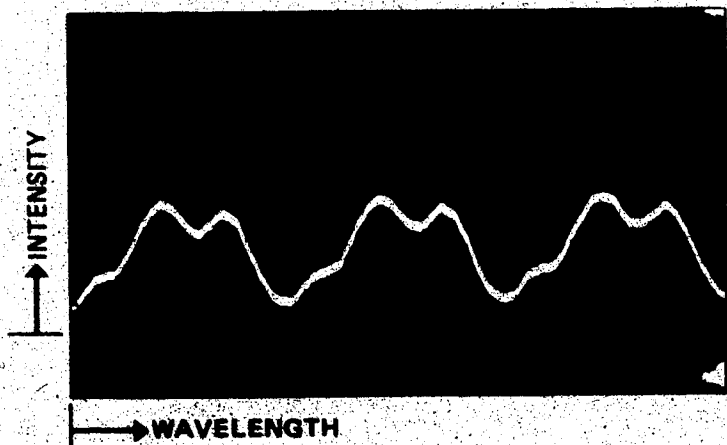
$T_i = 2.1 \text{ eV}$
 $B = 2.6 \text{ KGAUSS}$



4658 Å Ar II
 FREE SPECTRAL
 RANGE = .469 Å

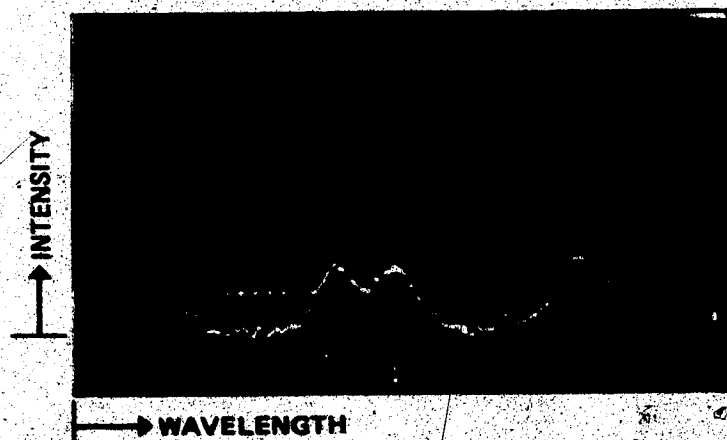
$T_i = 1.9 \text{ eV}$
 $B = 2.4 \text{ KGAUSS}$

Fig. 4.11 σ components of Doppler-broadened Ar II spectral lines viewed along the arc axis showing Zeeman splitting of transitions. $P = 3 \text{ Torr}$, $I = 270 \text{ A}$, $V = 31 \text{ V}$.



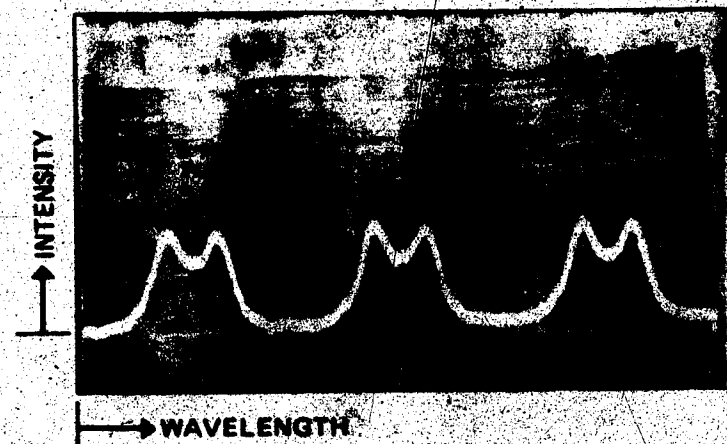
7380 Å Ar II
 FREE SPECTRAL
 RANGE = .789 Å
 B = 2.4 KGAUSS

a



6965 Å Ar I
 FREE SPECTRAL
 RANGE = .582 Å
 B = 2.1 KGAUSS

b



6965 Å Ar I
 FREE SPECTRAL
 RANGE = .702 Å
 B = 2.6 KGAUSS

c

Fig. 4.12 Zeeman splitting of Ar I and Ar II transitions; (a) components of 7380 Å viewed along the arc axis; (b) components of 6965 Å viewed transverse to the arc axis; (c), along the arc axis.

with the Hall probe measurements of field strength (see Chapter III). Profiles of the 6965 Å Ar I transition (Fig. 4.12) showed that neutrals existed in regions of lower field strengths away from the axis while axially they appeared to be in close proximity to the electrodes ($B = 2.6$ kG).

4.4.3 Discussion

Instrumental, Stark and Zeeman effects have all been taken into account in determination of the Doppler contribution to line broadening. Broadening due to the non-Doppler mechanisms was found to be essentially negligible in nearly all cases, with the result that the Doppler contribution itself could be determined to within 10% accuracy. Stark broadening parameters were taken from Griem⁵ using electron densities found from probe measurements. Unfolding of line shapes was accomplished in part by use of the Voigt profiles⁶, which result from the combination of dispersion and thermal broadening effects. In almost all cases, Stark broadening of Ar II lines for $n_e = 2 \times 10^{15} \text{ cm}^{-3}$ is much less than that due to thermal effects. If ion temperatures were significantly lower than 2 eV, n_e would have to be at least an order of magnitude greater to explain the observed broadening in terms of both Stark and Doppler effects. For example, the $\lambda = 4806$ Å Ar II line has $\Delta \lambda_D \approx 0.083$ Å for $T_i = 2$ eV and $\Delta \lambda_{\text{Stark}} \approx 0.003$ Å for $n_e = 2 \times 10^{15} \text{ cm}^{-3}$ and $T_e = 3.5$ eV. For $T_i = 1.4$ eV, $\Delta \lambda_D \approx 0.069$ Å and a Stark width of 0.03 Å is required for 0.083 Å total broadening, corresponding to an electron density of at least $2 \times 10^{16} \text{ cm}^{-3}$. As line profiles have been found to be very close to Gaussian in shape with the exception of the far wings, $T_i = 2$ eV is considered a reliable figure.

For pressures in the 1.5 to 6 Torr range and currents greater than 250 A, Ar II broadening was constant within 10%. Since T_i averaged over the arc cross-section is comparable to the on-axis temperatures, the T_i profile across the arc is unlikely to be highly peaked on axis, and therefore rather constant in the current channel.

Ar I lines such as 6965 Å have more pronounced Stark broadening than most Ar II lines. However, the measured relative width of the Ar I 6965 Å line was about half that of Ar II lines, more evidence that neutrals observed on axis are primarily in the electrode regions where large temperature gradients exist. In the current channel between anode and cathode it is likely that ionization is almost complete. Jassby⁷ estimates 98% ionization in the core of an argon arc with $I = 400$ A, $P = 3$ Torr, $T_i = 1.4$ eV and $B = 5$ kG.

4.5 Hydrogen Impurity in the Arc

A small percentage of hydrogen was present in the arc chamber under normal operating conditions. This was ascertained by identification of the H_{α} line (6563 Å) through Fabry-Perot line broadening measurements. No other Balmer lines were found, likely because their relatively weak intensities were swamped by argon line and continuum radiation.

Introduction of small partial pressures of hydrogen while monitoring H_{α} intensity showed that the intrinsic impurity level was typically $< 1\%$. It is likely that hydrogen trapped in the tungsten cathode constituted the major impurity source. The bottled argon gas contained only 5 ppm H_2 .

An interferogram of the impurity H_{α} line is shown in Fig. 4.13, as observed along the arc axis. Measured total width (FWHM) is ~ 1.1 Å.

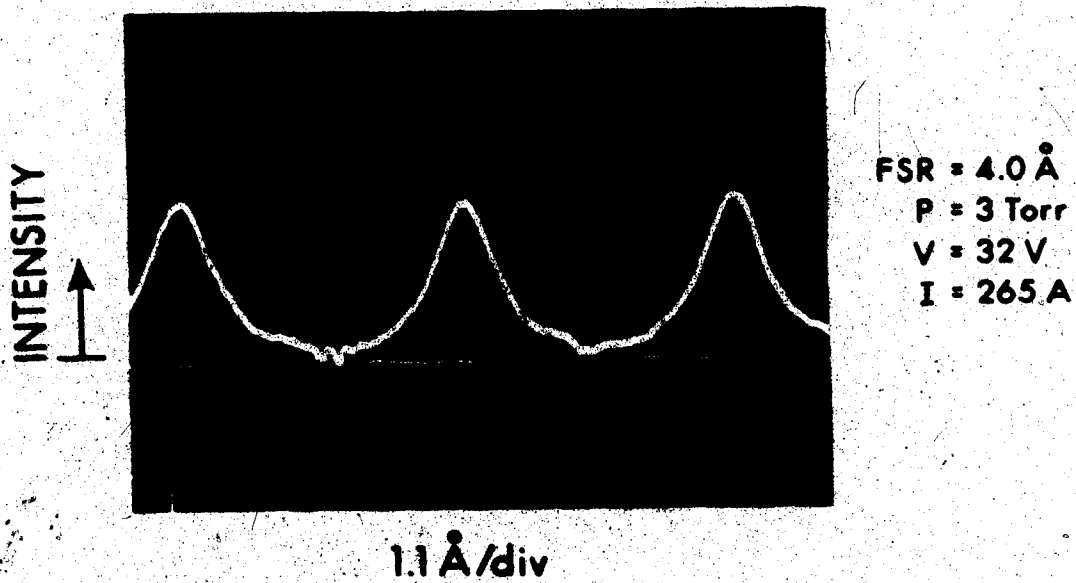


Fig. 4.13 Broadening of the H_{α} line, viewed along the arc axis.

The instrument width is 0.2 Å. Broadening is due to a combination of H_α fine structure, Zeeman, Stark and Doppler effects. From eqn. 4.9, the Doppler contribution is $0.5 T_H \text{ Å}$, for T_H in eV, which is 0.71 Å for $T_H = T_i = 2 \text{ eV}$. Whether or not T_H indeed equals T_i is uncertain. H_α fine structure and Zeeman splitting ($B = 2.5 \text{ kG}$) increase the width to 0.75 Å. Extrapolation of Griem's calculated H_α Stark broadening data⁵ yields $\Delta \lambda_{\text{Stark}} = 0.14 \text{ Å}$ for $n_e = 2 \times 10^{15} \text{ cm}^{-3}$ and $T_e = 3.5 \text{ eV}$. Assuming Lorentzian Stark and instrumental line shapes, a total Voigt width of $\sim 0.95 \text{ Å}$ results, which is within 15% of the measured width.

As several factors influence the broadening of the H_α line, including the exact location of the emitters, it is very difficult to draw any firm conclusions regarding temperatures and densities from measured H_α profiles. For transverse observation, measured H_α width was $\sim 0.8 \text{ Å}$; however, emission is from regions having a wide range of temperatures and densities.

Some further observations were made concerning the effect of hydrogen upon arc characteristics. With the arc operating in its high voltage mode (Fig. 3.4), addition of 1% H₂ invariably caused an immediate switch to the low voltage mode of operation. If operating in the low voltage mode, addition of 1% H₂ resulted in a slight arc voltage decrease and current increase (typically $\sim 3\%$ changes).

4.6 Conclusions

On the basis of the probe results, Doppler broadening measurements and consideration of energy equipartition times, it is plausible

that electron and ion temperatures are different, the electrons being the hotter species. The equipartition time¹¹ may be written as

$$t_{eq} \approx \frac{3 m_i m_e k^{3/2}}{8(2\pi)^{1/2} n_e Z^2 e^4 \ln \Lambda} \left(\frac{T_i}{m_i} + \frac{T_e}{m_e} \right)^{3/2} \quad (4.15)$$

With singly ionized argon ions, this reduces to

$$t_{eq} \approx \frac{1.3 \times 10^{10}}{n_e \ln \Lambda} \left(\frac{T_i}{7.3 \times 10^4} + T_e \right)^{3/2} \text{ sec} \quad (4.16)$$

for T_i, T_e in eV and n_e in cm^{-3} . For $n_e = 2 \times 10^{15} \text{ cm}^{-3}$, $T_i = 2 \text{ eV}$ and $T_e = 3.5 \text{ eV}$, $t_{eq} \approx 6 \text{ } \mu\text{sec}$, which is comparable to the ion lifetime, determined largely by charge transfer collisions with neutrals. Taking $n_0 = 4 \times 10^{13} \text{ cm}^{-3}$ in the core of the arc ($\sim 98\%$ ionization), $\tau = (n_0 \sigma v_i)^{-1} \approx 15 \text{ } \mu\text{sec}$, σ being the charge-transfer cross-section¹². This figure is likely an upperbound on the ion lifetime. For comparison, a recombination time ($1/\beta_r n_e$) estimate for this plasma is $\sim 5 \text{ msec}$, where β_r is the recombination coefficient for argon¹³. Thus, it is unlikely that ions are able to thermalize with respect to the electrons in the time available to them.

The values of n_e, T_e and T_i determined from probe and spectroscopic diagnostics result in a maximum plasma pressure of 15 - 20 Torr on axis. This compares with the magnetic pressure ($B^2/8\pi$) of $\sim 35 \text{ Torr}$ for $B = 2.5 \text{ kG}$. That this field is just sufficient to confine the arc has been observed (Chapter III); the calculated magnetic to plasma pressure ratio is indicative of this situation.

CHAPTER V

ARC PLASMA PERTURBATION BY A HIGH POWER CO₂ LASER5.1 Outline

An investigation was carried out to determine the possibility of arc plasma perturbations by the high power CO₂ lasers to be used in Thomson scattering experiments. In particular, electron heating in the focal volume via inverse bremsstrahlung absorption was studied. A simple model was adopted which assumed electron thermal conduction to be the dominant dissipative process. Numerical calculations based on this model showed negligible T_e increases for the laser intensities used for scattering. Experimental observations of Ar II line emission supported this conclusion.

5.2 Thermal Conduction Limited Electron Heating

Inverse bremsstrahlung absorption of radiation by plasma is a much more efficient process at 10 μm than for visible wavelengths, the absorption coefficient having a λ^2 dependence. One of the concerns then, when using a high power infrared source for scattering is the possible perturbation of the plasma and consequent distortion of scattered information.

Since the laser pulse times of 100 - 200 nsec are very much shorter than electron-ion equipartition times (eqn. 4.18), absorbed photons would lead to electron heating only during the observation time for scattering. As the arc is almost fully ionized in the

neighborhood of its axis, there is little opportunity for laser induced ionization. Even if this process did occur, density perturbations would be a few percent at most and therefore of small concern for the scattering experiment. In fact, the dominant electron energy loss is provided by thermal conduction which severely limits the elevation in T_e and therefore any ionization and collisional transfer of energy to ions.

A crude estimate of the electron heating may be obtained by equating power absorbed to the rate of change of the kinetic energy of free electrons in the laser focus.

$$\frac{\alpha(n_e, T_e, \lambda) P_0(t)}{A} = \frac{d}{dt} \left(\frac{3}{2} n_e k T_e \right) \quad (5.1)$$

$P_0(t)$ is the laser power and $A = \pi L^2$ is the focal area. The absorption coefficient α is given by¹

$$\alpha = \frac{(8\pi)^{3/2} n_e^2 e^6 \left(\frac{\bar{G}_\pi}{\sqrt{3}} \right) \left(1 - \frac{\omega_{pe}^2}{\omega_0^2} \right)}{3 c \omega_0^2 (m_e k T_e)^{3/2}} \quad (5.2)$$

For the existing plasma conditions, $\omega_{pe} \ll \omega_0 = \omega_{CO_2}$; thus $\bar{G}_\pi/\sqrt{3} = \ln \Lambda$ is given by¹ $\ln (3.9 \times 10^{14} T_e^{3/2}/\omega_0)$ for T_e in eV and

$$\alpha = \frac{10^{-35} n_e^2 \ln \Lambda}{T_e^{3/2}} \text{ cm}^{-1} \quad (5.3)$$

for T_e in eV, n_e in cm^{-3} .

Integration of eqn. 5.1 with respect to time for $n_e =$ constant leads to an electron temperature at the conclusion of the

laser pulse

$$T_{ef} = T_{eo} \left(1 + \frac{5 \times 10^{-35} n_e E_0 \lambda n \Lambda}{3 A_e T_{eo}^{5/2}} \right)^{2/5} \text{ eV} \quad (5.4)$$

where T_{eo} is the equilibrium electron temperature and E_0 is the laser energy. For $T_{eo} = 3.5$ eV, $n_e = 2 \times 10^{15} \text{ cm}^{-3}$, $E_0 = 3\text{J}$ and $\Lambda = 3 \times 10^{-2} \text{ cm}^2$, the result is $T_{ef} = 5.5$ eV, a considerable perturbation.

Of course this calculation provides for no thermal losses from the focal volume during the heating time. An important process to consider is electron thermal conduction, whereby heated electrons will diffuse into their cooler surroundings. The coefficient of electron thermal conduction is given by¹

$$\kappa_e = \frac{310 T_e^{5/2}}{\lambda n \Lambda} \frac{\text{watts}}{\text{cm eV}} \quad (5.5)$$

for T_e in eV.

If, indeed, the temperature calculated from eqn. 5.4 was ever established, the thermal conduction loss rate

$$V \cdot \kappa_e \nabla T_e = \kappa_e V^2 T_e \frac{\text{watts}}{\text{cm}^3} \quad (5.6)$$

would be of the order of 10^6 watts/cm³ so that absorbed laser energy could be dissipated in a few nsec. Since this is 2 orders of magnitude faster than the laser heating time, the real temperature rise is likely ~ 2 orders of magnitude less than that calculated assuming no losses.

It is therefore assumed that a steady state is quickly

reached in which absorption is balanced by thermal conduction.

$$\frac{10^{-35} n_e^2 \omega n \Lambda P_0(t)}{A T_e^{3/2}} + \kappa_e v^2 T_e = 0 \quad (5.7)$$

Because of the axial magnetic field, cross field conduction losses will be less than that along field lines by a factor $(r_{Be}/\lambda_{e-e})^2 \approx 10$.

Therefore, a one dimensional model is used to describe thermal diffusion losses (see Fig. 5.1) so that

$$v^2 T_e \approx \frac{d^2}{dz^2} T_e \quad (5.8)$$

With this approximation, eqn. 5.7 may be rearranged to read

$$\frac{d^2 T_e}{dz^2} = - \frac{\beta}{T_e^4} \quad (5.9)$$

where

$$\beta = \frac{3.2 \times 10^{-38} (n_e \omega n \Lambda)^2 P_0(t)}{A} \quad (5.10)$$

Note that for small temperature changes, κ_e is constant in z which has been implicitly assumed in writing eqn. 5.6.

One integration of eqn. 5.9 yields

$$\frac{dT_e}{dz} = - \left(\frac{2\beta}{3 T_e^3} + \text{constant} \right)^{1/2} \quad (5.11)$$

The boundary conditions are

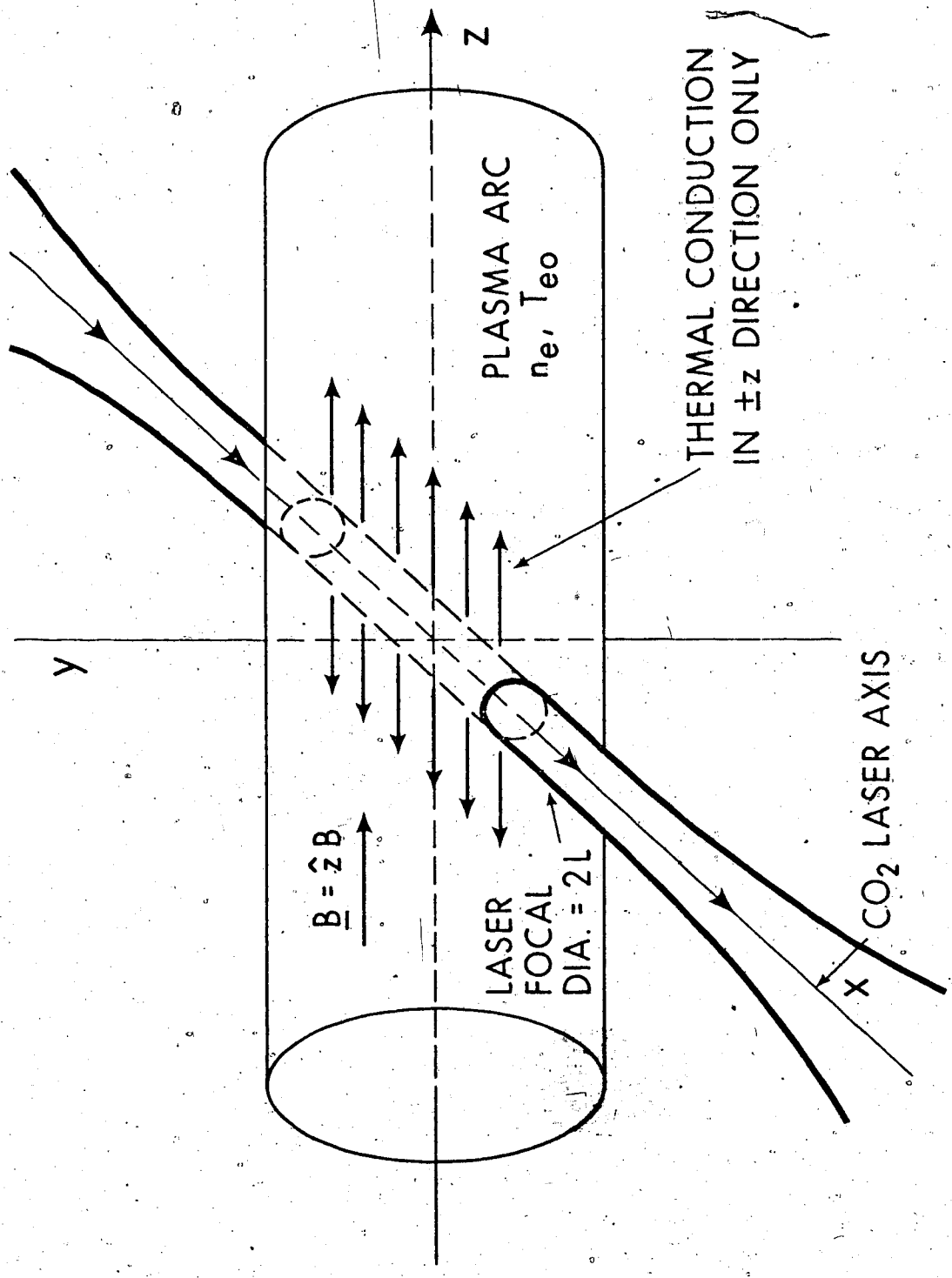


Fig. 5.1 Model for plasma electron heating, in the CO₂ laser focal volume.

$$\left. \frac{dT_e}{dz} \right|_{z=0} = 0 \quad (5.12)$$

and

$$T_e(L) + \lambda_{e-e} \left. \frac{dT_e}{dz} \right|_{z=L} = T_{e0} \quad (5.13)$$

where T_{e0} is the unperturbed temperature. In adopting boundary condition 5.13, it is assumed that outside the heating zone, T_e will decrease to the equilibrium value T_{e0} over a characteristic scale length for thermal conduction. The electron mean free path, λ_{e-e} , is taken as this scale length. For $|z| \geq L$, the solution is then

$$T_e(z) = T_{e0} + (T_e(L) - T_{e0}) e^{-(z-L)/\lambda_{e-e}} \quad (5.14)$$

Using boundary condition 5.12, eqn. 5.11 becomes

$$\frac{dT_e}{dz} = - \left(\frac{2\beta}{3} \right)^{1/2} \left(\frac{1}{T_e^3} - \frac{1}{T_e^3(0)} \right)^{1/2} \quad (5.15)$$

where $T_e(0)$ is the maximum temperature attained on the laser axis.

Expansion of $T_e(z)$ in a Taylor series about $z = 0$ results, for $T_e(0) - T_{e0} \ll T_{e0}$, in an approximate solution for $|z| \leq L$

$$T_e(z) = T_e(L) + \frac{\beta L^2}{2 T_e^4(0)} \left(1 - \frac{z^2}{L^2} \right) \quad (5.16)$$

Numerical solutions of eqns. 5.14 and 5.16 have been carried out and the results checked by numerical integration of eqn. 5.15. Temperatures and density ($2 \times 10^{15} \text{ cm}^{-3}$) near to those of the actual

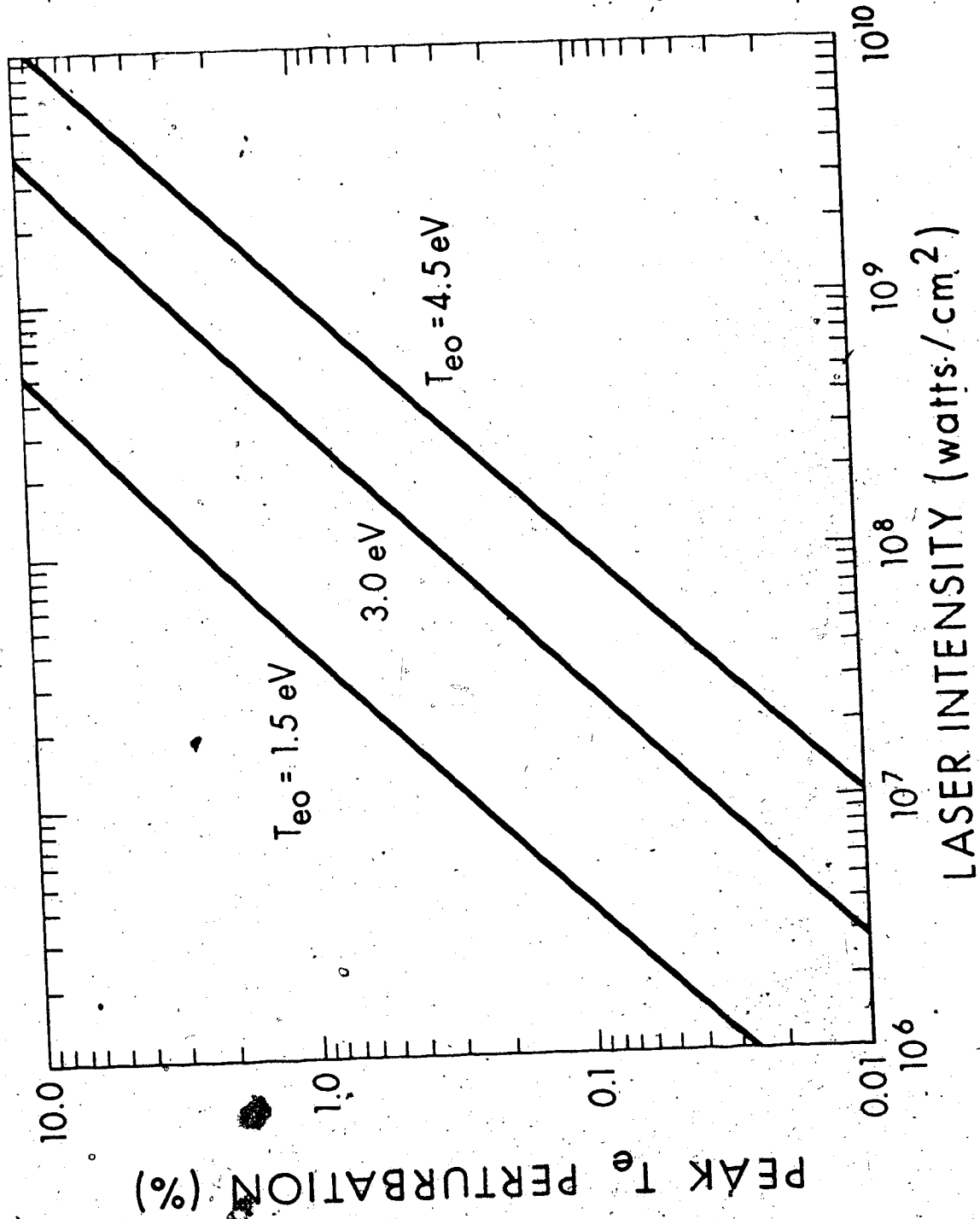


Fig. 5.2 Electron temperature perturbations as a function of CO₂ laser intensity.

argon arc parameters were considered and calculations for laser intensities up to 10^{10} watts/cm² were done.

Results are shown in Fig. 5.2. For intensities used in the present Thomson scattering experiments (up to 7×10^8 watts/cm²), the T_e perturbations are apparently negligible.

5.3 Experimental Observations and Discussion

Emission levels from Ar II transitions in the laser-plasma interaction volume were monitored in an attempt to verify that electron heating was indeed small. Light was collected by the Cassegrainian telescope and a 1/4 m Jarrell-Ash monochromator provided spectral dispersion (~ 10 Å resolution) prior to detection by a photomultiplier which was loaded sufficiently to observe events on the time scale of CO₂ laser pulses.

Ar II lines monitored included 4348 Å, 4590 Å, 4610 Å, 4658 Å and 4806 Å. For laser intensities of 5×10^7 watts/cm² and 3×10^8 watts/cm², there were no observable changes in the emission level from any of these transitions when the laser was fired. Typical signal to noise for these lines was (15-20)/1 so that $\sim 6\%$ changes in emission were detectable. The noise limit appeared to be determined by fluctuations in plasma arc conditions.

As the intensity I of emission from a given transition is proportional to e^{-E/kT_e} where E is the energy of the upper level of the transition, then changes in emission may be related to changes in T_e .

$$dI \propto \frac{E}{kT_e^2} e^{-E/kT_e} dT_e \quad (5.17)$$

or

$$\frac{dI}{I} = \frac{E}{kT_e} \frac{dT_e}{T_e} \quad (5.18)$$

For the Ar II lines mentioned, $E/k \approx 20$ eV so that $\Delta I/I \approx 5.7 \Delta T_e/T_e$ for $T_e = 3.5$ eV. As increases of $\sim 6\%$ in line emission were resolvable, it may be possible to conclude that increases in T_e are $< 1\%$.

In employing such an argument, it is assumed that the high energy bound electrons are in equilibrium with the free electrons. In the case of Ar II, this is reasonable as the energy difference between the bound levels and the continuum is small compared with the bound level energies themselves (~ 20 eV). Therefore, the Boltzmann factors for these levels are likely to be reasonably accurate.

A rough estimate of the relation between laser induced ionization and changes in T_e may be found from the Saha equations. In the case of $n_{\text{ArII}} \gg n_{\text{ArI}}, n_{\text{ArIII}}$ as is likely in the present argon arc, changes in neutral and doubly ionized densities are very sensitive to changes in T_e . Experimentally, however, insufficient Ar I and Ar III emission levels from the laser-plasma interaction volume were available to investigate this relationship and thereby aid in determining a limit

for electron heating.

With the experimental results for Ar II line excitation in terms of T_e increase supported by the thermal conduction model calculations, it is concluded that the arc temperatures and densities determined by probe and spectroscopic diagnostics are preserved under conditions of the Thomson scattering experiments.

CHAPTER-VI

COOPERATIVE THOMSON SCATTERING EXPERIMENTS

6.1 Outline

With known experimental values for temperatures, densities and fields in the plasma, and the availability of a 10 MW 10.6 μm pulsed CO_2 laser, the type of scattered spectra could be determined and steps taken to design an optical-electronic system for detection and resolution thereof.

In this Chapter, features of the expected cooperative scattered spectra for the argon arc plasma are discussed. Plasma chamber structural aspects along with optical detection components are described leading to design of a suitable viewing system for Thomson scattering. Characteristics of the infrared detector are noted, expected signal levels are calculated and the influence of various noise sources is determined. Observed signal and noise amplitudes are given and factors causing discrepancies from expected values are detailed. Thermal stabilization of the Fabry-Perot interferometer employed for spectral resolution is discussed. A method for signal to noise improvement in pulsed information is described.

Results of spectral scans are compared with calculated profiles which reflect the influence of the finite laser linewidth and the Fabry-Perot instrument function. Consideration is given to the applicability of this CO_2 scattering technique to Tokamak plasmas.

6.2 Scattered Spectral Shapes.

Spectral features of light scattered from the argon arc plasma using a CO₂ laser as incident source may be determined from a knowledge of the particle densities and temperatures as well as the magnetic field strength in the plasma. Taking $n_e = n_i = 2 \times 10^{15} \text{ cm}^{-3}$, $T_e = 3.5 \text{ eV}$ and $T_i = 2 \text{ eV}$, the scattering parameter α (eqn. 2.12) has a minimum value of 2.7 for $\theta = \pi$. Therefore, cooperative spectra would be observed for any scattering angle. The plasma chamber was designed with a viewing port at 30° to the laser axis through the arc; thus, either 30° forward scatter or 150° backscatter could be observed, for which $\alpha = 10.4$ and 2.8 respectively.

The bulk of the scattered power appears in the ion feature. In these spectra, the total width of which is approximately

$$\Delta\lambda = 2 \left(\frac{\lambda_0^2}{2\pi c} \right) (2 k_0 \bar{v}_i \sin \theta/2) \quad (6.1)$$

where \bar{v}_i is the mean ion thermal speed. This evaluates to 4.3 Å (FWHM) for $\theta = 150^\circ$ and 1.1 Å for $\theta = 30^\circ$.

The particular shape of the ion feature is described by the β parameter (eqn. 2.15) which equals 1.3 for $\theta = 30^\circ$ and 1.2 for $\theta = 150^\circ$ and the experimental conditions prevailing. Ion acoustic waves are strongly damped therefore, and the spectra will appear rather flat-topped in both cases.

Plasma frequency satellites appear in these cooperative spectra and are shifted from line centre an amount given by the dispersion relation for longitudinal oscillations in the plasma. In terms of fre-

quency, for $\alpha \gg 1$,

$$\Delta \omega = \pm \left(\omega_{pe}^2 + \frac{3k T_e k^2}{m_e} \right)^{1/2} \quad (6.2)$$
$$= \pm \omega_{pe} \left(1 + \frac{3}{\alpha^2} \right)^{1/2}$$

which becomes $1.2 \omega_{pe}$ for $\alpha = 2.8$ and $1.0 \omega_{pe}$ for $\alpha = 10.4$. For $n_e = 2 \times 10^{15} \text{ cm}^{-3}$, $\omega_{pe} \approx 2.5 \times 10^{12} \text{ sec}^{-1}$. The wavelength shifts are then $\pm 0.18 \mu\text{m}$ and $\pm 0.15 \mu\text{m}$ for $\theta = 150^\circ$ and $\theta = 30^\circ$ respectively.

The available infrared detector was equipped with an optical filter whose bandpass was limited to $0.14 \mu\text{m}$ (FWHM) centred at $10.6 \mu\text{m}$. Unfortunately, the small percentage of scattered power in each satellite ($< 5\%$ for $\theta = 150^\circ$) combined with low filter transmission at the wavelengths of interest rendered detection impossible.

The presence of a 2.5 kG axial magnetic field does not alter the shape of the ion feature in the scattered spectra. The ratio of an ion cyclotron frequency to a typical scattered frequency shift is of the order of 4×10^{-4} . Therefore \underline{k} must be within an angle $\sin^{-1}(4 \times 10^{-4}) = 0.02^\circ$ of the perpendicular to the direction of \underline{B} in order to observe ion cyclotron fine structure.

Since the detection optics were set up to collect light from an annulus defined by full angles of 11.6° and 3.3° , no magnetic modulations will appear in the ion spectral feature. Even if light with the appropriate \underline{k}_s vectors could be analysed, the modulations would have a characteristic wavelength separation of $< 10^{-3} \text{ \AA}$, so that no realistic resolving power would be available to observe them.

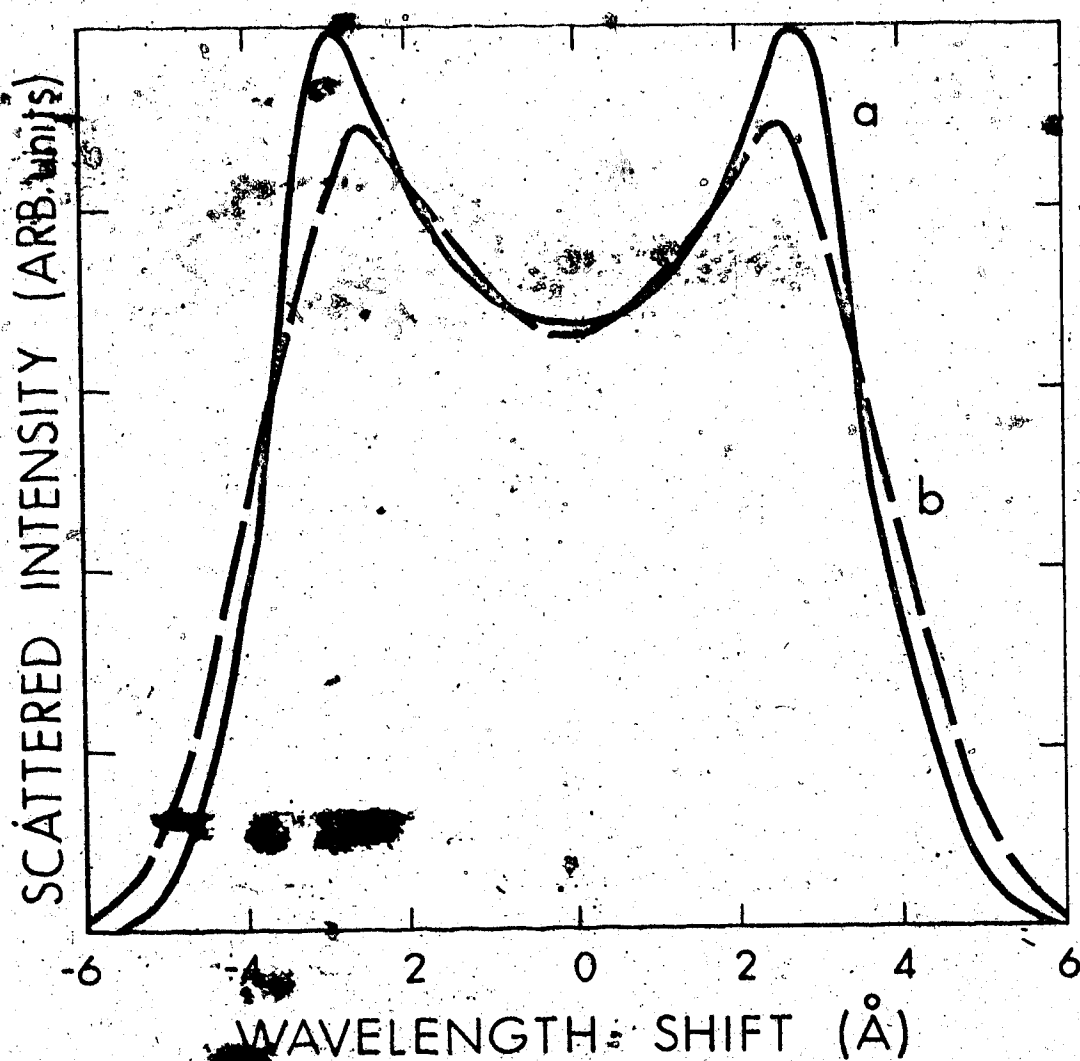


Fig. 6.1. Theoretical ion spectra for $\theta = 150^\circ$ backscatter.. (a) Salpeter spectrum $\Gamma^B(\lambda)$ for $\alpha = 2.8$ and $\beta = 1.2$, $\Delta\lambda = 7.3$ Å (FWHM); (b) normalized $I_{\text{BL}}(\lambda)$, the actual spectrum for a 1.2 Å Lorentzian laser line, $\Delta\lambda = 7.7$ Å (FWHM).

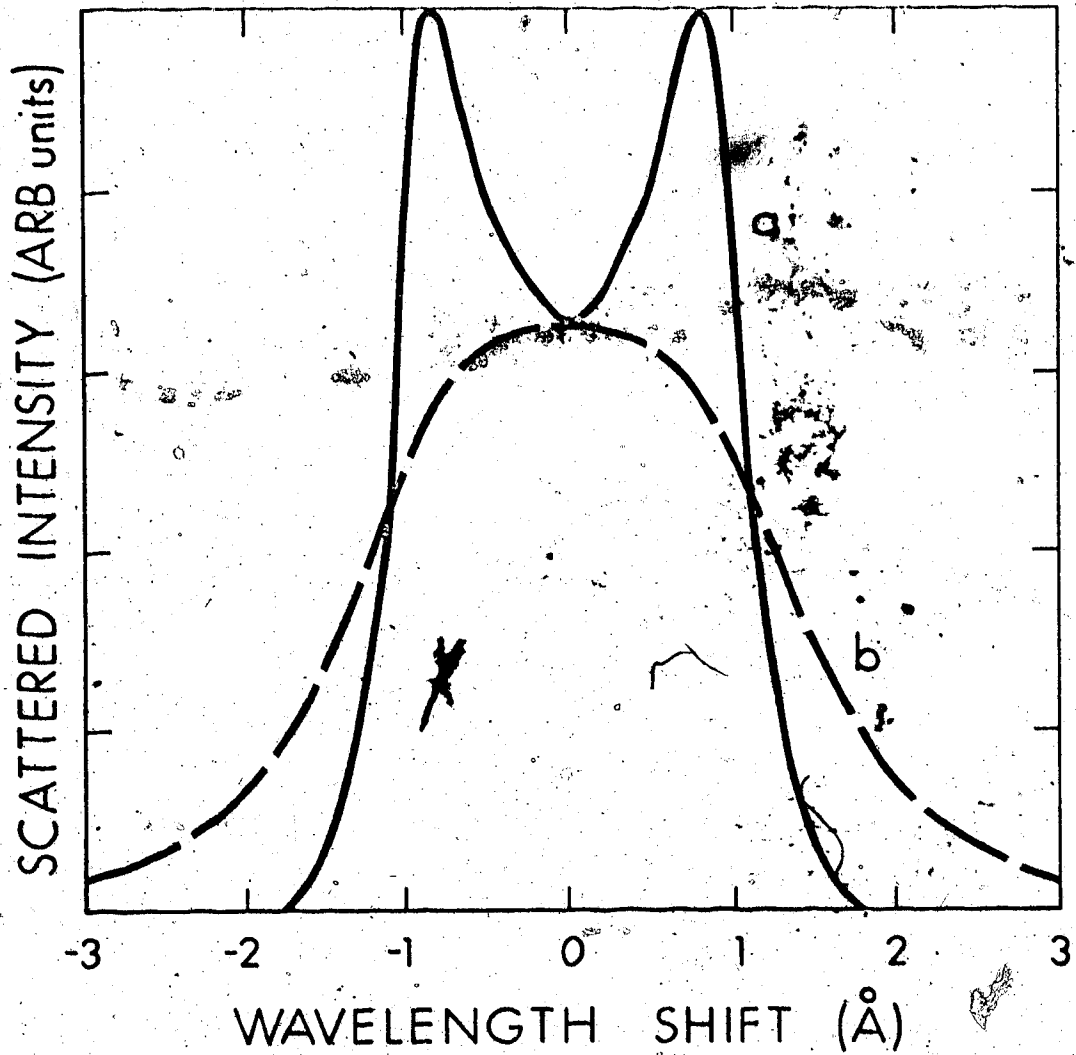


Fig. 6.2 Theoretical ion spectra for $\theta = 30^\circ$ forward scatter. (a) Salpeter spectrum $\Gamma_B(\lambda)$ for $\alpha = 10.4$ and $\beta = 1.3$, $\Delta\lambda \approx 2.2$ Å (FWHM); (b) normalized $I_{BL}(\lambda)$, the actual spectrum for a 1.2 Å Lorentzian laser line, $\Delta\lambda \approx 2.8$ Å (FWHM).

Collisional effects should not influence spectral shapes either. Characteristic mean free path for ion collisions with other ions is ~ 0.1 mm, (from eqn. 4.7, with $\lambda_{i-i} = \lambda_{e-e} T_i^2/T_e^2$) \gg than the CO₂ laser wavelength. From eqn. 2.20, $\alpha_{ci} = 9 \times 10^{-3}$ for $\theta = 150^\circ$ and $\sim 3 \times 10^{-2}$ for $\theta = 30^\circ$. Thus, no collisional narrowing of the ion feature should occur.

Salpeter's Γ_B functions (the collisionless, $B = 0$ case) adequately describe the ion spectra for the existing plasma conditions. In Figs. 6.1 and 6.2, the Γ_B 's are plotted for $\theta = 150^\circ$ and $\theta = 30^\circ$.

Pulsed CO₂ laser linewidths are not negligible compared to the widths of these ion spectra. The laser spectrum was therefore folded into the Γ_B profiles, the result given by

$$I_{BL}(\lambda) = K_1 \int_{-\infty}^{\infty} \Gamma_B(\lambda') I_L(\lambda - \lambda') d\lambda' \quad (6.3)$$

where K_1 is a normalization constant. Numerical evaluation of this convolution integral was carried out. $I_L(\lambda)$ was approximated by a Lorentzian profile of measured width (FWHM) 1.2 Å (see Fig. 3.6(b)). For the CO₂ source used, I_{BL} represents the actual scattered spectrum. Results are plotted in Figs. 6.1 and 6.2 along with the respective monochromatic source spectra. Note that the shape of the $\theta = 30^\circ$ spectrum is affected considerably more than that of the $\theta = 150^\circ$ spectrum.

6.3 Experimental Design

6.3.1 Input Optics

A complete schematic of the optical design for scattering

is shown in Fig. 6.3. Gold coated optics were used to couple the CO₂ laser beam into the plasma chamber which was provided with Brewster angle NaCl windows for beam entry and exit. A 50 cm focal length gold coated mirror focussed the radiation on arc axis; measured focal spot size was 2 mm for the amplified beam and 1.7 mm for the 6.7 m oscillator output.

Input path alignment was done with a He Ne laser which passed through the CO₂ cavity and 2 subsequent irises prior to focussing on a 1.75 mm diameter stainless steel ball which simulated the scattering volume. High stability CO₂ laser mirror mounts ensured that discharge shock waves did not misalign the cavity in the long term.

6.3.2 - Collection Optics

A NaCl window mounted at 30° to the laser axis afforded a view of the scattering plasma volume. Light collection and collimation was accomplished with a Cassegrainian telescope (see Chapter IV). The effective collecting diameter of the 20 cm radius of curvature mirror was 10 cm when placed 50 cm from the laser-plasma intersection. Light collimated by the 2.5 cm diameter, 3.25 cm focal length concave mirror was eventually focussed onto the infrared detector by a 6.5 cm focal length NaCl lens.

Magnification of the Cassegrainian system is given by

$$M = \frac{R}{2\sigma - R} \frac{f_2}{f_1} \quad (6.4)$$

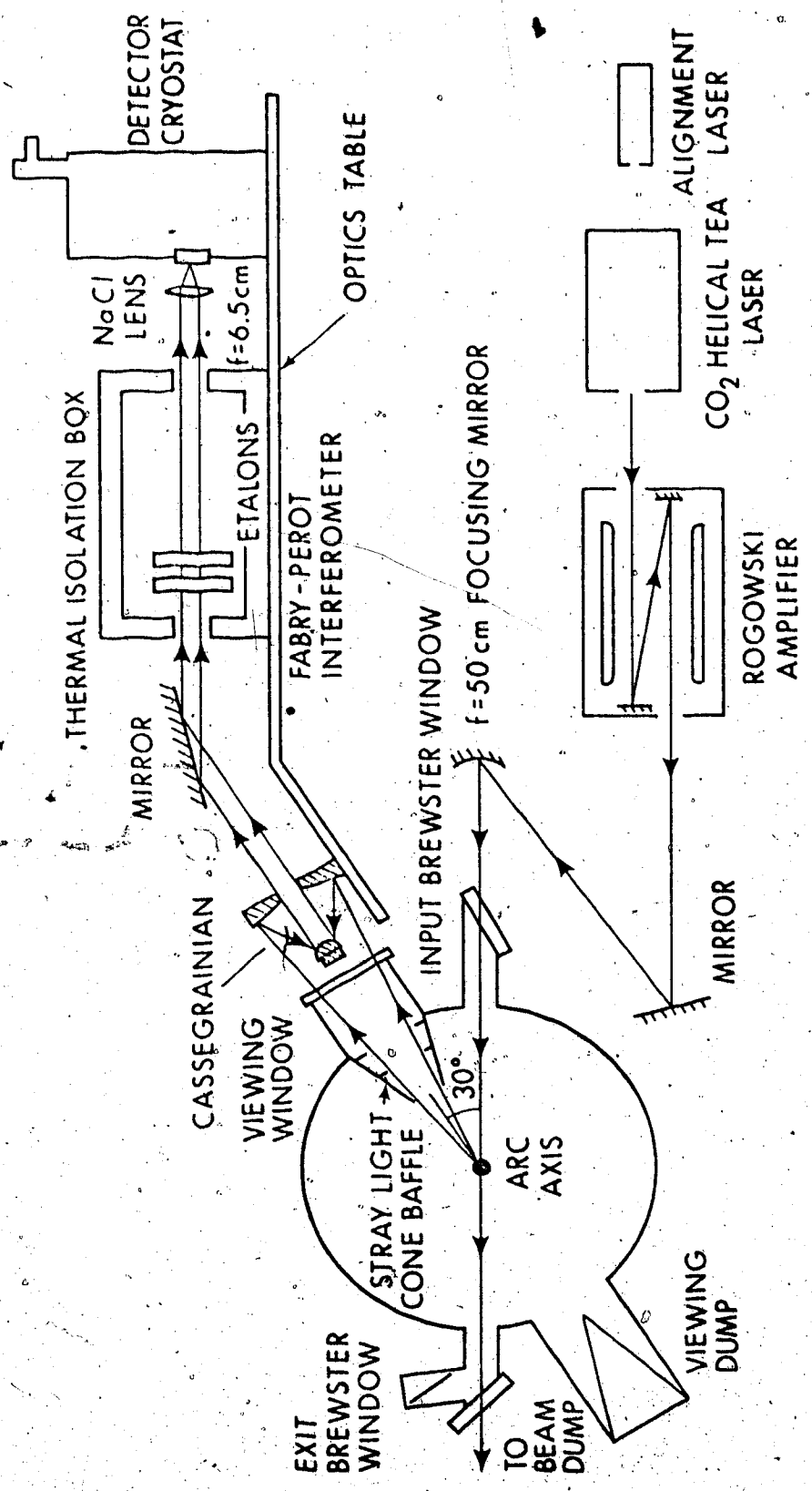


Fig. 6.3 Input and detection optics for Thomson scattering. For $\theta = 30^\circ$ forward scattering, input beam direction and Brewster window attachments are reversed.

where σ is the distance from the scattering centre to the collecting mirror, R is the radius of curvature of this mirror, f_1 the focal length of the collimating mirror and f_2 that of the NaCl lens. In this case, $M = 0.5$. Given a detector chip of area $1 \text{ mm} \times 2 \text{ mm}$, a laser plasma interaction width of 2 mm and a length of $4 \text{ mm} / \sin 30^\circ = 8 \text{ mm}$ could be viewed.

The Cassegrainian collected light with scattering angles $30^\circ \pm 5.8^\circ$, thus providing sufficient resolution for the α parameter. For $\theta = 150^\circ$, α would remain constant to within $\pm 1.5\%$; for $\theta = 30^\circ$, the range of α would be from 8.7 to 12.9, a $\pm 20\%$ variation. The solid angle subtended by the collecting mirror was

$$\Delta \Omega = \frac{A_1 - A_2}{\sigma^2} = \frac{\pi(5^2 - 1.6^2) \text{ cm}^2}{50^2 \text{ cm}^2} = 2.8 \times 10^{-2} \text{ sterr} \quad (6.5)$$

Here, A_1 is the area of the collecting mirror and A_2 the area of the collimating mirror shadow upon it.

From eqn. 2.16, the detectable scattered power, integrated over all wavelengths is, for $r_e^2 = 8 \times 10^{-26} \text{ cm}^2$, $n_e = 2 \times 10^{15} \text{ cm}^{-3}$, $\lambda = 0.8 \text{ cm}$, $\Delta \Omega = 2.8 \times 10^{-2} \text{ sterr}$, $P_0 = 10^7 \text{ watts}$ and $\sin^2 \delta = 0.9$,

$$P_s = 1.6 \times 10^{-5} T_0 \text{ watts} \quad (6.6)$$

where T_0 is the transmission of the collection optical train. This included a NaCl viewing window, 3 gold-coated surfaces and a NaCl lens. Therefore $T_0 = (0.92) (0.99)^3 (0.92) = 0.8$ and $P_s = 1.3 \times 10^{-5} \text{ watts}$.

6.3.3 Stray Laser Light

Since 10 MW laser powers were being utilized, several measures were taken to ensure that stray laser light did not enter the optical system and swamp the scattered power levels. Plasma chamber walls were painted black to aid in the absorption of stray CO₂ light. The exit Cassegrainian window was equipped with a dump to trap NaCl surface reflections of the laser. A conical viewing dump was provided opposite the NaCl viewing window. It was designed such that light incident upon its blackened walls suffered many reflections and considerable absorption before exiting. A blackened cone with optical baffles was installed so as to prevent light from any line of sight other than that directly through the scattering volume from reaching the Cassegrainian. External to the chamber, the laser beam was dumped against a blackened inclined wall a distance of 50 cm from the exit window.

6.3.4 Fabry-Perot Interferometer Resolution

Laser input and scattering detection optics were mounted on an aluminum table isolated from the plasma chamber and associated vibrations due to vacuum pumps, etc. Isolation was important, especially for the Fabry-Perot interferometer - the instrument which provided the necessary spectral resolution. Given that ion spectra were likely of the order of a few Å in width, resolving powers $\lambda/\Delta\lambda$ in the neighborhood of 10^5 were required.

At our disposal was a Lansing model interferometer, with 2 flat germanium etalons 5 cm in diameter and coated for 99% reflectivity

in the 10 μm region. These etalons were mounted and the interferometer operated in the manner described in Chapter 4.

In particular, 2 \AA resolution was desired for analysis of $\theta = 150^\circ$ backscatter and 1 \AA resolution for the narrower $\theta = 30^\circ$ forward scattered spectrum. Light from a low power (~ 1 watt) CW CO_2 laser was focussed on the stainless steel ball and scattered into the Cassegrainian for purposes of interferometer alignment. For a reflectivity R of 99%, a finesse of 310 was possible, but only for perfectly collimated light, which was not available. In fact, the Cassegrainian was aligned such that mean full angle divergence of He Ne laser light scattered from the steel ball was 9 mrad. The free spectral range (FSR) of the instrument, $\lambda^2/2d$, for backscattering with etalon separation $d = 0.23$ cm was 245 \AA . A finesse of 120 was obtained, implying 2 \AA (FWHM) resolution. For forward scattering, $d = 0.52$ cm was used and finesse of 108 obtained for 1 \AA resolution. Linewidth of the alignment laser contributed negligibly to these values. Maximum transmission achieved for 2 \AA resolution was 12% and 10% for 1 \AA resolution. In Fig. 6.4, an oscillogram of a typical point source resonance function is shown.

Profiles were obtained by applying the detector signal to the input of a P.A.R.L. lock-in amplifier. Reference voltage was supplied by a photo-transistor which detected visible light chopped by the laser beam chopper wheel. The d.c. output of the lock-in was displayed on a Tektronix 556 oscilloscope, which was swept externally by a voltage proportional to the Fabry-Perot scanning ramp.

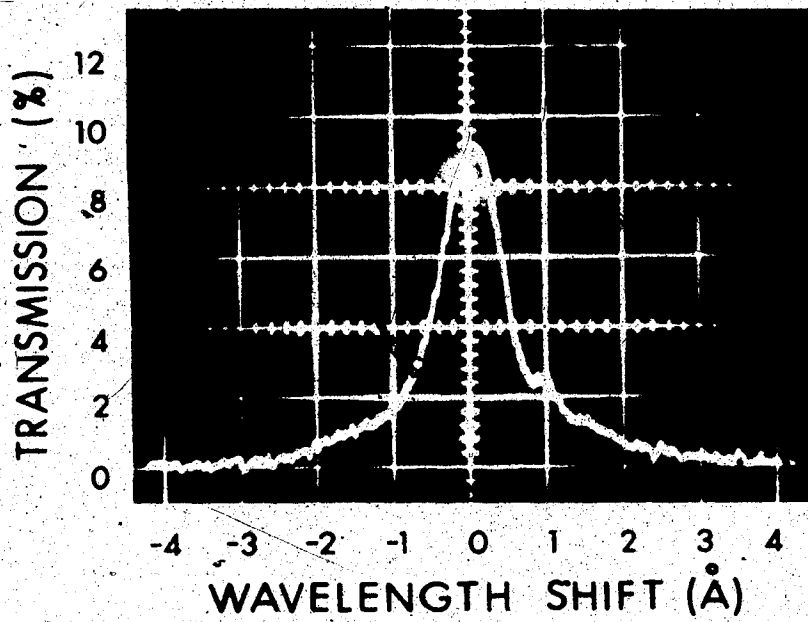


Fig. 6.4 Point source instrument profile for the Fabry-Perot interferometer showing 1 Å width used for resolution of $\theta = 30^\circ$ forward scatter.

6.3.5 Fabry-Perot Thermal Stabilization

Because of the high interferometer resolution required, serious problems arose with regard to long term maintenance of optimum finesse and transmission. It was discovered in the course of investigations that the resonance position would drift substantially (many widths) and the resolution deteriorate (to $> 2.(\Delta\lambda)_0$), typically over a period of a half hour. Since precautions had been taken to isolate against mechanical vibrations, thermal effects were suspected and indeed found to be the source of trouble.

The interferometer body was constructed of aluminum which has a thermal expansion coefficient of $2.5 \times 10^{-5}/^{\circ}\text{C}$. With the etalon mounts separated by a few cm, a 1°C change in temperature could mean a change in etalon separation of the order of a micron, which is 20% of a FSR.

In addition, the piezoelectric crystal stack had a temperature coefficient of $10^{-6}/^{\circ}\text{C}$ and a length of 3 cm, for a change in length of $0.03 \mu\text{m}/^{\circ}\text{C}$. Accurate quartz crystal thermometers mounted adjacent to the Fabry-Perot cavity showed typical fluctuations of $\pm 0.5^{\circ}\text{C}$ over half hour periods.

To alleviate this problem, the interferometer was enclosed in a plywood box insulated on the interior by 5 cm thick styrofoam everywhere except for 2.5 cm diameter light entry and exit apertures. Once sealed from exterior air currents, the box and contents reached thermal equilibrium in about 1 hr, after which temperature fluctuations were limited to $< 10^{-2} ^{\circ}\text{C}/\text{hr}$. Therefore, the box served as a rather effective thermal integrator, and a corresponding improvement in instrument stability was observed.

39

As an additional precaution against any drifts during the course of spectral scans, a reference path was included in the optics. By means of a removable mirror which intersected light from the Cassegrainian, the resonance position could be periodically checked during experimental runs.

6.3.6 Infrared Detector

For all scattering measurements, the IR detector used was a mercury doped germanium (GeHg) photoconductive device. Detectors of this type are sensitive to the near IR with a long wavelength cut-off at $\sim 14 \mu\text{m}$. They must be cooled to $< 30^\circ\text{K}$ and therefore liquid helium was used as the refrigerant. As previously mentioned, a cooled narrow-band filter was included immediately before the 1 mm x 2 mm detector.

IR detectors are, of course, sensitive to heat radiated by the surrounding environment. The filter is necessary to limit the optical bandwidth of this background radiation and the photon noise associated with it, while maintaining transmission at the wavelengths of interest. Detector sensitivity is increased as a direct consequence of background noise reduction. With filter, this detector had a responsivity of 2×10^7 volts/watt at $10.6 \mu\text{m}$ when a 15 V bias battery in series with a $2 \text{ M}\Omega$ resistor was connected across the chip. Detector rise time was ~ 100 nsec with proper loading, about equal to the laser pulse rise time. Measured detector resistance was $\sim 3 \text{ M}\Omega$.

6.4 Signal/Noise Calculations

Given the expected scattered power level and the detector responsivity, the integrated scattered signal may be calculated. Experimentally, it was convenient to work with a 180 kΩ bias resistor and 15 V bias battery. With detector output capacitively coupled to a Tektronix 1A7A preamplifier, ($R_{in} = 1 M\Omega$) the net load was 150 kΩ. Under these conditions, detector response to pulsed CO₂ radiation was 1.2×10^4 volts/watt. Risetime of the loaded detector plus preamplifier was 5 μsec, and the signal decay time was ~ 40 μsec. For the scattered power found from eqn. 2.16, integrated scattered signals would be 158 mV. For 6% average Fabry-Perot transmission over a 2 Å bandpass in a 7 Å wide spectrum, a typical resolved signal would be 2.7 mV. Against this signal level, the amplitude of noise voltage due to various sources was then considered.

Three possible origins of noise which could hamper recovery of plasma scattered signals were evaluated; these noise sources are all random in nature. Plasma bremsstrahlung radiation is considered first. For a volume V of plasma, the bremsstrahlung emitted per unit wavelength per unit solid angle is¹

$$P_b = 2.1 \times 10^{-36} g Z^2 \frac{n_e n_i}{\lambda^2 T_e^{1/2}} \exp\left(\frac{-1.24 \times 10^{-4}}{\lambda T_e}\right) \frac{V_p}{4\pi} \frac{\text{watts}}{\text{cm sterr}} \quad (6.7)$$

for T_e in eV, λ in cm and V_p in cm^3 . At 10.6 μm g, the free-free Gaunt factor² was taken as 1.2 and with $Z = 1$, $n_e = n_i = 2 \times 10^{15} cm^{-3}$, $T_e = 3.5$ eV, $V_p = (0.2) (0.4) (1.5) cm^3$, $\Delta \Omega = 2.8 \times 10^{-2}$ sterr and $\Delta \lambda = 1.4 \times 10^{-5} cm$, $P_b = 1.3 \times 10^{-8}$ watts incident upon the detector. With a

detector responsivity at d.c. of $(2 \times 10^7 \text{ volts/watt}) (15 \text{ V/9 V}) (150 \text{ k}\Omega / 1.2 \text{ M}\Omega) = 4.2 \times 10^6 \text{ volts/watt}$, 54 mV would appear across the chip. However, placing the Fabry-Perot in the optical path drastically limits the incident bremsstrahlung watts. For example, a FSR of 245 Å implies 7 Fabry-Perot orders in the cooled filter bandpass. For 2 Å resolution and 10% transmission, $P_b = 1.3 \times 10^{-11} \text{ watts}$, producing $\approx 54 \text{ }\mu\text{V}$ of d.c. signal.

Due to the statistical nature of bremsstrahlung emission, the d.c. emission will be accompanied by a random noise level. Using Poisson statistics to describe these fluctuations, the noise power is given by³

$$P_N = (8 P_b h\nu)^{1/2} \text{ watts/Hz}^{1/2} \quad (6.8)$$

where $h\nu$ is the photon energy at the wavelength of interest. For 10.6 μm , $h\nu = 1.87 \times 10^{-20} \text{ J}$. Bremsstrahlung noise power is therefore $P_{Nb} = 1.4 \times 10^{-15} \text{ watts/Hz}^{1/2}$. The 5 μsec risetime implies a system bandwidth of 70 kHz, and assuming a responsivity of $4.2 \times 10^6 \text{ volts/watt}$, a noise voltage of 1.5 μV results with etalons in the optical path.

Another noise source is Johnson thermal noise which appears in all electronic systems. Its RMS amplitude is given by

$$V_{NJ} = (4kTRB)^{1/2} \text{ volts} \quad (6.9)$$

where R is a resistance at temperature $T^\circ\text{K}$ and B is the electrical bandwidth. For $R = 150 \text{ k}\Omega$, $T = 295^\circ\text{K}$ and $B = 70 \text{ kHz}$, $V_{NJ} = 13 \text{ }\mu\text{V}$.

A third noise source is that alluded to earlier in the discussion of detector characteristics, namely fluctuations in room temp-

erature blackbody radiation. This may be treated in a similar manner to the bremsstrahlung - d.c. emission level plus attendant statistical noise. The Wein-Planck radiation law gives the blackbody intensity at temperature T⁰K, as

$$I(\lambda, \Omega) = \frac{1.2 \times 10^4}{\lambda^5} \left[\exp\left(\frac{1.44 \times 10^4}{\lambda T}\right) - 1 \right]^{-1} \frac{\text{watts}}{\mu\text{m cm}^2 \text{sterr}}$$

for λ in μm. Detector design was such that the chip of area 2x10⁻²-cm² subtended a solid angle of 0.1 sterr. For a filter bandpass of 0.14 μm, the emission incident on the detector from a 295⁰K environment is 2.5x10⁻⁷ watts. From eqn. 6.8, the associated noise power is 1.9x10⁻¹³ watts/Hz^{1/2}, which for 70 kHz bandwidth and 4.2x10⁶ volts/watt responsivity means a noise voltage of 210 μV RMS across the detector chip. Of the random noise sources, room temperature radiation is quite clearly dominant. The calculated noise levels, then, appear to be considerably smaller than expected signal levels.

6.5 Experimental Noise Levels

Measured noise levels were reasonably close to the calculated amplitudes. For detector bias voltage of 15 V, total broadband noise input to a Tektronix 1A7A preamplifier was ~ 140 μV RMS. For V_{BIAS} = 4.5 V, the noise level was ~ 50 μV RMS. There was no observable difference in these levels for plasma ON and plasma OFF, the conclusion being that room temperature background noise indeed predominated, and bremsstrahlung and thermal noise were small by comparison. Inherent

oscilloscope noise for these measurements was $\sim 7 \mu\text{V RMS}$, a negligible contribution.

6.6 Experimental Signal Levels

Observed scattered signals were appreciably less than anticipated levels. A major factor contributing to this situation involved the experimental scattering volume, which was found to be smaller than the idealized volume used in previous signal calculations. The optical system was designed to ideally image a plasma cross-section of $2 \text{ mm} \times 4 \text{ mm}$ on the detector chip, which, for viewing at 30° to the laser axis, translates into a scattering volume of 25 mm^3 for a 2 mm focal spot diameter. Detailed measurements showed that the observable scattering volume was $\sim 5 \text{ mm}^3$, a factor of 5 smaller.

Divergence of light reaching the detector was limited by the 2.5 cm focussing lens aperture, which in turn defines the observable plasma cross-section perpendicular to the Cassegrainian axis. While use of a larger lens would have undoubtedly increased integrated scattered signals, it was pointless to do so because of Fabry-Perot light quality requirements. As mentioned in Chapter 4, to achieve a resolving power RP , light incident on the etalons must have full angle divergence less than $\theta_{\text{div}} = 2/(RP)^{1/2}$, which implies $\theta_{\text{div}} = 9 \text{ mrad}$ for 2 \AA resolution.

For source points a distance $\pm h$ measured perpendicular to the Cassegrainian axis, light divergence may be calculated from consideration of the lens system shown in Fig. 6.5, which represents the detection optics. Since $2 h' = f_1 \theta_{\text{div}}$ and $2 h \phi_0 = 2 h' \phi_1$,

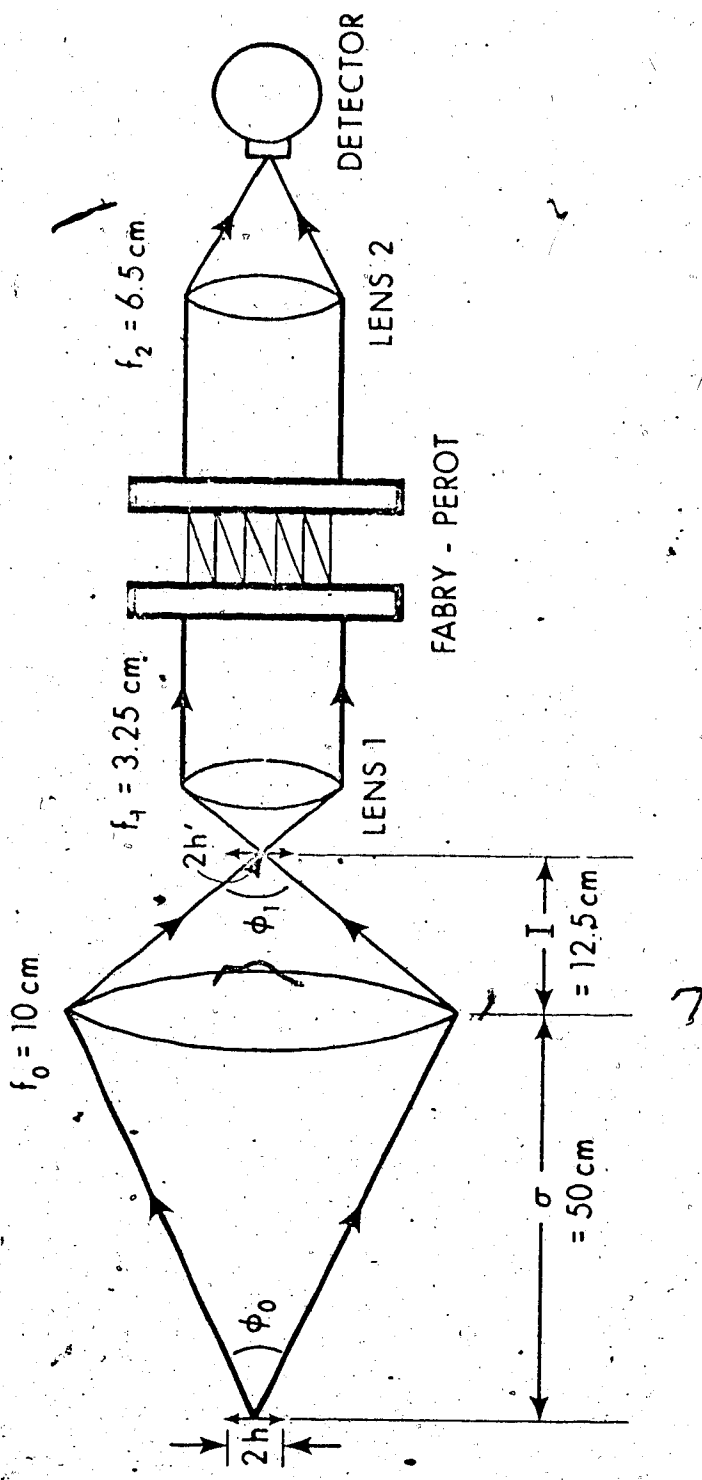


Fig. 6.5 Equivalent lens system for the detection optics.

$$\theta_{\text{div}} = \frac{\phi_0}{\phi_1} \frac{2h}{f_1} = \frac{I}{\sigma} \frac{2h}{f_1} \quad (6.11)$$

For $\sigma = 50$ cm, $I = 12.5$ cm and $f_1 = 3.25$ cm, eqn. 6.11 yields $\theta_{\text{div}} = 9$ mrad for $h = 0.6$ mm, which implies a divergence-limited plasma cross-section of 1.2 mm by 1.2 mm. The resulting useful scattering volume is ~ 5 mm³.

Depth of field along the Cassegrainian axis does not further limit the volume. This may be seen by considering the divergence from sources at $\sigma \pm \Delta\sigma$. Since

$$\frac{dI}{d\sigma} = \frac{d}{d\sigma} \left(\frac{\sigma f_0}{\sigma - f_0} \right) = -\frac{I^2}{\sigma^2} \quad (6.12)$$

then

$$\Delta I = -\frac{I^2}{\sigma^2} \Delta\sigma, \quad \Delta\sigma \ll \sigma \quad (6.13)$$

Light from $\sigma \pm \Delta\sigma$ is now divergent upon passing through lens 1. Images are formed at distances I_1 from lens 1 which satisfy

$$\frac{1}{f_1 \pm \Delta I} + \frac{1}{I_1} = \frac{1}{f_1} \quad (6.14)$$

i.e.

$$I_1 \approx \frac{f_1^2}{\Delta I}, \quad \Delta I \ll f_1 \quad (6.15)$$

Divergence is given by $\theta_{\text{div}} = a/I_1$ where a is the aperture of lens 1.

Substituting eqn. 6.13 into eqn. 6.15, the result is

$$|\theta_{\text{div}}| = \frac{a^2 \Delta \cdot \sigma}{f_1^2 \sigma^2} \quad (6.16)$$

For $\theta_{\text{div}} = 9 \text{ mrad}$, $|\Delta| = 0.75 \text{ cm}$ for a 1.5 cm divergence-limited depth of field, much greater than the effective laser-plasma column interaction length.

Another factor which decreased experimental signal levels was deterioration of detector performance. When larger (10 V - 15 V) bias levels were used, electrical breakdown across the detector chip occurred and random noise spikes of up to 50 mV amplitude were observed in the output. To avoid breakdown entirely, a bias voltage of 4.5 V was employed in all scattering measurements. Since the 3.3 times decrease in responsivity affected signal and noise (room temperature background) equally, the loss in overall signal to noise was small.

Electrical breakdown of the detector was attributed to probable adsorption of water vapour on the surface of the chip. A baking procedure⁴ was attempted with the hope of evaporating the water contaminant and restoring detector performance. This proved partially successful in that noise spikes were reduced to $\sim 1 \text{ mV}$ for 15 V bias. However, this mV noise proved too much for reliable signal processing and $V_{\text{BIAS}} = 4.5 \text{ V}$ was used in all experimental runs.

Taking into account reduced scattering volume and detector responsivity, the measured integrated scattered signals of 3 to 4 mV were within a factor of 2.7 of the revised calculated value of

$$158 \text{ mV} \times \frac{4.5 \text{ V}}{15 \text{ V}} \times \frac{5 \text{ mm}^3}{25 \text{ mm}^3} = 9.5 \text{ mV} \quad (6.17)$$

Considering the numerous factors influencing this calculation, the agreement is fairly reasonable.

Signal from integrated stray laser light was (4 ± 1) mV for $\theta = 150^\circ$ and (13 ± 3) mV for $\theta = 30^\circ$. The necessity of the precautions taken to reduce stray light was vividly illustrated by removing the stray light cone whereupon background signal increased 2 orders of magnitude.

Integrated scattering was of approximately the same level for both $\theta = 150^\circ$ and $\theta = 30^\circ$. Arc conditions were $P = 3$ Torr, $V = 32$ V and $I = 275$ A, and subsequent spectra were taken for these arc parameters as well. Earlier investigations of 150° backscatter using the 1 MW CO_2 pulsed laser showed that maximum integrated signal occurred in the 3 - 4.5 Torr pressure range, falling to $\sim 50\%$ of maximum at $P = 1$ Torr and remaining within 20% of maximum for $5 \text{ Torr} < P < 10 \text{ Torr}$.

6.7 Experimental Fabry-Perot Instrument Functions

For a given etalon separation, Fabry-Perot profiles for an extended source are broader than corresponding point source functions. Careful measurements were carried out to determine profiles for the entire scattering volume. The scattering ball was moved across the plane of the laser-plasma intersection in a grid pattern with the point source function recorded at 0.3 mm intervals. Summation of these yielded a resultant instrument function for the scattering volume, since the result for a given plane through this volume would be the same as

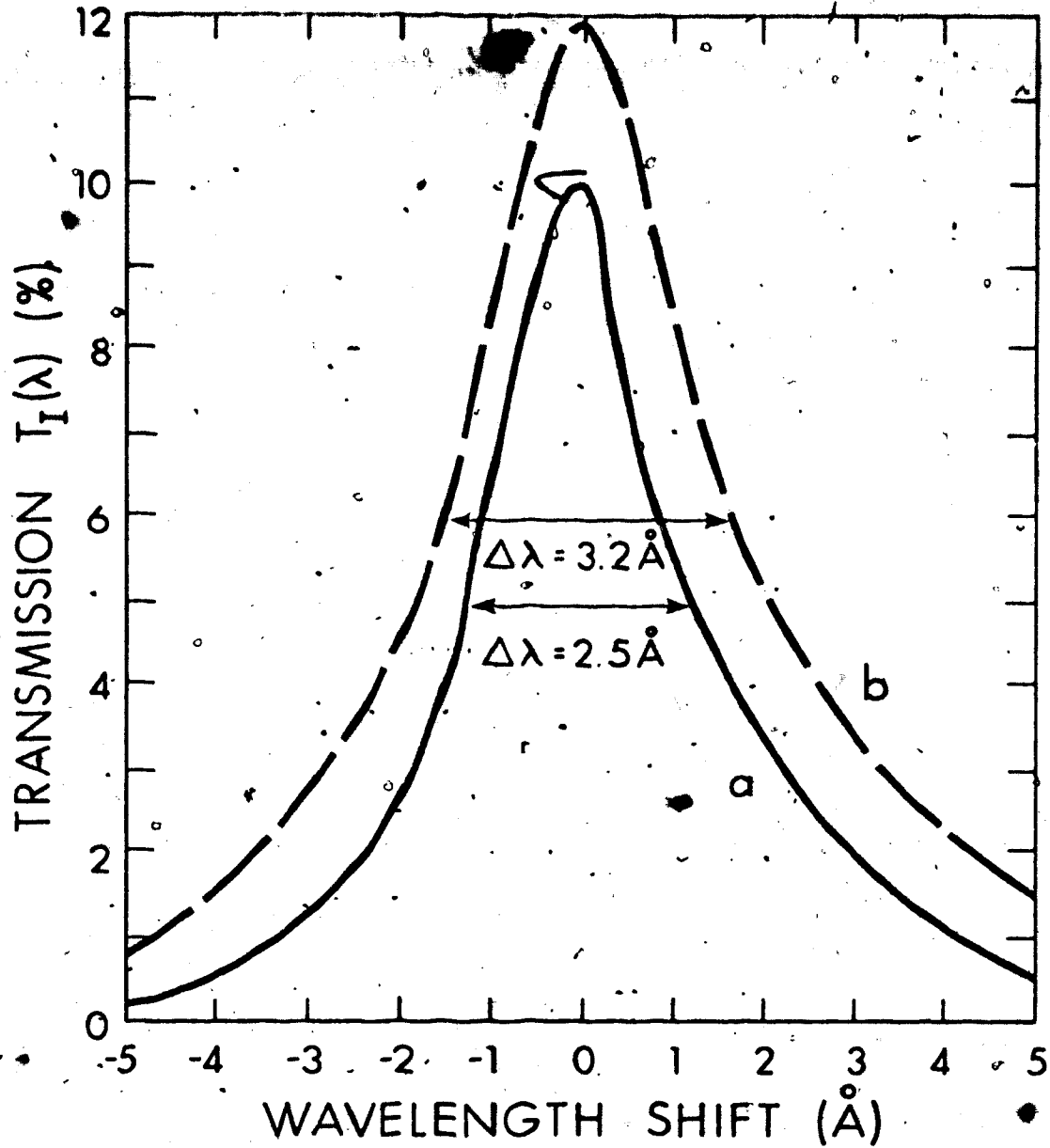


Fig. 6.6 Fabry-Perot profiles for the scattering volume; (a) for resolving $\theta = 30^\circ$ forward scattering with 1 \AA point source resolution and etalon separation 0.23 cm; (b) for resolving $\theta = 150^\circ$ back-scattering with 2 \AA point source resolution and etalon separation 0.52 cm.

98

that for any other parallel plane. For 2 Å and 1 Å point source resolutions, extended source resolutions of 3.2 Å and 2.5 Å respectively were obtained. The extended source profiles are plotted in Fig. 5.6.

6.8. Enhancement of Signal/Noise

Experimental scattered signals were sufficiently small that placement of the Fabry-Perot in the optical path required additional measures to improve the resulting signal to noise. For 150° backscatter, a 3 Å Fabry-Perot bandpass with 6% average transmission placed on a 7 Å wide spectrum would pass 2.6% of the integrated signal - about 90 μV. For 30° forward scatter, a 2.5 Å bandpass with 5% average transmission placed on a 2.5 Å wide spectrum would result in a signal of 175 μV peak amplitude. With 50 μV RMS noise voltage in both cases, S/N was 1.8 and 3.5, respectively.

A P.A.R.L. boxcar integrator was used to improve these S/N ratios. This instrument accepts a voltage waveform consisting of signal + noise and analyses the waveform for a time Δt , evaluating its average value in this interval. The averaging process is characterized by a time constant T . Information is stored in the form of a d.c. voltage. After a train of n pulses are supplied to the boxcar integrator input channel, the d.c. output voltage will have reached a value proportional to the mean waveform amplitude during Δt .

$$V_{OUT} = V_{MEAN} (1 - e^{-n\Delta t/T}) \quad (6.18)$$

In the process, the average of the noise component is computed as well.

For random noise, this average approaches zero as the number of data inputs becomes very large. For n samples, the S/N of the input waveform is improved by $n^{1/2}$ when $n\Delta t/T \leq 1$ (linear averaging).

In Fig. 6.7, the electronic setup for signal processing is indicated. The 1A7A preamplifier output of the Tektronix oscilloscope was utilized in order to increase signal levels to meet input sensitivity requirements of the boxcar integrator. Preamplifier output impedance was 1 k Ω and boxcar input impedance 100 k Ω . Preamplifier gain of 1.3×10^3 increased signal amplitudes (and noise) to 100 mV levels.

For spectral scans of 150 $^\circ$ backscatter, 20 shots were averaged to obtain each spectral point. Ten samples per point were taken in the case of 30 $^\circ$ forward scattering. Boxcar ON time was 15 μ sec, synchronized to the scattered signal with a jitter of < 100 nsec. (Fig. 6.8). An averaging time constant T of 300 μ sec was used. Resulting S/N for backscattering was $1.8 (20)^{1/2} = 8$ and $3.5 (10)^{1/2} = 11$ for forward scattering. From eqn. 6.18, boxcar output levels were 63% of the mean signal amplitude in the backscattering case and 40% of the mean for forward scattering.

There was one more troublesome noise problem which had to be dealt with. This was pickup from the CO₂ laser high voltage discharges. To protect the boxcar integrator input circuit, the noise spike (see Fig. 6.8) had to be limited to less than 2 mV at the 1A7A input. Thorough electrostatic shielding of the detector cable and bias box, along with placing the detector-to-preamplifier cable close to a fast ground served to sufficiently limit the pickup. Internal detector connections

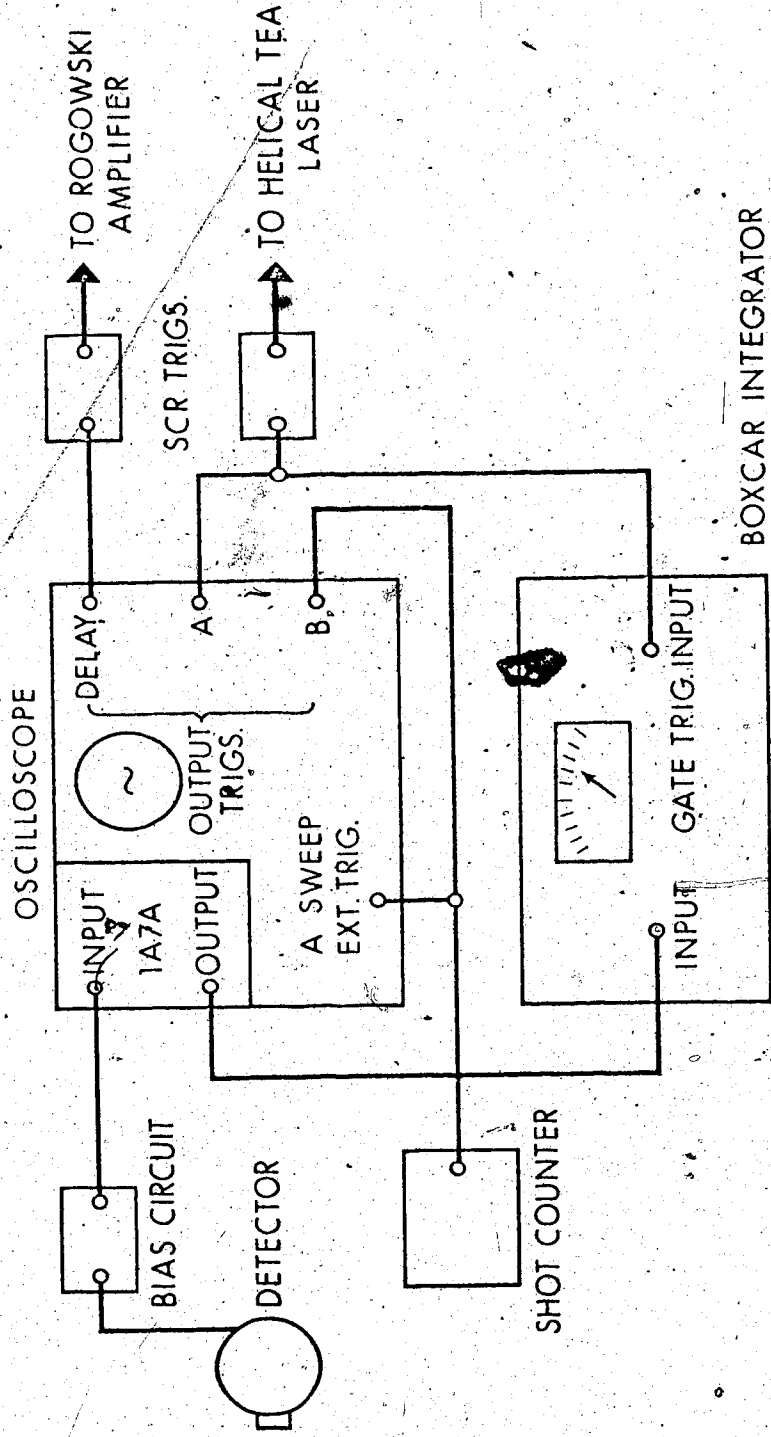
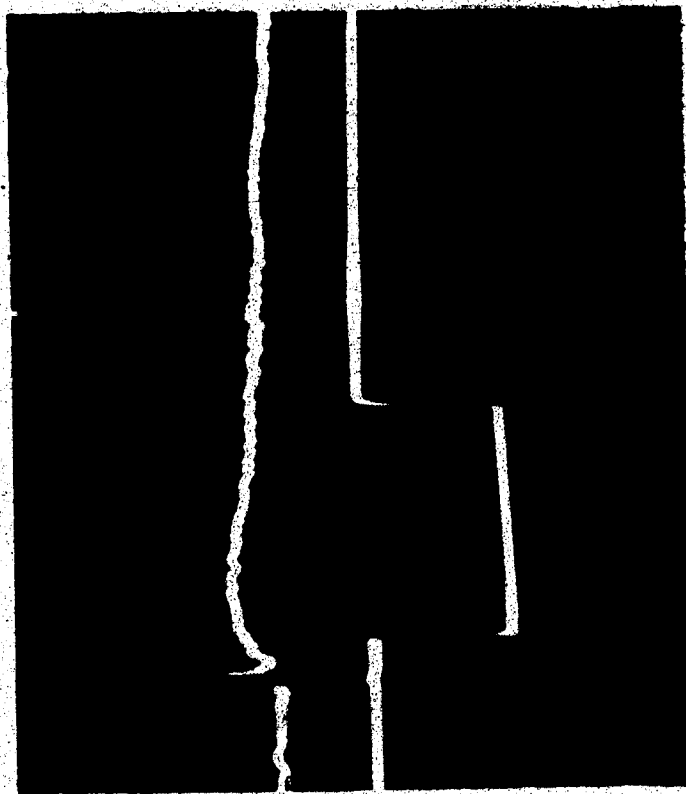


Fig. 6.7 Detection and synchronization electronics for scattering.



SCATTERED SIGNAL

+ NOISE $200\mu\text{V}/\text{div}$

BOXCAR INTEGRATOR

GATE

$5\mu\text{sec}/\text{div}$

Fig. 6.8 Synchronization of boxcar integrator gate to resolved scattered signal. Peak of discharge noise spike is off-scale.

were protected by a built-in radiation shield.

6.9 CO₂ Laser Scattering Results and Discussion

For 150° backscattering, data from 4 spectral runs are shown in Fig. 6.9. The 10 MW CO₂ oscillator-amplifier was the radiation source, with $E_0 = 2.5$ J in a single pulse. Forward scattering data from 2 spectral runs are shown in Fig. 6.10. The 6.7 m CO₂ oscillator was the incident source with ~ 2 J per pulse.

Individual data points represent the difference between n shots with plasma ON and n shots with plasma OFF at the wavelength indicated. In this way, the contribution of stray light was removed. The Fabry-Perot interferometer was seen to attenuate stray light a factor of 2 - 3 more than the scattered signal, probably because the scattering source was much more localized than the multi-sources of stray light. Such sources were located in the plasma chamber only, as the detector and Fabry-Perot were completely shielded from externally scattered laser light. This was checked by achieving a zero reading on the boxcar integrator for n shots with the Cassegrainian output blocked.

In Figs. 6.11 and 6.12, the experimental data are compared with calculated scattering profiles. Vertical error bars represent statistical amplitude deviations. If there are m data points of ordinate value x_i with approximately equal abscissas, the deviation of a single reading is given by

$$\sigma = \pm \left(\frac{\sum_{i=1}^m (x_i - \bar{x})^2}{(m-1)} \right)^{1/2} \quad (6.19)$$

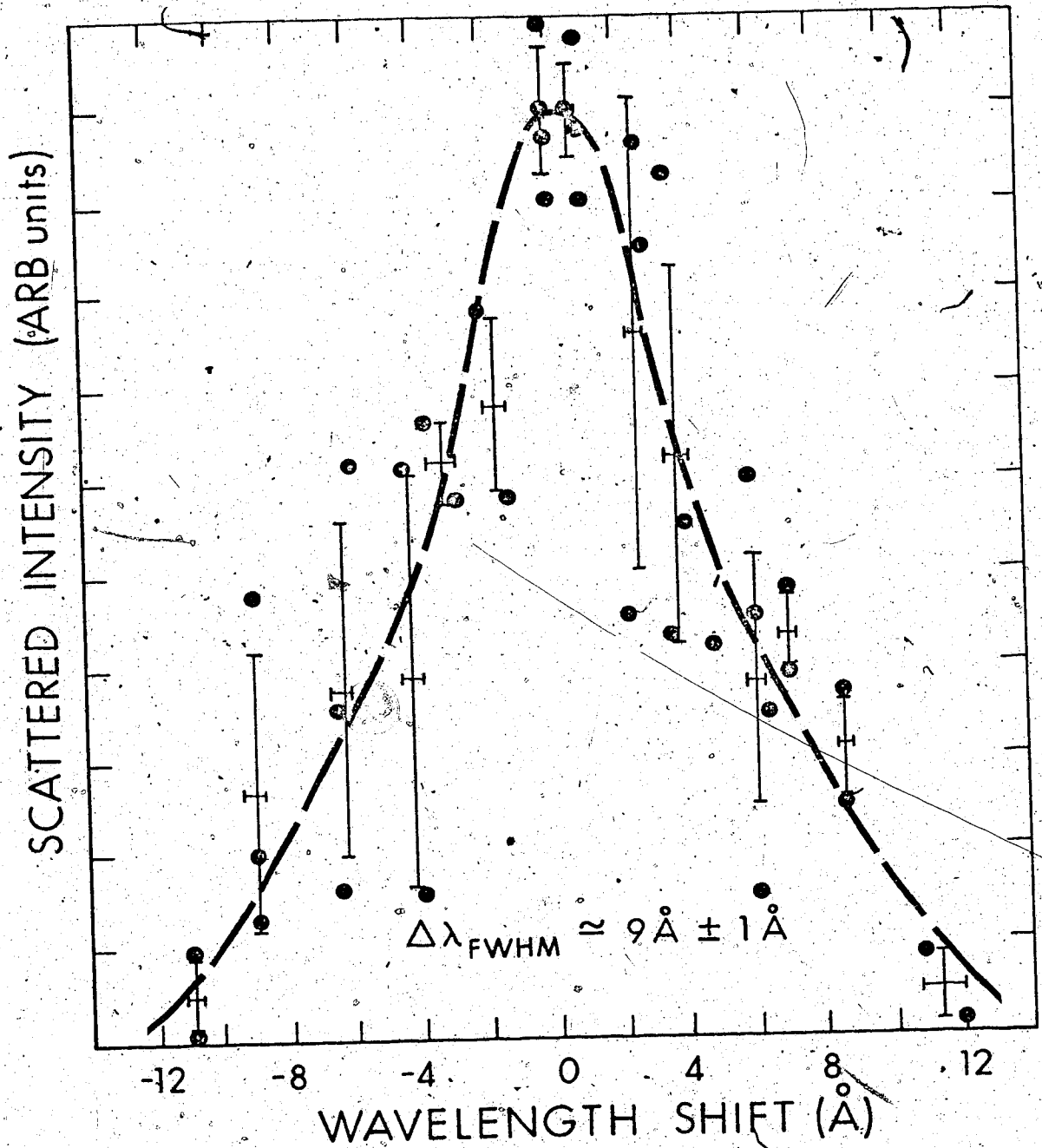


Fig. 6.9 Experimental data for $\theta = 150^\circ$ backscatter.

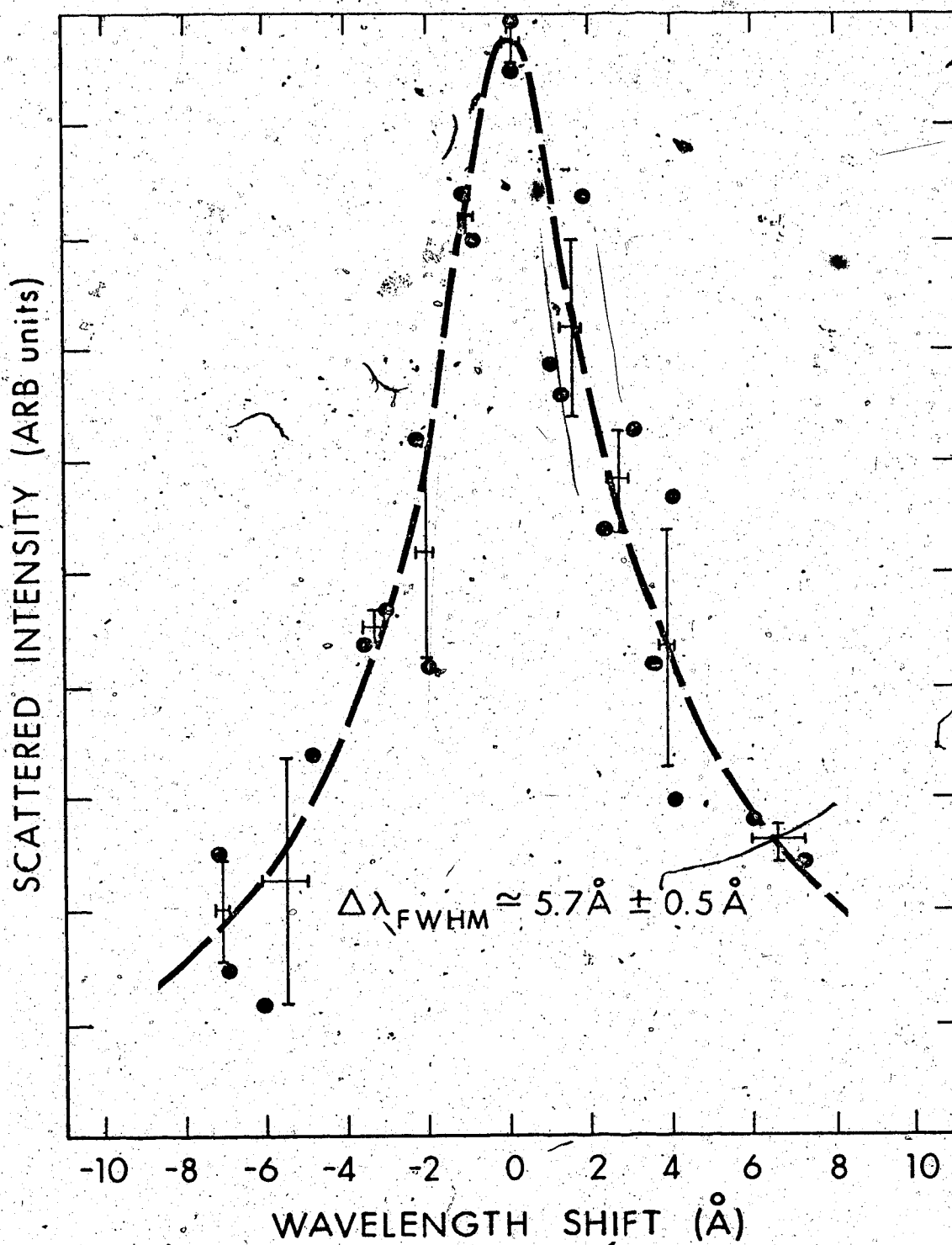


Fig. 6.10 Experimental data for $\theta = 30^\circ$ forward scatter.

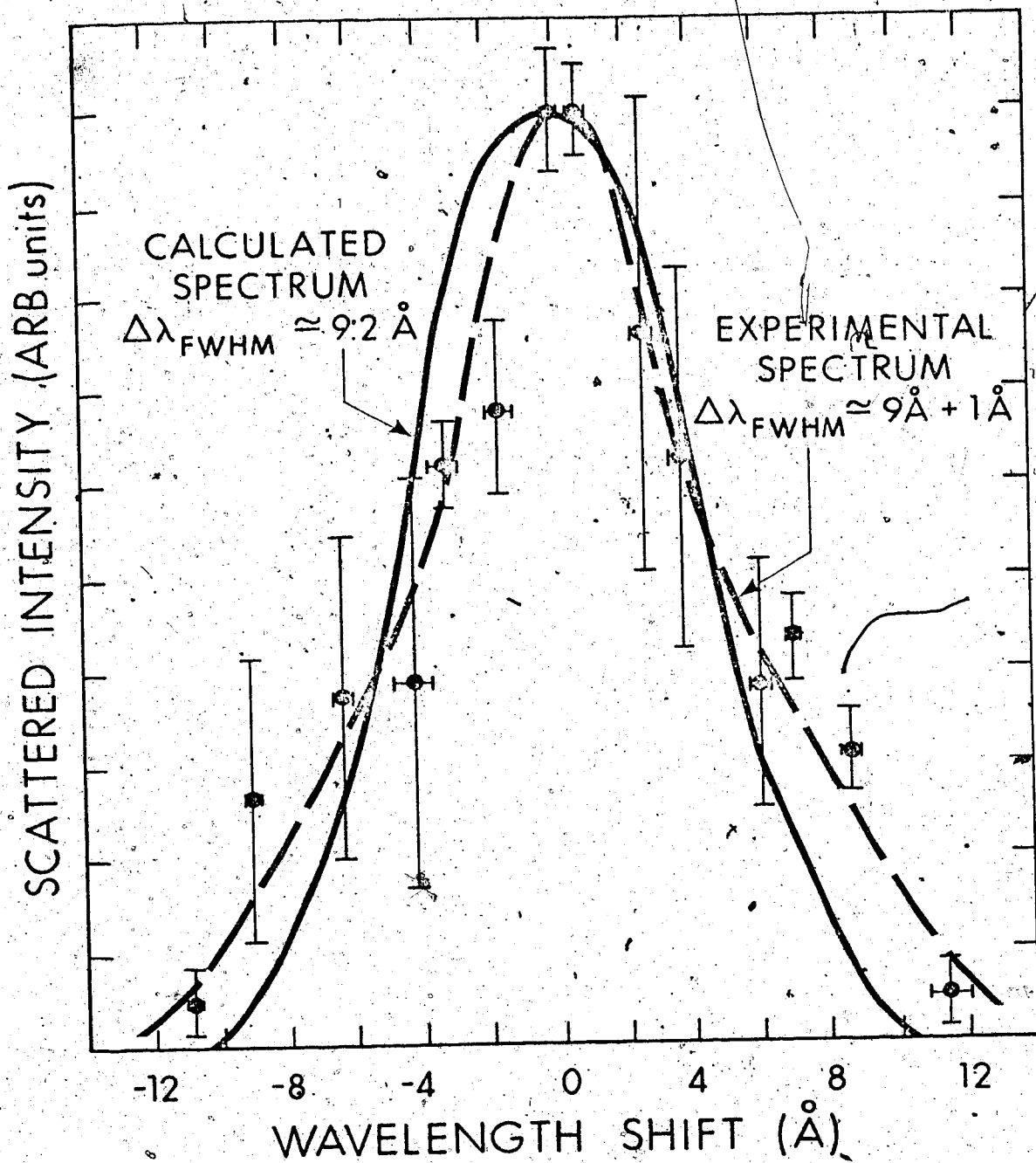


Fig. 6.11 Comparison of experimental and calculated spectra for $\theta = 150^\circ$ backscattering. Calculated spectrum $I_S(\lambda)$ includes the effect of a 3.2 \AA Lorentzian instrument function.

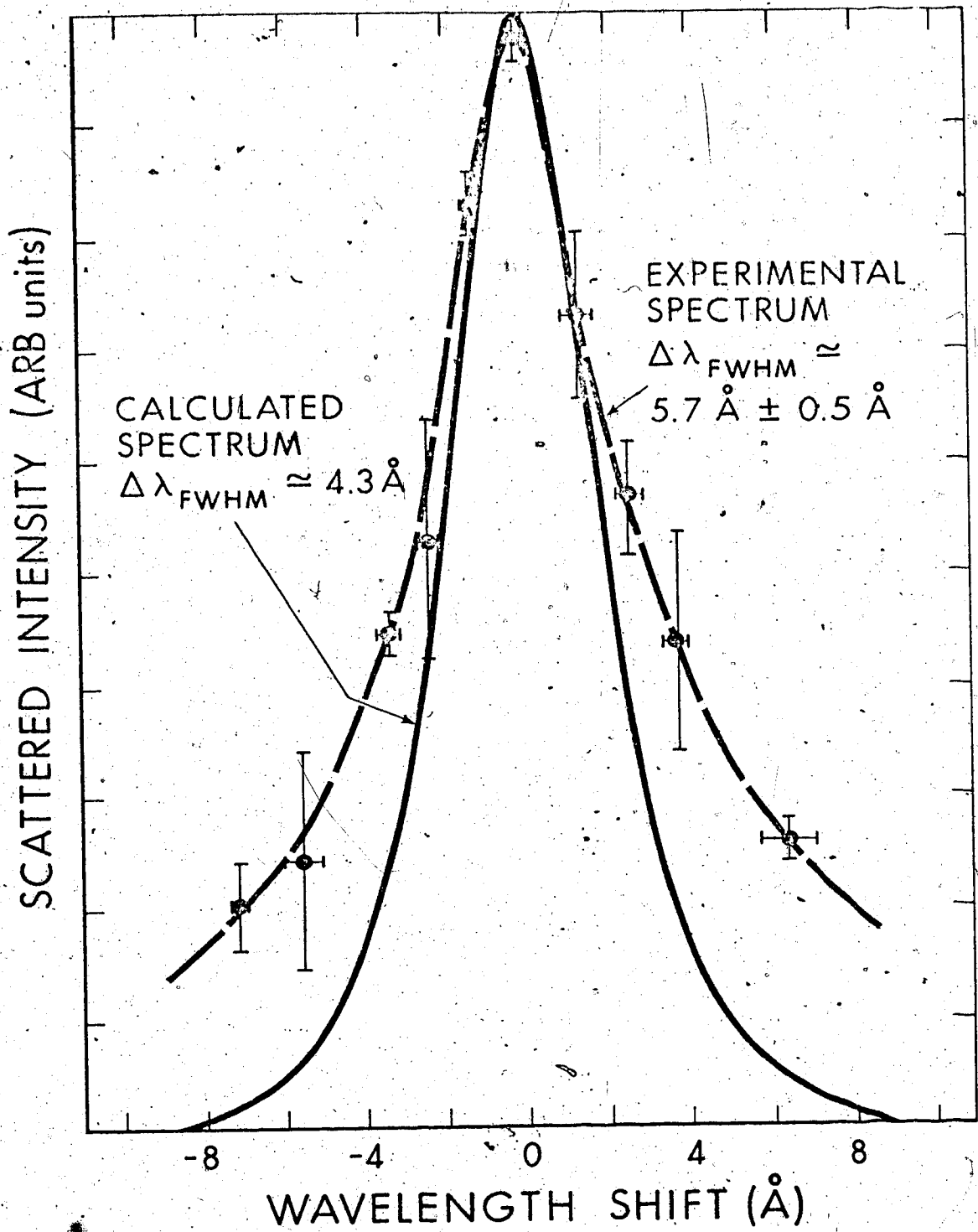


Fig. 6.12 Comparison of experimental and calculated spectra for $\theta = 30^\circ$ forward scattering. Calculated spectrum $I_S(\lambda)$ includes the effect of a 2.5 \AA Lorentzian instrument function.

where \bar{x} is the mean value of x_i 's. Horizontal error bars describe the uncertainty in the Fabry-Perot wavelength setting.

To obtain the calculated scattering profiles, convolution of the I_{BL} 's (Figs. 6.1 and 6.2) with the Fabry-Perot functions $T_I(\lambda)$ for the scattering volume (Fig. 6.6) was carried out. The convolution integral is

$$I_S(\lambda) = K_2 \int_{-\infty}^{\infty} I_{BL}(\lambda') T_I(\lambda - \lambda') d\lambda' \quad (6.20)$$

where K_2 is a normalization constant. The I_S functions for $\theta = 150^\circ$ and $\theta = 30^\circ$ were computed numerically, approximating $T_I(\lambda)$ by Lorentzian curves of FWHM 3.2 \AA and 2.5 \AA respectively.

Convolved widths of backscattered and forward scattered spectra were found to be 9.2 \AA and 4.3 \AA . Agreement with the experimental backscattered spectral width ($\sim 9.0 \text{ \AA}$) is quite good, while there is a 30% difference between the calculated and experimental width ($\sim 5.7 \text{ \AA}$) for 30° forward scattering. Such a discrepancy is not surprising in view of the considerable influence of laser and instrumental widths upon this narrower spectrum.

Unfortunately the rather indistinct ion acoustic resonances are easily masked unless one employs extremely fine resolution. Since the useful scattering volume decreases linearly with increasing RP, the task of recovering the $\theta = 150^\circ$ spectrum would be very difficult with, say, $< 1/2 \text{ \AA}$ resolution unless laser power was correspondingly increased. The laser line itself smears out the features of the $\theta = 30^\circ$ ion spectrum.

The experimentally obtained $\theta = 150^\circ$ ion spectrum exhibits the

broadening expected for 2 eV argon ions, given that instrumental profile effects are predictable. Since spectral width varies as $T_i^{1/2}$, 10% error in $\Delta \lambda$ implies a 20% uncertainty in T_i .

Both forward and backscattered spectra are slightly skewed towards the long wavelength side of line centre. Such a skewing may be due simply to the statistics of information recovery, or to some slight systematic error in Fabry-Perot alignment and hence instrumental shape.

These results constitute the first resolved scattered spectra and measurement of thermal ion fluctuations using a pulsed CO_2 laser as incident source. The technique should prove suitable for probing even lower density plasmas, as presently available CO_2 pulsed laser powers are 2 orders of magnitude higher than the 10 MW levels used in these investigations. Experiments with hotter plasmas would not have the stringent resolution requirements and associated difficulties of the present one.

6.10 Cooperative CO_2 Scattering from a Tokamak Plasma

Returning to the discussion (in Chapter 2) of scattering from Tokamak plasmas, it is now possible to outline the design parameters for a CO_2 small angle scattering measurement.

Assume $n_e = 10^{14} \text{ cm}^{-3}$ with $T_e = T_i = 500 \text{ eV}$ (case 1) and $T_e = T_i = 2 \text{ keV}$ (case 2). A deuterium plasma has $Z = 1$.

Consider case 1 first. For $\alpha = 1$, $\theta = 5.8^\circ$ is required. The scattered spectrum will have an ion feature ($\beta = 0.7$) with 25% of the

scattered power and an electron feature containing the remainder. The ion feature is almost Gaussian in shape with a FWHM (eqn. 6.1) of $\sim 16 \text{ \AA}$. The electron spectrum is flat-topped with a FWHM of $\sim 1400 \text{ \AA}$ (note $\bar{v}_e/c \ll 1$, so there are no relativistic effects).

Collecting light from an annulus defined by half angles of 4.8° and 6.8° (for definition of α) implies $\Delta \Omega = 2.3 \times 10^{-2}$ sterr. Now

$$P_s = r_e^2 \frac{1 + Z \alpha^2}{1 + (Z + 1) \alpha^2} P_0 n_e \ell \sin^2 \delta \Delta \Omega \text{ watts} \quad (6.21)$$

Taking $P_0 = 10^8$ watts, $\ell = 1$ cm, $\sin^2 \delta = 1$ (forward scattering) yields $P_s = 1.2 \times 10^{-5}$ watts = $P_{si} + P_{se}$.

Suppose that the laser beam is focussed by an $f = 50$ cm lens to a 1 mm diameter spot and scattered light is collected by an $f = 25$ cm lens located 50 cm from the laser focus. Then the collecting aperture has an 8.5 cm inner diameter and the laser beam must be somewhat smaller than this in order that large amounts of stray light do not enter the collection system. Excellent discrimination against laser stray light is of prime importance.

A model of a possible collection-resolution-detection system is shown in Fig. 6.13. A Fabry-Perot with 3 \AA resolution ($\theta_{div} < 10.6$ mrad) is needed for the ion component and a monochromator with 250 \AA resolution for the electron portion of the spectrum. The lens system is set up for $M = 1$ and supplies light for the Fabry-Perot with full angle $\theta_{div} \leq 10$ mrad from a 1 cm depth of field and a 1 mm focal spot. (eqns. 6.11 and 6.16).

Detector noise is background radiation limited. Because of

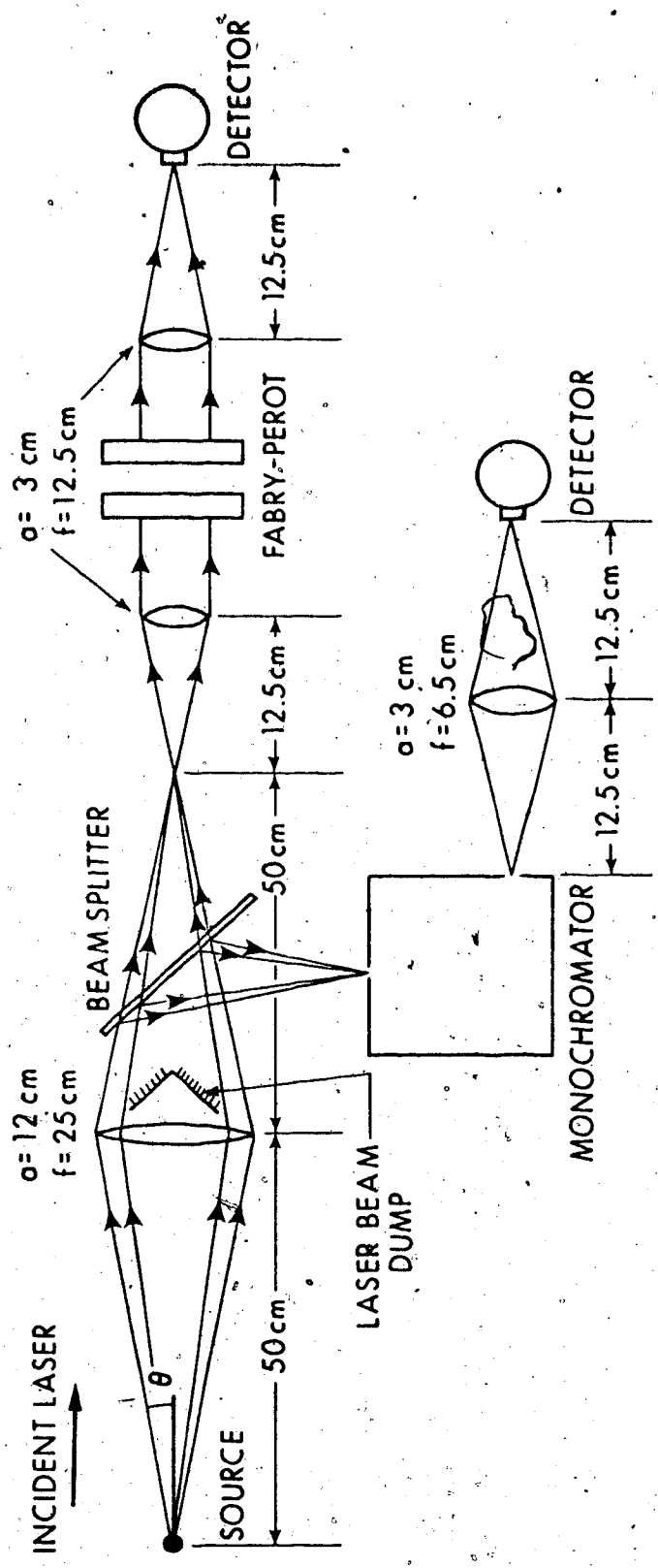


Fig. 6.13 Optics for small angle C02 laser scattering from a Tokamak plasma.

lower n_e and higher T_e , plasma bremsstrahlung is at least 3 orders of magnitude less than that in the argon arc scattering system. A 1 mm x 1 mm detector subtending $\pi (1.5^2 \text{ cm}^2)/12.5^2 \text{ cm}^2 = 4.5 \times 10^{-2}$ ster is required and a 0.3 μm bandpass filter is needed in front of the chip. From eqns. 6.8 and 6.10 the noise power is 1.3×10^{-13} watts/Hz^{1/2}. With electrical bandwidth and 15 V bias responsivity as before, $V_N = 150 \mu\text{V}$.

Optical transmission for 3 lenses and the Fabry-Perot (5%) is 3.9%. For a 3 \AA bandpass, the transmitted scattered power is

$$.039 P_{si} \times \frac{3 \text{ \AA}}{16 \text{ \AA}} = 2.2 \times 10^{-8} \text{ watts} \quad (6.22)$$

resulting in a signal of $\sim 260 \mu\text{V}$ on the detector and S/N of 1.7.

For the electron spectrum, an overall optical transmission of 39% (50% for the monochromator) would yield S/N of 50, as $P_{se} = 3 P_{si}$. A beam-splitter could provide an alternate path to a second detector for simultaneous recovery of electron and ion spectra. Electron S/N would then be $50 R$ and ion S/N $1.7(1-R)$ where R is the beam-splitter reflectivity. $R = 0.1$ would be appropriate in this case. A better situation would likely result from utilization of a multi-channel detection system, whereby information is accumulated in the fewest possible number of shots, assuming sufficient S/N in each channel.

Determination of P_{si}/P_{se} and T_e enables calculation of n_e because this scattered power ratio⁵ is a function of α , which in turn depends on n_e and T_e .

For case 2, $\theta = 2.9^\circ$ is required for $\alpha = 1$. Discrimination against laser light is even more crucial, as the CO_2 beam diameter must

certainly be ≤ 4.2 cm. For a definition, light from $\theta = 2.9^\circ \pm 0.5^\circ$ may be collected for $\Delta \Omega = 6 \times 10^{-3}$ ster. For this scattering angle, spectral widths are equal to those in case 1. The lens apertures of Fig. 6.13 may be halved; otherwise the optics are similar. This doubles the allowable depth of field for adequate Fabry-Perot resolution and allows detector design such that $\Delta \Omega_{det}$ is a factor of 4 less than previously. Combined, these two factors overcome the decrease in collection solid angle so that S/N ratios remain equal to those calculated for case 1.

To analyse one further situation, consider $\alpha = 2$ scattering for case 1 ($T_e = T_i = 500$ eV). The optical system and detectors for case 2 may be used, as $\theta = 2.9^\circ$. From eqn. 6.21, $P_s = 5 \times 10^{-6}$ watts for $l = 2$ cm. Now, however, $P_{si} = 0.65 P_s$ and $P_{se} = 0.35 P_s$.

The ion spectrum has $\beta = 0.9$ and is approximately 12 Å FWHM. Electron plasma frequency satellites are included in the electron spectrum and are located ± 450 Å from line centre; in terms of frequency the shift is about $1.3 \omega_{pe}$. Assuming Landau damping is the dominant broadening mechanism, the width of these resonances is ~ 100 Å. Either a high resolution (~ 25 Å) monochromator or a relatively low resolution Fabry-Perot would be sufficient to resolve this portion of the spectrum. For the ion spectrum, S/N with 3 Å Fabry-Perot resolution (possible if $l \leq 2$ cm) is ~ 5 . In the electron spectrum, about $1/4 P_{se}$ is in each satellite. Using a Fabry-Perot with 25 Å resolution and 10% average transmission, $S/N = 1.4$ may be obtained. Again, 2 optical paths may be used for simultaneous recovery of spectra, S/N reduction dependent on the particular division of scattered light by a beam-splitter. Further improvement of S/N in all cases may be realized with a multi-shot

averaging technique similar to that described earlier.

In a Tokamak, toroidal magnetic fields may influence spectral features. For example, consider case 1 with $B_T = 40$ kG and the CO_2 laser axis perpendicular to field lines. Ω_e is comparable to ω_e , in fact $\Omega_e/\omega_e = 0.9$. Consequently, the electron spectral shape may be observably different from the field free situation and B field information may thus be available. For the ions, $\Omega_i/\omega_i = 1.4 \times 10^{-2}$ so that \underline{K} must be within 0.3° of the perpendicular to B_T . For the chosen annulus of scattering angles, \underline{K} is within 1.0° of the perpendicular to B_T , so modulation of the ion spectrum will occur with $\Delta \lambda_{MOD} \approx 0.1$ Å, probably too fine a structure to be observable.

The foregoing considerations show that CO_2 cooperative scattering from present day Tokamak plasmas is feasible in general. Success of the technique hinges upon the ability to discriminate exceedingly well against laser stray light, always a formidable problem in small angle scattering. Another concern is, of course, optical system compatibility with the Tokamak physical layout.

CHAPTER VII

SUMMARY AND CONCLUSIONS

The magnetized argon arc facility which has been constructed has served as a useful laboratory source for the study of plasma properties and the development of diagnostic techniques. This steady state, quiescent plasma is a convenient laboratory source for investigations into such areas as turbulence, instabilities and laser heating.

Probe and spectroscopic measurements were carried out in order to expedite Thomson scattering experimental design. They have also served to expand and establish the body of experimental data for the arc plasma parameters.

Biased probes have been operated under extremely high heat flux conditions and in an interesting new regime affected by both charged particle collisions and magnetic fields. Spatially resolved electron densities and temperatures have been determined for this type of arc for the first time. Further investigation could lead to a more complete understanding of electrostatic probe behaviour in such circumstances.

Ar II Doppler broadening measurements have yielded accurate ion temperature information, while observation of Zeeman splitting of transitions has confirmed Hall probe measurements of magnetic field strength in the arc.

A high power CO₂ laser system was constructed in order to provide sufficient Thomson scattered power levels from the arc plasma. A 10 MW oscillator-amplifier and a 20 MW oscillator were both used in

scattering experiments. Multi-shot wavelength spectra were obtained for these lasers and the effect of laser chromaticity on scattered spectra has been evaluated.

Numerical studies have been made concerning perturbations of the magnetized plasma arising from absorption of CO₂ laser radiation. Electron heating and laser induced ionization were considered. Plasma line emission under high laser flux conditions has been monitored. Both calculations and experimental observations showed that plasma perturbations for the present laser-plasma system were insufficient to influence Thomson scattering results. In general, multi-MW CO₂ lasers may be employed in scattering diagnostics without disturbing the plasma medium, provided electron densities are $< \sim 10^{16} \text{ cm}^{-3}$ and electron temperatures are $> \sim 1 \text{ eV}$.

The most important result of experimental investigations has been the demonstration of pulsed CO₂ laser cooperative Thomson scattering as a viable diagnostic for relatively low density plasmas.

Fabry-Perot resolved ion spectra have been obtained for the first time using a pulsed 10.6 μm source. Scattered information was processed using a boxcar integrator for S/N improvement. Ion temperatures deduced from scattering data were in good agreement with Ar II Doppler broadening results.

In order to further develop this technique, which has considerable diagnostic potential for hot, tenuous plasmas such as present Tokamaks, more work must be done, especially with regard to engineering design of small angle scattering experiments. Success of such experiments depends upon minimization and rejection of laser stray light by input and detection optics. Extremely good CO₂ laser-beam characteristics

are thus a necessity. Low divergence, single transverse mode output for high power, wide aperture (several cm) lasers is desirable in this respect. Associated optical components need be of the highest quality. In the interest of improving detector response, the use of longer pulse (> several usec) CO₂ lasers of sufficiently high power should be investigated. Availability of high sensitivity, multi-channel IR detection schemes along the lines of current systems for visible detection would greatly assist CO₂ Thomson scattering development.

Another possible scheme for small angle pulsed CO₂ scattering is the heterodyne method of detection, wherein stray laser light provides a local oscillator signal which is mixed with the plasma scattered signal to produce electronically detectable beat frequencies. Recently, this technique has been demonstrated in a low density discharge¹. Heterodyne detection required the use of fast IR detectors of the HgCdTe type. State of the art devices have > 700 MHz bandwidth with up to 100 volts/watt responsivity linear to ~ mW incident power levels.

REFERENCES

CHAPTER II

1. J.D. Jackson, "Classical Electrodynamics" (Wiley, New York, 1962).
2. E.E. Salpéter, Phys. Rev. 120, 5, 1528 (1960).
3. J.A. Fejer, Can. J. Phys. 38, 1114 (1960).
4. J.P. Dougherty and D.T. Farley, Proc. Roy. Soc. A 259, 79 (1960).
5. J.A. Fejer, Can. J. Phys. 39, 716 (1961).
6. D.T. Farley, J.P. Dougherty and D.W. Barron, Proc. Roy. Soc. A 263, 238 (1961).
7. M.S. Grewal, Phys. Rev. 134, 1A, 86 (1964).
8. A.A. Offenberger and R.D. Kerr, Phys. Lett. A 37, 5, 435 (1971).
9. C.C. Daughney, Confinement in Ohmic Heated Tokamaks (paper presented at 1975 CAP conf.).
10. E.T. Gerry, Ph.D. Thesis (M.I.T., 1965).

CHAPTER III

1. D.L. Jassby, J. Appl. Phys. 43, 11, 4542 (1972).
2. R.N. Morris, M.Sc. Thesis (Univ. of British Columbia, 1968).
3. A.J. Beaulieu, Proc. IEEE 59, 667 (1971).
4. N.H. Burnett and A.A. Offenberger, J. Appl. Phys. 44, 8, 3617 (1973).
5. J.R. Izatt and C.J. Budhiraja, Single Mode Operation of a Helical TEA CO₂ Laser by Injection of a CW CO₂ Laser Beam (paper presented at 1975 CAP conf.).

6. A. Nurmikko, T.A. DeTemple and S.E. Schwarz, Appl. Phys. Lett. 18, 130 (1971).
7. H. Nishihara and B. Kronast, Opt. Comm. 5, 1, 65 (1972).

CHAPTER IV

1. S. Glasstone and R.H. Lovberg, "Controlled Thermonuclear Reactions" (Van Nostrand, Princeton, 1960).
2. F.F. Chen, "Plasma Diagnostic Techniques", edited by R.H. Huddlestone and S.L. Leonard (Academic Press, New York, 1965).
3. L. Minnhagen, Arkiv för Fysik 25, 203 (1963).
4. C.J. Baker, T.L. deBruin and P. Zeeman, Z. Phys. 51, 114 (1928).
5. H.R. Griem, "Plasma Spectroscopy" (McGraw-Hill, New York, 1964).
6. D.W. Posener, Austral. J. Phys. 12, 184 (1959)
7. See reference III-1.

8. H.N. Olsen, J. Quant. Spect. and Rad. Trans., 3, 59 (1963).
9. H.F. Berg and W. Ervens, Z. Phys. 206, 184 (1967).
10. H.D. Campbell and A.J. Barnard, J. Quant. Spect. and Rad. Trans. 9, 3 (1969).
11. L. Spitzer, "Physics of Fully Ionized Gases" (Interscience, New York, 1962).
12. S.C. Brown, "Basic Data of Plasma Physics" (M.I.T. Press, Cambridge, 1966).
13. A.A. Offenberger and R.D. Kerr, J. Appl. Phys. 43, 2, 354 (1972).

CHAPTER V

I.P. Shkarofsky, T.W. Johnston and M.P. Bachynski, "The Particle Kinetics of Plasmas" (Addison-Wesley, 1966)

CHAPTER VI

1. J. Sheffield, "Plasma Scattering of Electromagnetic Radiation" (Academic Press, London, 1975)
2. See reference IV-5.
3. A.A. Offenberger, Ph.D. Thesis (M.I.T., 1968).
4. J.P. Dybwad and L.M. Logan, IR Phys. 13, 73 (1973).
5. See reference II-1.

CHAPTER VII

1. D.R. Baker, N.R. Heckenberg and J. Meyer, Phys. Lett. A 51, 3, 185 (1975).
-